7-16-2021 3:00 PM

Development of a Wireless Telemetry Load and Displacement Sensor for Orthopaedic Applications

William Anderson, *The University of Western Ontario*

Supervisor: Holdsworth, David W., *The University of Western Ontario*

A thesis submitted in partial fulfillment of the requirements for the Master of Engineering Science degree in Biomedical Engineering

Recommended Citation

Anderson, William, "Development of a Wireless Telemetry Load and Displacement Sensor for Orthopaedic Applications" (2021). *Electronic Thesis and Dissertation Repository*. 7971.
https://ir.lib.uwo.ca/etd/7971

Abstract

Due to sensor size and supporting circuitry, in vivo load and deformation measurements are currently restricted to applications within larger orthopaedic implants. The objective of this thesis is to repurpose a commercially available low-power, miniature, wireless, telemetric, tire-pressure sensor (FXTH87) to measure load and deformation for future use in biomechanical applications. The capacitive transducer membrane of the FXTH87 was modified, and a relationship was reported between applied compressive deformation and sensor signal value. The sensor package was embedded within a deformable enclosure to illustrate potential applications of the sensor for monitoring load. Finite element analysis was an effective tool to predict the fatigue life and failure location of 3D-printed Ti-6Al-4V and PLA load cells. Finite element models of fracture fixation loading scenarios were developed to evaluate the feasibility of internal sensing components. The proposed device presents a sensitive and precise means to monitor high-capacity loads within small-scale, deformable enclosures.

Keywords

Accelerometer, additive manufacturing, capacitive transducer, deformation, elastomer, fatigue, finite element analysis, load, orthopaedic implants, pressure, sensor, strain, telemetry, wireless, 3D printing

Summary for Lay Audience

Each year, there are hundreds of thousands of lower limb long bone fractures. The bone fractures are predominantly caused during trauma, such as motor vehicle accidents, or falls in the aging population. With most fractures, the affected area is stabilized using either internal or external fracture fixation devices. Internal fixation components include fracture fixation plates and intramedullary nails. These implants ensure that the broken bone segments are properly aligned and stable, so that the natural bone healing process is fast and successful. Unfortunately, in some cases, union between the broken bone segments does not occur or takes longer than normal. Prolonged bone nonunion can lead to fatigue failure of the fixation implant, which further damages the tissue surrounding the fracture location. Monitoring of the bone healing process is very subjective and highly dependent on the experience of clinicians to evaluate the affected region. There is a clear need for a sensorized implant that is capable of providing an objective measure of bone healing. The challenge is most currently available sensor packages are too big or do not have the necessary functionalities to be embedded within an orthopaedic implant. In this thesis, a miniature wireless sensor was developed using a commercially available tire pressure sensor. This novel sensor package is capable of monitoring load, small-scale displacement, acceleration, and temperature all within a miniature package. To demonstrate that this sensor was capable of being embedded within an orthopaedic implant, the sensor was instrumented within a custom 3D-printed deformable structure. The combination of the novel sensor and deformable enclosure generated a functional load cell that is capable of measuring physiological loads. To evaluate the performance of the load cells, the structures were subjected to theoretical and experimental mechanical testing. To determine if the novel miniature sensor package could be feasible for instrumentation within a fracture fixation implant, finite element models of long bone fracture fixation using a custom orthopaedic implant were generated. The miniature wireless sensor package described in this thesis is well suited to monitor load and displacement in many biomedical, commercial, and industrial small-scale and remote measurement applications.

Co-Authorship Statement

Chapter 1: Introduction

Sole Author – William Anderson

Chapter 2: Development of a Wireless Telemetry Sensor Device to Measure Load and Deformation in Orthopaedic Applications

Study Design – William Anderson, Sydney Wilson, David Holdsworth

Device Modification – William Anderson, Sydney Wilson

Data Collection – William Anderson, Sydney Wilson

Data Analysis – William Anderson, Sydney Wilson

Manuscript Preparation – William Anderson, Sydney Wilson

Manuscript Revisions – William Anderson, Sydney Wilson, David Holdsworth

Chapter 3: Design and 3D Printing of Wireless Load Cells for Biomedical Applications

Study Design – William Anderson, Todor Ivanov, David Holdsworth

Device Manufacturing – William Anderson, Tom Chmiel

Data Collection – William Anderson, Todor Ivanov

Data Analysis – William Anderson, Todor Ivanov

Manuscript Preparation – William Anderson

Manuscript Revisions – William Anderson, Todor Ivanov, David Holdsworth

Chapter 4: A Preliminary Investigation of Monitoring Bone Healing in Fracture Fixation Applications using the FXTH87

Study Design – William Anderson, Todor Ivanov, David Holdsworth

Data Collection – William Anderson, Todor Ivanov

Data Analysis – William Anderson, Todor Ivanov

Manuscript Preparation – William Anderson

Manuscript Revisions – William Anderson, Todor Ivanov, David Holdsworth

Chapter 5: Conclusions and Future Directions

Sole Author – William Anderson

Acknowledgments

During my time at Western, I had the opportunity to work with a remarkable group of talented individuals that have all contributed to help me get to where I am today. First and foremost, I would like to thank my supervisor and advisory committee, who have dedicated countless hours contributing to my development as a scientist and engineer. My supervisor, Dr. David Holdsworth, has been an endless source of knowledge and support. His dedication to his students' work is unmatched and he was always there to help me overcome any problems I faced. He instilled upon me the importance of the scientific process, which significantly improved my research from conception to communication. I am incredibly grateful to have worked with Dr. Holdsworth and the lessons he has taught me will pay dividends in both my personal and professional life. As a final aside, David's unique talent of being able to convey scientific problems and processes using analogies and his real-life experiences really made learning so much more fun and engaging. From the moon landing to the Super Ball, you never knew what story you would be told next. My advisory committee members, Dr. Ryan Willing and Dr. Emil Schemitsch, each came from different disciplines, but their wealth of knowledge in their respective fields greatly influenced the quality of my work and the direction of my project. I can't thank both of them enough for their contributions to my research and for their mentorship throughout my candidacy.

Throughout my time at the Robarts Research Institute, the technical staff in the Holdsworth lab group have always supported my research and have been an excellent source for both academic and personal guidance. Chris Norley, Hristo Nikolov, Steven Pollmann, and Jaques Milner have each been instrumental during the development and execution of the experiments described in this thesis. From acquiring the tools to create experiments, to helping me solve problems, the technical staff were always able to point me in the right direction. I would like to give a special thanks to Todor Ivanov for all of his help building and running many of the finite element models discussed in this thesis. Todor has taught me so much about the world of finite element analysis and his strong attention to detail has greatly improved the quality of my research. I am so lucky to have worked with such a special group and I am forever grateful for the contributions they have made to my project.

The group of graduate students I had the opportunity to work alongside have always been a source of support from the day I arrived at Western. Sydney Wilson, Santiago Cobos, Rudy Baronnette, Dr. Adam Paish, Dr. Daniel Lorusso, and Alexandra Blokker have all dedicated time to help me design experiments, troubleshoot problems, and review presentations. I could not have asked for a better group of friends and I will cherish the time we spent working together. I have to give an extra special thanks to Sydney Wilson for all of her help. It is impossible to put into words everything Sydney has done for me during my time at Western. This is a phrase that gets thrown around a lot, but it has never been more true in this case that I would not be delivering this work if it wasn't for the seemingly endless time Sydney has spent helping me with this project. Sydney's preliminary testing of the sensor described in this thesis immediately gave me a head start on my project. Her time developing and fabricating custom circuit boards, coding the sensor, helping design test apparatuses, and assisting with experiment data collection/analysis did not go unnoticed. It was a pleasure working with such a talented individual and I am excited to see all of the things she accomplishes in her career.

I would like to acknowledge the Bone and Joint Institute at Western for their financial support and for their resources, which have aided in my career development as a scientist and engineer. I was lucky to be a part of the collaborative specialization in musculoskeletal health research program, where I was able to take part in many development seminars and workshops. I was provided with the opportunity to interact and collaborate with faculty and students from a handful of different disciplines.

Finally, I would like to thank my family and friends for all of their everlasting support. My parents, Dave and Diane, have always been my biggest fans and I am incredibly lucky to have their support in all aspects of my life. My siblings and fellow Western graduates, Marnie and James, helped me get settled in London and made moving to a new university a whole lot easier. I would like to thank my grandfather, Doug "Buppa" Drysdale, for motivating me to pursue graduate studies and for his unconditional support in all of my endeavors. Lastly, I would like to thank Brynna Kerr for her scientific insight and support each and every day. My time in graduate school at Western has been an invaluable learning experience and I am excited to apply the skills I have learned in my future work.

Table of Contents

List of Tables

List of Figures

List of Appendices

List of Abbreviations

2D	Two-dimensional
3D	Three-dimensional
ABS	Acrylonitrile butadiene styrene
ADC	Analog to digital converter
CAD	Computer-aided design
CPU	Central processing unit
CT	Computed tomography
FEA	Finite element analysis
FDM	Fused deposition modeling
GUI	Graphical user interface
HDPE	High-density polyethylene
HIP	Hot isostatic pressing
MEMS	Microelectromechanical system
MRI	Magnetic resonance imaging
MVA	Motor vehicle accidents
NIST	National Institute of Standards and Technology
OIML	International Organization of Legal Metrology
PC	Polycarbonate
PDMS	Polydimethylsiloxane

PLA	Polylactic acid
PBF	Power bed fusion
PCB	Printed circuit board
QFN	Quad flat no-lead
SLM	Selective laser melting
STL	Stereolithographic
TPMS	Tire pressure monitoring system

Chapter 1

1 Introduction

This chapter will provide a detailed description of the pertinent background information of the work that was conducted in the subsequent chapters. An understanding of long bone injuries, surgical fixation strategies, a miniature wireless sensor device, 3D printing, load cell mechanisms, the current state of knowledge of each field, and areas for improvement must be obtained to follow the work in the coming chapters.

1.1 Long Bone Injury, Repair, and Treatment

Long bones, and more specifically femurs, are one of the most commonly fractured human bones and lead to rehabilitation periods that last months and even years. It is important to understand the prevalence of long bone fractures in our society today and the mechanisms that lead to fractures and subsequent complications. In addition, knowledge of natural bone repair and clinical treatment strategies are essential to help understand the short- and long-term prognosis of bone fractures.

1.1.1 Long Bone Injury

Long bone fractures are among the most frequently fractured bones for a number of reasons including but not limited to aging, osteoporosis, and trauma [1-3]. Depending on the severity of the fracture, the rehabilitation process can last months to well over a year. In addition to the bone fracture, there is almost always damage to surrounding soft tissue structures such as muscles, tendons, ligaments, blood vessels, nerves, and skin. Damage to these surrounding structures can increase recovery time and may lead to additional complications. The following section describes common mechanisms that result in long bone fracture and their prevalence in society today.

As people age, their risk of bone fracture significantly increases due to the decrease in the mechanical properties of bone [4]. These mechanical properties include elastic modulus, strength, and fracture toughness. The elastic properties of bone decrease with age, which results in a decrease of the stress required to form a crack [4]. As our current human population is aging, it is expected that the number of age-related fractures would significantly increase [5]. The mechanism of injury in many of these fractures is a fall. In the United States, it is projected that there will be over 3 million age-related fractures by 2025 [1]. While this number encompasses fractures from all regions of the body, it is expected that a sizeable portion of these fractures would occur in long bones, and more specifically the femur. In addition to the natural aging process, other bone diseases can also increase the susceptibility of a bone to fracture. One of the most prevalent bone diseases in society today is osteoporosis. Osteoporosis causes a reduction of bone mass, strength, and microarchitecture of the affected bones [5]. Degradation of the mechanical properties of bone greatly increases the likelihood of a fragility fracture. In the United States, it is estimated that by 2020 there will more than 14 million people with osteoporosis [6]. In addition, the number of people in the United States over the age of 50 years old is expected to increase 60% between 2000 and 2025 [6]. This will result in an increase in fractures related to the natural degradation of bone, as well as an increase in the number of people that have osteoporosis. For the femur specifically, in the United States in 2005, it was estimated that there were approximately 300,000 hip fractures [6]. Worldwide, the number of hip fractures was estimated to be approximately 1.66 million in 1990 but could rise to 6.26 million by 2050 [7]. The cost of a hip fracture can range between US $50,000 and US $70,000 depending on the time of operative intervention [8]. In the United States alone, this can amount to tens of billions of dollars. While osteoporosis is the most prevalent bone disease that significantly increases the number of bone fractures, it is important to note that there are many other bone diseases that can affect every age group of the population. Osteonecrosis, Paget’s disease, and osteogenesis imperfecta are just a few examples of bone diseases that alter the mechanical properties of bone [9]. It is clear that due to the increasing worldwide elder population, the natural course of bone aging, and bone diseases such as osteoporosis there will be a significant increase to the number of femoral and other long bone fractures worldwide.

Another leading cause of bone fractures is motor vehicle accidents (MVA). The energy generated in high-speed collisions can result in damage to bones and surrounding soft tissue structures. There have been few large-scale research studies focusing on femoral fractures in MVA; however, many smaller studies have been conducted that provide valuable insight into what population wide numbers may look like. In Sweden from 1998 to 2004, there we approximately 6400 inpatients with femoral shaft fractures [10]. A majority of the fractures were a result of falls in the elder population due to reasons previous discussed; however, approximately 17% or 1100 of the fractures were caused by MVA [10]. Of those 17% nearly 80% of the patients were male. A study in Brazil evaluating 200 cases of femoral fractures from 1990 to 2005 showed that 13.5% of the fractures were caused by MVA [11]. In many of the cases, when a person breaks their femur as a result of a MVA there is almost always additional damage to surrounding bones and soft tissue. One study has shown that 73% of patients that break their femur in a MVA also sustain at least one additional skeletal injury [12]. Non-skeletal injuries in the head, thorax, and pelvic regions were seen in 62% of the cases. These additional injuries can negatively influence the rehabilitation time of the broken femur, which can lead to revision surgeries and higher expenses associated with the injury. As for the location of the fracture along the femur, a study of approximately 500 femoral fractures following a MVA presented that the femur was fractured in the diaphysis region more predominantly that the proximal and distal regions [13]. While studies obtaining large population data of femoral fractures due to MVA have not been conducted, published numbers on the number of MVA are available. From the United States census of 2011 there were approximately 10.2 million MVA with nearly 40,000 deaths in 2008 [14]. It is reasonable to expect that there may be thousands of people that are admitted to local health care facilities with broken femurs as a result of a MVA. It is evident that a significant portion of femoral fractures in society today are caused by motor vehicle accidents and it is important to have effective treatment strategies in place that can minimize the rehabilitation process. From the numbers presented here, it is clear that there are hundreds of thousands of long bone fractures every year. This information is important to know when discussing bone healing complication rates in Section 1.1.4 and it illustrates how many people could benefit from improved treatment strategies.

1.1.2 Long Bone Repair

In the immediate aftermath of a long bone injury, the bone naturally begins to repair itself. This is a multi-stage process that can take many months to fully complete. This section will briefly describe the natural healing process from the time immediately following a fracture until bone union is achieved. Following a fracture, depending on the fixation strategy deployed to stabilize the region, either primary (direct) or secondary (indirect) bone healing will commence.

Primary bone healing, also known as direct bone healing, occurs when there is anatomical reduction of the bone fragments and they are in direct contact with each other [15]. At the fracture site, there is compression between the bone fragments with no movement between the fragments [15]. Therefore, this leads to absolute stability of the fracture region. In opposition to secondary bone healing (described below), there is no callus formation and bone remodels through basic multicellular units [15]. Internal compression plates are an example of a fixation method that initiates primary bone healing, as these plates promote absolute stability around the fracture site.

Secondary bone healing, also known as indirect bone healing, occurs when there is a small amount of movement at the fracture site and the bone heals through callus formation [15, 16]. As soon as a bone has been fractured the acute inflammatory response commences. A hematoma forms at the fracture site, which consists of peripheral and intramedullary blood, and bone marrow cells [15]. The injury triggers an inflammatory process that causes the hematoma to coagulate around the fracture. The hematoma generates the framework for the impending callus formation [15]. The acute inflammatory response is most active in the first 24 hours following a fracture and is typically completed after 7 days. During the inflammatory response TNF-Alpha, transforming growth factor-beta (TGF-β), bone morphogenetic proteins (BMP), and many inflammatory cytokines including IL-1β, and IL-6 are secreted [16]. The hematoma is slowly replaced by fibrous tissue [15]. During the repair phase, endochondral bone forms in the callus creating a cartilaginous matrix (soft callus). The cartilaginous matrix is converts to woven bone (hard callus) after the invasion of blood vessels and osteoblasts [15]. Finally, in the remodeling phase, the woven bone is remodeled into hard lamellar bone by basic multicellular units. The configuration of secondary bone healing is largely determined based the stresses applied to the fracture site [17, 18]. Locking plates are an example of an internal fixation method that promotes secondary bone healing. The most important take away from this section is that small bone-fragment movement and implant motion are critical components to initiating secondary bone healing. Implant motion and flexure could potentially be monitored using a sensorized implant to observe the bone healing process. With complete stability occurring around the fracture site during primary healing, it would be nearly impossible for a sensor to monitor the load acting through the implant and fracture site. Therefore, a future sensorized fixation implant must be designed to promote secondary bone healing. To determine which internal fixation implant is capable of stabilizing the region while promoting secondary bone healing, an understand of current internal fixation methods must be obtained.

1.1.3 Long Bone Treatment Strategies

Following a long bone fracture, a treatment strategy should be initiated as soon as possible. In many cases, fast alignment of broken bone segments and stabilization can improve outcome measures and reduce costs [19]. This section introduces the various stabilization methods that are deployed to treat long bone fractures today. For this thesis, only background on internal stabilization methods such as fracture fixation plates and intramedullary nails is provided. It is important to note that there are many other types of fracture stabilization. This includes external stabilization methods such as casts and external fixators.

Internal fixation methods involve a stabilization device being implanted within the injured limb of a patient. The most common internal stabilization devices are fracture fixation plates and intramedullary nails. Screws, pins, and wires usually accompany plates and nails to help provide additional stabilization. The objective of internal fixation devices is to restore natural bone anatomy while enabling fast mobilization of the patient [20]. Intramedullary nails are long rods, commonly fabricated in stainless steel and titanium alloy, which are inserted in the medullary canal of long bones. The intramedullary nail internally spans the site of the fracture and is locked at the proximal and distal ends using interlocking screws. Interlocking screws can be removed to create dynamization at the fracture site. The proximal and distal screws also help prevent torsion of the nail [20]. Intramedullary nailing is performed in antegrade (nail inserted proximal to distal) or retrograde (nail inserted distal to proximal) fashion, based on the bone fracture. Both techniques are commonly used in femoral and humeral shaft fractures, but for tibial shaft fractures, the antegrade technique is preferred [20]. Nails are inserted in the medullary canal with the assistance of a guide wire, a wire that helps align the broken segments of the bone. Nails are often cannulated so they can be inserted with the guide wire. The medullary canal is often reamed to enlarge the canal to a size similar to the diameter of the nail. While reaming does remove native tissue, it has been shown to be an effective technique to decrease bone non-union rates [21-24]. Intramedullary nails come in many different shapes and sizes depending on the bone they will be implanted in and the physical characteristics of the patient. For example, a femoral nail is bowed anteriorly to match the shape of the bone. Flexible intramedullary rods have been developed for youth whose bones have not fully matured in size. These flexible rods do not affect the function of the growth plate, ensuring that normal bone growth can continue. Flexible rods are inserted through the metaphysis of the bone and are targeted to stabilize diaphyseal fractures. One disadvantage of flexible nails is that they can also require external fixation methods, such as a cast, to help stabilize the region. Intramedullary nails have been an effective method of fracture stabilization as they result in low bone nonunion rates, low complications rates, fast return to mobility, and have a relatively small incision when compared to other internal fixation devices [25]. For diaphyseal bone fractures, the most common fixation device is an intramedullary nail [25-27]. However, with most fixation methods and orthopaedic implants as a whole, intramedullary nails have a number of disadvantages. In comminuted fractures that are treated with an intramedullary nail, leg length discrepancies have been observed in up to 43% of cases [28, 29]. If discovered, the patient may have to return to the operating room to relock the nail at the proper length. Like many orthopaedic implants, infection can pose a problem to the healing process if it cannot be quickly eradicated. In a review of multiple studies, infection rates in femoral shaft fractures treated with an intramedullary nail were reported to be approximately 1% [27]. Chronic infections can lead to nail removal until the infection has been resolved. This scenario increases the rehabilitation time of the patient, as revision surgeries must be performed. Fracture of the intramedullary nail itself is rare, occurring in less than 5% of cases [30]. In these scenarios there is typically prolonged non-union that causes the implant to fail due to fatigue. Nevertheless, intramedullary nailing is a very effective method of stabilizing long bone fractures and will continue to be used for many years to come.

In addition to intramedullary nails, fracture fixation plates are one of the main methods of internal stabilization of broken long bones and are the focus of the research conducted in subsequent chapters of this thesis. Fracture fixation plates provide rigid fracture fixation and are typically fabricated in titanium alloy or stainless steel. Plates typically span the fracture site and are fixed in place using screws on both sides and sometimes with lag screws through the fracture site. This diminishes the movement of the bone fragments when a functional load is applied [20]. The working principle of fracture fixation plates as a load-sharing device is that immediately following a fracture the plate bears the load acting on the fracture site. As the bone begins to heal the bone begins to take back some of the load. Eventually, when the bone is fully healed, the fracture fixation plate will not be loaded [31]. There are many different fracture fixation plates that are designed to tackle fractures in various bones throughout the body. There are two main types of fixation plates: compression plates and locking plates. These different plates are designed to provide varying levels of stability that determine the initiation of primary or secondary bone healing. The amount of strain present at the fracture site determines the mechanism of healing [31]. The strain over the fracture site is calculated by dividing the change in fracture gap by the initial gap length. For primary bone healing to occur, the gap fracture strain must be less than 2%. Secondary bone healing will occur if the fracture gap strain is between 2% and 10%. If the strain exceeds 10%, bone healing will not be successful. The objective of compression plates is to provide absolute stability, a rigid fixation. This nearly eliminates fracture gap strain and promotes primary bone healing. Compression plates reduce strain by minimizing the initial gap length and halting any fracture site displacement. Compression plates are capable of resisting axial, torsion, and bending forces, when placed on the side of the fracture where tension is present [32]. Conventional compression plates convert the axial load applied to the plate to shear stresses at the interface of the fixation plate and the bone [31]. The frictional forces at this interface counteract the applied axial force. The maximum axial forces that a compression plate can withstand depend on the product of the coefficient of friction at the plate-bone interface and the force normal to the plate, which is determined by screw torque applied during plate insertion [31]. In clinical practice today 3-5 Nm of torque is recommended for 3.5 mm cortical screws, which results in a maximum plate axial load capacity of approximately 1200 N [32-34]. Screw length and torque is selected on a case-by-case basis by the surgeon leading the operation. If screw torque does not reach the recommended threshold, absolute stability is not maintained, which results in fracture motion and a halt in fracture healing. Increased screw torque can result in stripping of the screw leading to reduced fixation and subsequently no bone healing. In compression plates the screw-bone shear interface is the weakest link in the plate-screw-bone mechanism [31]. Under bending the highest shear stresses occur at the outer most screws on the plate. Techniques such as increasing contact area between screw and bone, using locking plates, and increasing friction at the plate-bone interface can reduce shear stresses at the screw-bone interface [31]. One downside of compression plates is that they generate large compressive forces at the plate-bone interface that can lead to limited blood supply reaching the periosteum of the bones. Reduced blood flow can result in bone necrosis, bone resorption, and loosening of the fixation plate [31]. In response to this problem, limited contact compression plates were developed to minimize surface contact [35-37]. These compression plates still rely on the plate-bone interface for fixation.

As an alternative to compression plates, the use of locking fixation plates promotes initiation of secondary bone healing, the preferred mechanism of healing in diametaphyseal regions [31]. Locking plates promote secondary bone healing as the implants bridge the fracture site, therefore allowing small strain to occur while stability is provided. Locking plates function as a single-beam construct where there is no motion between the plate, screws, and bone. In opposition to compression plates, locking plates and screws are both threaded. As the male thread component on the head of the locking screw interacts with the female thread component on the locking plate, a mechanical lock is formed, and the position and rotation of the screws with respect to the plate is fixed. The screw holes in locking fixation plates allows for the placement of screws at varying angles because they feature both a conventional hole and threaded hole. Locking plates provide better fixation than conventional compression plates because they convert shear stresses into compressive stress at the screw-bone interface [31]. Healthy human bone is more resistant to compressive forces than shear stresses. As a single-beam construct that converts shear stress into compression, the fixation of locking plates does not depend on friction at the plate-bone interface. Therefore, preserving the blood supply beneath the fixation plate. Due to the unique screw holes in a locking plate, the plate can function as a compression plate (if only conventional holes are used), a locking plate (only threaded holes are used), or a hybrid plate (use of both conventional and threaded holes) [38]. Hybrid plates are utilized in unique cases at the discretion of the surgeon.

From the descriptions of the common types of internal stabilization methods, locking fracture fixation plates are the implant most likely to be capable of successfully monitoring the bone healing process. Locking fixation plates promote secondary bone healing, which allows small implant flexure to occur at the fracture site. Our hypothesis is that this small implant flexure may be monitored by a miniature sensor device. This reduces the feasibility of using sensorized compression plates to monitor fracture gap strain and bone healing, as they promote primary bone healing. Absolute stability with very limited motion (less than 2% fracture gap strain) around the fracture site would be challenging to measure using a sensorized compression plate. The inherent size and thickness of locking fracture fixation plates make it feasible for a sensor device to embedded within the implant. As intramedullary nails are inserted through the medullary canal of the bone, they have a very small diameter, and it would be challenging to embed a device inside such a small space.

In clinical practice today, there are a variety of different mechanisms deployed to combat long bone fractures. These internal and external stabilization methods come in many different shapes and sizes, but all share a common goal, to safely and effectively return the patient to normal function. Each fixation method has many designs for different types of bones around the body. However, to develop a sensorized implant that is capable of monitoring the long-bone healing process, a locking fixation plate is the best alternative. While these fixation methods are all generally very effective, the rehabilitation time and complication rates associated with each method may vary.

1.1.4 Long Bone Treatment Prognosis

After a patient has broken a long bone and has received a fixation device, the prognosis of the injury is dependent on the selected stabilization method. This section evaluates the prognosis of a long bone injury following fixation of bone segments for the treatment strategies described in Section 1.1.3. Success and complication rates are presented for each of the different stabilization methods. It is important to understand the prognosis of the injury so that an effective treatment strategy can be quickly selected. In addition, understanding complication rates can help improve future implant design and lead to an increase in successful patient outcomes.

Following bone stabilization there are three outcomes that can occur: union, nonunion, and malunion. Union is defined as successful bridging of the broken bone segments and the normal anatomy of the bone is restored. This is the most optimal outcome as the patient is likely able to return to normal activity. Nonunion occurs when the bone has not healed. If the fracture has not healed additional surgeries may be required in order to initiate a successful healing process. Long term nonunion can result in prolonged loading of the fixation device and could lead to implant failure. There are many different factors that can result in bone nonunion. For example, excess fracture site motion and infection are two common factors that lead to bone nonunion. In addition, use of tobacco and delaying a return to weight bearing have also been shown to be risk factors for femoral nonunion [39]. Finally, malunion occurs when the bone has healed but not in proper alignment. The bone may not be of adequate length, can have a rotational deformity, or an angular deformity. In femurs, malunion is diagnosed when there is shortening by more than 2 cm or an angular/rotational deformity greater than 10 degrees [40]. The work presented in this thesis focuses on monitoring bone union, therefore attempting to eliminate bone nonunion. While malunion is an important outcome of many orthopaedic surgeries, nonunion rates are more relevant to the work presented in this thesis and will be the focus of this section.

For the most part, both internal and external stabilization techniques are very effective in the femur. However, there is still a significant percentage of patients that are affected by bone nonunion [41]. It is important to note that the numbers presented in this section are from different research studies that had varying sample sizes with patient populations that may never have had the exact same fracture location and geometry. Nevertheless, these studies provide a good indication of the femoral nonunion rates when treated with internal and external stabilization methods. In a review of four studies, treatment of femoral fractures with fracture fixation plates had nonunion rates ranging from 2% to 7% [41]. In addition, a review of eighteen studies that used a locking plate for stabilization of distal femoral fractures has presented that nonunion rates generally range between 0% and 21% but can also be as high as 32% [42, 43]. In a review of three studies, femoral treatment using external fixation had nonunion rates ranging from 0% to 12% [41]. In seven studies, patients treated with intramedullary nails had nonunion rates ranging from 0% to 8% [41]. Insertion of intramedullary nails was performed via a variety of techniques, including reamed antegrade nailing, unreaming antegrade nailing, and retrograde nailing. Based on the femoral nonunion percentages presented here, it is reasonable to expect that with the current number of femoral fractures occurring annually (Section 1.1.1) there could be tens of thousands of cases of femoral nonunion occurring each year. Eliminating bone nonunion can decrease the rehabilitation time of the patient and can reduce costs as revision surgeries will not have to be performed. One solution to solving bone nonunion is to develop an implant that is capable of monitoring the bone healing process. This would allow clinicians to determine when a bone has healed and when it is safe to return to weight bearing or when to remove the implant, if necessary. In clinical practice today, there are few truly objective methods of measuring bone healing. Effective tools such as the radiographic union score for tibias have been developed to assess fracture healing by subjective assessment of cortical bridging [44]. However, it still depends on the experience of a clinician to evaluate an X-ray to determine if a bone has healed. For years there has been not been a general consensus among orthopaedic surgeons on the assessment of fracture healing [45]. Development of a sensorized implant could reduce bone nonunion by providing an objective measure of the bone healing process.

1.2 Novel Miniature Wireless Sensor Device

To develop a sensorized implant capable of monitoring bone healing, a miniature wireless sensor device must be constructed that is small enough to fit within orthopaedic components while measuring and transmitting data. In recent years, advancements have been made miniaturizing automotive sensor packages, which have enabled their use in a variety of small-scale applications. The FXTH87 is a tire pressure-sensing package developed by NXP Semiconductors (Figure 1.1). It is the key component in many commercially available tire-pressure monitoring systems (TPMS). The FXTH87 tire pressure sensor is a microelectromechanical system (MEMS). MEMS is a process technology used to develop miniature, integrated devices or systems that combine both electrical and mechanical components [46]. Devices are capable of sensing, control, and actuation on the micro level.

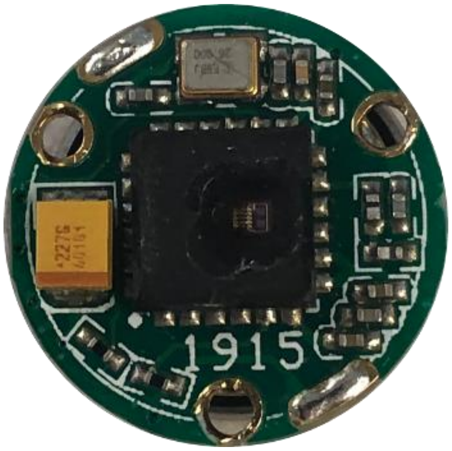

Figure 1.1: FXTH87 tire pressure sensor in commercial TPMS configuration.

Due to the unique environment of orthopaedic sensing applications, the ideal sensor would feature a low-power, stand-alone, miniature sensor package that is capable of measuring load and strain. The proposed sensor package, the FXTH870511DT1 (FXTH87), features an 8-bit 4 MHz CPU, 315/434 MHz RF transmitter, 6 channel 10-bit ADC, 125 kHz LF receiver, pressure sensor, dual-axis accelerometer, temperature sensor, and additional components, making the FXTH87 a fully functional wireless telemetry package [47]. All sensors, transmitting equipment, memory, and CPU for the FXTH87 are housed inside a miniature package measuring 7 mm × 7 mm × 2 mm, making it one of the smallest pressure sensing packages in the world. This package utilizes a capacitive pressure transducer to obtain pressure measurements. The mechanism capacitive transducers use to measure displacement and load is expanded upon in Section 1.4.3 below, but briefly, capacitive pressure transducers feature two metallic plates held in parallel and separated by a dielectric medium [48, 49]. The bottom plate, known as the electrode, is held fixed and used as a reference for the top plate. The top plate is called the diaphragm and it can move closer to the electrode. As the diaphragm moves toward the electrode and the distance between the two plates decreases, the output capacitance increases. In its commercial configuration, the capacitive pressure transducer is calibrated to measure changes in air pressure. For the sensor configuration described in this thesis, instead of measuring air pressure, the onboard capacitive transducer can be modified and then calibrated to measure load and deformation by manipulating the distance between the electrode and the diaphragm using a 3D-printed mechanical indenter. The capacitive transducer onboard the FXTH87 can also be manipulated by embedding the sensor in a deformable spring body. As a force is applied to a spring body, the structure deforms, and contacts the surface of the capacitive transducer of the FXTH87. As is presented in this thesis, the deformable spring body can take the shape of a simple deformable structure or in a more complex design, an orthopaedic component. To develop deformable structures and implants, additive manufacturing (3D printing) can be selected to quickly fabricate custom objects that accommodate the FXTH87 sensor device.

1.3 Additive Manufacturing

Within the last decade, additive manufacturing (commonly known as 3D printing) has increased in popularity and functionality and has been proven to be a suitable alternative to traditional manufacturing techniques. Additive manufacturing allows for rapid prototyping of complex structures in a variety of materials consisting of but not limited to plastics, metals, and metal alloys. Additive manufacturing has grown to a point where it may be capable of improving upon traditional fabrication methods in many different industries. For example, fabrication of orthopaedic implants using additive manufacturing could allow custom implants to be built that can accommodate internal placement of sensor packages. In addition, 3D printing can be used to generate patient-specific implants. Custom implants conforming to native anatomy may have the potential to improve implant success rates and decrease complications [50-52]. This section will discuss the plastic/metal additive manufacturing process and the feasibility of using additive manufacturing to develop custom orthopaedic implants and other deformable structures.

1.3.1 Additive Manufacturing Process

Additive manufacturing (or 3D printing) is a method of creating three-dimensional objects by depositing material, commonly in layers. This process is controlled by a computer that manipulates the movement of a nozzle, laser, or electron beam to deposit a filament or form solid structures [53]. The custom structure, developed in computer-aided design (CAD) software, is built one layer at a time until the full object has been erected. To prepare a structure for printing, the part is imported into slicing software that breaks the object into different layers and generates an optimal path for the nozzle, laser, or electron beam. While there are many different types of additive manufacturing processes, fused deposition modeling (FDM) and powder bed fusion (PBF) via selective laser melting (SLM) are the focus of this section, as they are the processes used to build structures discussed in subsequent chapters.

FDM is one of the most popular additive manufacturing methods because the thermoplastic materials used in this process are inexpensive when compared to metals. FDM can quickly generate complex structures in a safe and reliable manner [54]. In FDM a build material, also known as filament, is fed into a liquefying head from a spool. The liquefier head melts the filament, and a nozzle dispenses the material on a flat build plate along a path predetermined by slicing software [54]. When the liquefied filament leaves the nozzle it quickly cools into a solid and becomes the base for the next layer. The nozzle traces the cross-sectional geometry of the object layer by layer until the part is complete. Common materials used in FDM are polylactic acid (PLA), acrylonitrile butadiene styrene (ABS), high-density polyethylene (HDPE) and polycarbonate (PC) [54]. Objects fabricated using FDM have mechanical properties comparable to conventional fabrication methods such as thermoforming and injection moulding [55]. The static and dynamic mechanical properties are highly dependent on FDM process parameters. Process parameters such as raster gap (space between material deposits) and raster angle (angle of material deposits) have been shown to determine the mechanical properties of the object [56-58]. Settings within the slicer software allow the user to adjust a variety of printing parameters to ensure the finished product is fabricated as it was designed. FDM is a fast, effective, and inexpensive method of 3D printing plastics and is a useful method for rapid prototyping and modeling.

PBF is an additive manufacturing technique that uses thermal energy to fuse specific areas of a powder bed [59]. SLM and electron beam melting are the two techniques used in PBF. SLM is the process used in fabrication of components presented in subsequent chapters and will be the focus of this section. Additive manufacturing via PBF can fabricate objects made of stainless steel, cobalt chrome alloy, titanium alloy, and other metals. The PBF process consists of two inert gas or vacuum sealed chambers (the power chamber and the build chamber), a metallic powder, a roller, and energy source. Both the power and build chambers are filled with an inert gas or are a vacuum to protect the regions fused by the laser from exposure to atmospheric contaminants such as oxygen and water vapor. Using shielding gas to prevent exposure to these particles improves the quality of the metal fusion [60, 61]. The powder chamber and build chamber each have pistons that adjust the powder supply and build plate, respectively. At the start of the printing process, the roller or recoater arm pushes a thin layer of powder from the powder supply in the powder chamber across the surface of the build plate in the build chamber. If SLM is the selected fabrication technique, a laser is used to trace and selectively melt the powder occupying the space of the first cross sectional slice of the desired part. When a layer is completed, the piston in the build chamber moves the build plate downward and the piston in the powder chamber moves upward. The adjustment in height is determined by the user-defined layer thickness. Next, the process is repeated, powder is spread across the build plate and selectively melted by the laser. Once the part has been completed, excess powder is removed to extract the part. Depending on the size of the object being printed, multiple parts can be placed on the build plate. Common defects associated with SLM are porosity, lack of fusion (i.e. non-consolidation), and crack formation [62]. For complex objects, supports can be generated in the slicer software and can be removed in post-processing. Once the supports are removed, the part can undergo post-processing techniques such as heat treatment and polishing. Hot isostatic pressing (HIP) may also be applied to the object to decrease porosity and increase density [63]. Post-processing techniques can improve mechanical properties and decrease the surface roughness of the part [64]. An expanded discussion on the benefits of post-processing techniques and how they are important specifically to implant design is presented in the following section, Section 1.3.2. While PBF with SLM is significantly more expensive than plastic FDM, it is an effective method of fabricating high-quality metallic parts.

1.3.2 Considerations for 3D Metal Printing of Orthopaedic Implants and Deformable Structures

With metal additive manufacturing increasing in popularity and accessibility, it has opened the door to for use in the orthopaedic industry. 3D printing technology can fabricate anatomical models, surgical instruments, orthopaedic implants, and prostheses [65]. While the applications of metal additive manufacturing in the orthopaedic industry are seemingly endless, 3D printing of orthopaedic implants will be the focus of this section. With the imaging modalities and 3D printing facilities available today it is possible to design and fabricate patient-specific orthopaedic implants. This process involves obtaining three-dimensional (3D) images using computed tomography (CT) or magnetic resonance imaging (MRI), segmentation of the images to create a 3D model, and design of the implant based on native anatomy and other surgical factors [66]. The advantage of patient-specific implants is improved outcomes, as there would be fewer complications during surgical procedures. Even if a custom implant is not fabricated, surgeons can generate a physical model of the native anatomy to help plan for the surgical intervention. Additive manufacturing can create custom implants with complex geometry; designs which are unobtainable using subtractive manufacturing methods. For example, porous structures can be created that can improve osteointegration, reduce stress shielding at bone-implant junctions, and have an elastic modulus comparable to human bone [67-69]. 3D-printed implants that have custom geometry matching that of the patient can be biomechanically tested using patient-specific loading conditions in finite element analysis software. This advises the engineer and clinician whether the custom implant needs to be modified or is feasible for implantation. Patient-specific 3D-printed implants have been deployed to tackle hip arthroplasty, bone tumor resection, and spinal fusion. While any implant geometry can be created using 3D printing, it does not necessarily mean that the implant is feasible for use in a surgical intervention. One reason that was widely holding back the use of 3D-printed implants was inconsistent manufacturing quality. Facilities fabricating implants must be certified under ISO 13485 before being able to apply for authorization to implant 3D printed materials. ISO 13485 specifies requirements for a quality management system for manufacturing of medical devices [70]. In recent years, an increasing number of fabrication facilities have been certified under ISO 13485, which increases the number of groups that can begin work on manufacturing patient-specific implants. Components manufactured in ISO 13485 certified facilities are safely 3D printed, consistently of high quality, and have no cross contamination from other materials. In the post-processing phase every printed object is subjected to an assessment from a trained technician to ensure quality standards are met. Another reason limiting the wide use of 3D printed orthopaedic implants are concerns about the mechanical properties of 3D metal printed materials. As the methods of additive and subtractive manufacturing are different it is expected that there may be a discrepancy in mechanical properties. Components additively manufactured using titanium alloy (Ti-6Al-4V) were found to have similar ultimate tensile strength, yield strength, and elongation to wrought titanium alloy [71-73]. However, the fatigue properties of 3D printed titanium alloy fabricated using SLM are significantly lower than wrought material [74-77]. In addition, anisotropy in the fatigue performance was observed to be dependent on build orientation of the component. Reduced fatigue life is a cause for concern as orthopaedic implants fabricated using 3D printing could potentially fail sooner than traditional implants. Components fabricated using 3D metal printed have a reduced fatigue life due to factors including microstructure, porosity, and surface finish [74]. A rough external surface can lead to crack initiation and subsequently premature fatigue failure. Similarly, internal porosity produces stress concentrations that may result in crack initiation and propagation. In order for 3D-printed metals to be implemented in orthopaedic applications their fatigue life must be improved. Post-processing techniques such as HIP and shot peening are effective at improving fatigue life by reducing porosity and residual stresses [71, 78, 79]. Studies have also shown that decreasing surface roughness can increase the fatigue performance of 3D printed objects [80]. Methods of decreasing surface roughness include polishing, chemical etching, electrochemical polishing, shot peening, and laser-ablation [80]. Due to the nature of unprocessed 3D metal printed components, orthopaedic implants fabricated using additive manufacturing and SLM methods must undergo a significant amount of post-processing techniques to be mechanically feasible for use in patients. In regard to internal fracture fixation, few studies have been published discussing testing and feasibility of 3D printed implants. This is likely because existing conventionally manufactured implants provide sufficient surgical intervention in an overwhelming majority of cases. However, 3D metal printing may be an advantageous tool in the rapid fabrication of custom fracture fixation components with embedded sensor packages. In this case, a full mechanical evaluation of 3D metal printed fracture fixation implants would be required to determine whether a sensorized implant would be feasible for clinical use. These implants must undergo static and dynamic mechanical evaluation, similar to tests performed on existing implants fabricated using traditional manufacturing methods. To conclude, 3D metal printing is an effective tool to quickly create implants with patient-specific geometries. With sufficient post-processing, 3D metal printed implants can be safely tasked in a variety of dynamic in-vivo applications, however more data is required to determine if said implants are feasible for use in fracture fixation.

1.4 Mechanisms of Load Measurement

Load measurements are an integral part of many applications in a variety of industries. Due to the diversity of load cell applications, there is a need for load cells that are capable of measuring a wide range of load values. In addition, there are different requirements for how much a load cell can deform during the process of force measurement. As with many engineering problems there is almost always more than one way to solve a problem. In the case of load cells, there are a handful of different mechanisms capable of measuring load. This section will introduce the two components of a load cell, the sensor and spring body, and the conventional techniques used to measure load. Emphasis is placed on resistive and capacitive load transduction, as resistive sensors are the most commonly used load sensors today and capacitive sensors because this method is utilized in the device described in subsequent chapters. In this thesis, a novel miniature wireless load cell is described so it is important to understand the measurement mechanisms used in existing devices and how they differ from the proposed load cell.

1.4.1 Two Components of a Load Cell

For any load cell to be successful they require two components: a sensor and a spring body. For most load cells, the sensor is commonly a resistive, hydraulic, piezoelectric, or capacitive sensor. A spring body is an elastic structure that returns to its original shape or position following the application of a force. As a force is applied to the load cell, the spring body deforms. Simultaneously, the sensor of choice is measuring the deformation of the spring body. It is a common misconception that load cells directly measure load. In reality, every load cell only measures deformation, which is then converted into a load value. In many applications, the deformation of the spring body is so small that it is barely visible to the naked eye. For example, when you step on a bathroom scale or place your groceries on the self-checkout platform you don’t feel any movement of the spring body. The sensors used in these types of load cells are capable of detecting very small deformation values and converting them into a load value. In many load cells, the spring body is the key component that determines the load capacity of the load cell. The same sensor package can be used to measure a load of 10 N or 10 kN because the sensor is only measuring the deformation of the spring body. In this scenario, each spring body would be precisely designed to deform a specific distance under a specific load using finite element analysis or mechanical deflection equations. As the same sensor can be used to measure a wide range of load capacities, it is critical that each sensor be calibrated inside the deformable spring body it is paired with.

There are many different spring body designs that are optimized to measure a wide range of load values. The most common load cell devices commercially available today have beam, S-type, or button spring bodies [81]. Cantilever beam spring bodies are commonly fixed at one end and free at the other end. As force is applied to the free end of the beam, the structure deforms. The deformation is measured using resistive sensors such as strain gauges, which are bonded to the surface of the structure. S-type spring bodies are similar to beam spring bodies as S-type load cells feature beams on the top and bottom of the load cell that deform during loading. S-type load cells can be used to measure both compression and tension forces and are commonly paired with resistive sensors. Finally, button load cells are circular and have a focal point in the centre, to which a force is applied. When a force is applied, the spring body within the button deforms. Button load cells are best at measuring axially applied compression forces. Button load cells can feature resistive, pneumatic, hydraulic, or capacitive sensors. These different spring body designs are capable of measuring hundreds of grams to thousands of kilograms. In addition, these spring bodies are designed to reach their specific load capacity under a very small amount of deformation.

The capacity of a spring body does not only depend on the shape of the structure. It is heavily determined by the mechanical properties of the material used in spring body fabrication. For example, consider two geometrically identical spring bodies, with one made of metal and the other a plastic; in this case, the metal structure will require a higher force to deform, as it has a higher elastic modulus than plastic. In addition, it is preferable to use materials that are highly resistant to fatigue. Even though the strain of the spring body will keep the material within its elastic limit it is still susceptible to fatigue failure after a number of cycles. When designing the spring body for a load cell of a specific capacity it is important to tune the geometry of the structure while taking into consideration the properties of the material that will be used to fabricate the structure.

1.4.2 Resistive Load Sensors

The most popular sensors used in commercial load cells are resistive sensors called strain gauges. Strain gauges are composed of thin metal wire arranged in a snaking pattern on a flexible material [82]. Strain gauges are bonded to the deformable region of the spring body. As the strain gauge is deformed during loading, the resistance of the wire changes as the diameter, length, and resistivity of the wire is altered [83]. Strain gauges are oriented so that when a force is applied in a single direction, a linear change in resistance occurs. During compression, the diameter of the wire increases, and the length of the wire shrinks, which decreases resistance. Under tension the diameter of the wire decreases as the length is stretched, which results in increased resistance. The small change in resistance of the wire can be measured as a change in voltage. As the change of resistance in a single strain gauge is very small, multiple strain gauges are connected in a Wheatstone bridge to amplify the changes. A precise voltmeter is placed across the Wheatstone bridge to measure the change in output voltage. The system can then be calibrated because load values can be matching with a corresponding output voltage. While a strain gauge can only measure a change in load along one axis, multiple strain gauges can be installed at various angles to measure load in more than one direction. As was previously described, there is no limit to the amount of load that a strain gauge can measure as that depends on the properties of the accompanying spring body. However, there are limits to the amount of deformation a strain gauge can withstand, therefore it is vital to ensure that the strain gauge does not deform beyond the elastic limit of the wire material or the spring body. Strain gauges are deployed within beam type, S-type, and button type load cells and are used to measure compression, tension, flexure, and torque. As strain gauges output an analog voltage value, accompanying signal conditioning and processing units are required to provide the user with data in conventional load units.

1.4.3 Capacitive Load Sensors

Capacitive force transducers are one of the most widely used mechanisms of load measurement as capacitive sensors are precise and have high resolution [84, 85]. In addition, capacitive sensors are small in comparison to other load sensors, which makes them ideal for small-scale applications. The miniature device presented in this thesis utilizes a capacitive transducer to measure both deformation and load. The capacitive transducer described in this thesis incorporates two parallel metallic plates separated by an elastic dielectric medium. The top plate is called the diaphragm and, as its name implies, it is capable of motion [48, 49]. The bottom plate, named the electrode, is held fixed and is used as a reference for the diaphragm. As a force is applied to the diaphragm it moves closer to the fixed electrode. This results in an increase in capacitance, which can then be correlated to the displacement or force causing the shift of the diaphragm [83]. When the force is removed from the diaphragm, the elastic dielectric material helps the plate return to its original position. The position of the diaphragm can be manipulated in a variety of ways including using air pressure or a mechanical indenter. Similar to other mechanisms of load measurement, capacitive transducers can be embedded with deformable spring bodies of varying capacity to measure a wide range of load values.

While each mechanism of load measurement presents a unique method of obtaining load values, resistive and capacitive based load cells are the most popular devices used today. Load cells that utilize these mechanisms can be very small in size, highly accurate, inexpensive, and reliable over long periods of time. This makes them both feasible for use in small-scale applications such as orthopaedic sensing. Pneumatic and hydraulic load sensors are very useful in larger scale industrial applications but are incapable of being effective in miniature sensing applications. A case is made in this thesis that capacitive based load sensors are advantageous to resistive load cells in certain applications as capacitive sensor packages, such as the FXTH87, can measure comparable load magnitudes but in a wireless device that is smaller in size and contains additional integrated processing/telemetry components.

1.5 Performance Targets for Load Cells

1.5.1 Metrological Regulations for Commercial Load Cells

Load cells that are commercially available today must ensure that they satisfy load cell regulation requirements developed by the International Organization of Legal Metrology (OIML) and the National Institute of Standards and Technology (NIST). Document R60 Parts 1 and 2 [86] describe the metrological and technical requirements for load cells as well as metrological controls and performance tests. While this document describes requirements and performance standards for strain gauge-based load cells, the document states that it can be used to guide testing on load cells of different mechanisms. The testing procedures described in this standards document can be used to test the capacitive load cell developed in this thesis. Mechanical tests performed on the load cell include creep, minimum dead load output return, and repeatability. Document R60 suggests tests can also be performed to determine the effect changing temperature, pressure, and humidity have on the output load value.

To understand the methodology of the mechanical tests performed on the sensor, it important to define terms related to the measuring range of the load cell (Figure 1.2). The maximum measuring range of a load cell is determined by the values of minimum dead load (E_{min}) and maximum capacity (E_{max}). Minimum dead load is defined as the smallest quantity (units of mass) that can be applied to the load cell. The maximum capacity of the load cell is the maximum amount of load the can be applied to the load cell. The safe load limit (E_{lim}) is the maximum load that can be applied without causing permanent damage to the load cell. Document R60 suggests that the load cell measuring range is not simply the range between the minimum and maximum load that can be applied to the load cell. It is suggested that the minimum load of the measuring range (D_{min}) is greater than E_{min} but less than 10% of E_{max}. On the other end the maximum load of the measuring range (D_{max}) should be less than E_{max} but greater than 90% of E_{max}. Therefore, the load cell measuring range (D_R) is the difference between D_{max} and D_{min}. It is important that the measuring range of the load cell is established before mechanical testing, as the measuring limits of the device dictate the experimental testing procedure.

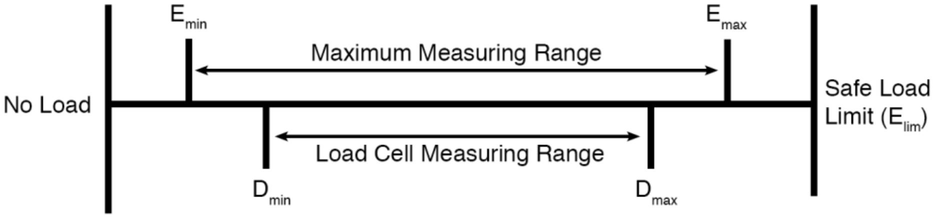

Figure 1.2: Measuring range of a load cell. Derived from [86].

1.5.2 Performance Standards for Implantable Load Sensors

As was described in Section 1.5.1, the regulations for commercial strain gauge load cells do not apply directly to the sensor and load cell proposed in this thesis. However, they can be a useful tool to help develop tests that can be performed on the sensor package. Throughout this thesis, primarily in Chapter 2 and 3, tests are performed on our proposed sensor to evaluate its performance. As the sensor package is intended to be tasked in orthopaedic applications, performance targets can be set to evaluate the success of our proposed sensor package. Currently, there are no officially published works describing performance regulations for implantable load sensors. It is important to note that performance standards are different from safety regulations, which is not the primary focus of the work presented in this thesis. For every implantable sensor package, it is important that they are electrically, chemically, physically, and biologically safe for the patient [87]. The work presented in this thesis is focused on quantifying variables such as sensor error, load capacity, power consumption, and transmission range. In the future, work describing the preparation of our proposed sensor for in-vivo environments would include tests to ensure the sensor package can be hermetically sealed and is not susceptible to electrical disturbances.

While published work describing performance standards for implantable load sensors has not been developed, we can generate realistic performance targets using the published work of groups that have previously developed implantable sensors. The key performance variables for implantable load sensors, both capacitive and resistive based, include sensor error, repeatability, creep, hysteresis, sensitivity, load resistance, load capacity, deformation capacity, power consumption, and transmission range. To ensure the most accurate measurements are recorded, it is important to ensure that the sensor error is low. A hip prosthesis developed by [88], is capable of monitoring loads of 2 kN to 5 kN and has reported measuring error ranging from 0.4% to 0.9%. An instrumented tibial implant developed in [89], could measure loads of 2 kN with average errors of 1%. For our proposed sensor, it would be advantageous to have comparable error values, but error values less than 5% would provide us with a good indication of the true load being measured. Next, it is important that the sensor can provide repeatable measurements over a long period of time, which allows the sensor to be calibrated. In previously described devices, repeatability error ranged from less than 1% to 8% [90-92]. While errors close to 0% are preferable, a repeatability error of less than 5% would indicate that consecutive sensor tests are repeatable. For the sensor to be a useful measurement instrument in both static and dynamic applications, it is advantageous for the sensor to undergo minimal creep and hysteresis. For load cells, a creep test involves subjecting the sensor to a constant load for 30 minutes [86]. Creep error is determined by monitoring the change in signal output during the test. Creep error is calculated by determined the change in signal output as a percent of the full-scale load range of the load cell. In an ideal scenario, the response of the sensor would stay the same for the duration of the test. However, due to the unique design of the proposed sensor, which is described in Chapter 2 and 3, a small creep error is expected. This error is a result of using a viscoelastic material to convert a pressure sensor into a functioning load sensor. From previously described material testing, the relaxation response of the elastomeric material Sylgard 184 corresponds to a creep error of approximately 5% [93]. Therefore, as some creep error is expected, it would be optimal if the creep error of the proposed sensor is comparable to previously published material testing research. In load cells, hysteresis error is defined as the maximum difference in load between loading and unloading cycles as a percent of the full-scale load range of the sensor package. An error value close to 0% would indicate that the sensor reports the same signal value at a specific load level during both loading and unloading cycles. Sensors with low hysteresis error are commonly tasked in dynamic applications as the packages provide consistent measurements during the loading and unloading cycles. Previously described resistive and piezoelectric sensing solutions for orthopaedic applications reported hysteresis errors of less than 1% and 10%, respectively [94, 95]. For the sensor proposed in this thesis, having comparable hysteresis error values would further validate that the sensor could be tasked in dynamic orthopaedic applications. Next, the sensitivity of the sensor must be high enough to be able to monitor very small changes in displacement and subsequently load. The displacement range of an orthopaedic implant will likely be very small (less than a millimeter) so the sensor must sensitive enough to monitor this deformation. A sensitivity of greater than 1 signal unit/μm would provide adequate characterization over the measuring range and would enable the sensor to measure very small changes in displacement and subsequently load. Sensor load resistance, in this thesis, is defined as the force that is required to fully deform the capacitive transducer of just the sensor itself. The load resistance of the sensor must be reduced as much as possible to ensure the sensor is able to measure a wide range of loads. For example, if it took 1000 N to fully deform only the sensor itself, then the sensor in combination with a spring member would not really be feasible to measure loads less than 1000 N. In other words, it is best that the inherent load resistance of the sensor is small and that a majority of the load resistance is from the spring member. Strain gauges are a good example of a sensor with a low load resistance as the metallic wire is embedded in a flexible membrane that is very easy to deform. The load capacity of a strain gauge load cell is determined by the load capacity of the deformable spring member. For the sensor proposed in this thesis, it is advantageous for the load resistance of the sensor to be as close to 0 N as possible. However, a load resistance slightly above 0 N does not influence sensor measurements as the load resistance of the sensor is accounted for during calibration. A sensor load resistance between 0 N and 5 N would indicate that sensor would be feasible to monitor both small and large loads.

As was described in [88] and [89], the sensor packages were capable of monitoring loads exceeding 2 kN. It is important that our proposed sensor is compatible with custom spring bodies to ensure that the load capacity of the overall package can be tuned. This means that the sensor does not have to be altered to be able to be tasked in applications where both high and small load measurements are required. The proposed sensor would easily be capable of monitoring loads comparable to previously described devices (1-5x body weight force) if the sensor is compatible with a deformable spring body. With that being said, in this thesis, developing load cells with varying load capacity (less than 50 N and greater than 100 N) would indicate that the same sensor can be used to monitor a range of different forces. As was previously mentioned, the amount of deformation expected to be observed in orthopaedic applications is very small, likely never exceeding a millimeter. Therefore, it is advantageous for the maximum deformation range of the sensor to be less than a millimeter. This ensures that the full measuring range of the sensor is used. It is important to note that if the deformation range of the application is less than the measuring range of the sensor, the sensor can still be used in that application to some degree. For example, if the measuring range of the application was 0.1 mm and the capacity of the sensor was 10 mm, the sensor would still record data, but it may not provide the best representation of the data. In that scenario, it would be better that the measuring range of the application is a larger percentage of the deformation capacity of the sensor.

The final two performance variables are transmission range and power consumption. As the intended application of the sensor is to be embedded inside the body, the transmission range of the sensor package must be great enough to be able to effectively transmit data from inside the body to an external receiver. In other words, a transmission range greater than 1 m would indicate that the sensor is capable of communicating with the external receiver. Finally, the power consumption of the sensor must be low to ensure that the sensor will be able to record and transmit sensor data for a period of weeks or months on a finite power source. It is advantageous for the sensor to be able to seamlessly transition between operation modes. This would allow the sensor to go into a period of sleep to preserve battery life when transmissions are not required. To develop quantitative power consumption targets for the proposed sensor package, the performance of existing sensors tasked in orthopaedic applications can be evaluated. The sensor and telemetry system described in [96] had a power consumption of approximately 5 mW. The sensor package proposed in [89] had a power consumption of 40 mW. Finally, the power consumption of the device described in [97] was 230 mW during transmission, 1.7 mW during sensor measurements, and 320 μW during standby. If the performance of our proposed sensor is comparable to these systems (less than 50 mW power consumption during maximum transmission), and is capable of transitioning between operation modes, then our package would be feasible to record sensor measurements over a long period of time on a finite power supply. In applications such as bone healing, the sensor would be easily capable of monitoring the full extent of the healing process, which typically lasts from a few months to a year. In conclusion, the performance targets outlined in this section are realistic measures that all implantable load sensors should strive for (Table 1.1). Meeting these targets would identify that our proposed sensor package is comparable to, if not better than, previously described devices. This would indicate that the sensor package described in this thesis is feasible for use in orthopaedic and other biomedical applications.

Table 1.1: Summary of performance targets for implantable load sensing devices.

Performance Targets	Units	Target Value
Sensor Error	%	< 5%
Repeatability Error	%	< 5%
Creep Error	% F.S.	< 5%
Hysteresis Error	% F.S.	< 5%
Sensitivity	Signal unit/μm	> 1 signal unit/μm
Load Resistance	N	0-5 N
Load Capacity	N	> 100 N
Displacement Capacity	μm	< 1000 μm
Power Consumption	mW	< 50 mW
Transmission Range	m	> 1 m

1.6 Thesis Objectives

The specific objectives, as well as some associated hypotheses, of this work are:

1. Modify a commercially available wireless telemetric tire pressure sensor into a compact, low-power load and deformation sensor for future use in orthopaedic applications.

2. Test the proposed load and deformation sensor to determine if power management and transmission capabilities are feasible for future orthopaedic applications.

    a. It is hypothesized that the power management capabilities of the sensor package will enable the device to be tasked to measure load and deformation in both long- and short-term applications. In addition, the sensor will effectively be able to transmit through tissue.

3. Develop customizable, 3D-printed load cells capable of measuring a range of compressive loads for use in biomedical applications

    a. It is hypothesized that by changing the design of the cantilever beams used to construct the load cell spring body, the load capacity of the structure will change.

4. Test the 3D-printed load cells to determine if experimental fatigue life and failure location can be predicted using theoretical finite element analysis. In addition, test calibrated load cells to evaluate their performance in comparison to commercially available devices and proposed performance targets.

    a. It is hypothesized that the structures fabricated in Ti-6Al-4V using 3D printing will have a reduced fatigue life in comparison to theoretical model estimates due to the inherent mechanical properties of 3D-printed Ti-6Al-4V.

    b. It is hypothesized that the failure locations predicted by finite element analysis will be in the same location as the region of failure on the 3D-printed components.

5. Generate a simplistic and realistic finite element model of long bone fracture fixation to determine if the FXTH87 could be embedded within an implant to monitor the bone healing process.

1.7 Thesis Overview

In Chapter 2, the development of a wireless telemetry sensor device capable of measuring load and deformation is described. This chapter demonstrates that a commercially available tire pressure sensor can be modified to effectively monitor load and small-scale deformation. The performance of the built-in accelerometer, power management system, and telemetry system were evaluated. A proof-of-principle deformable structure was described that demonstrates how the proposed device would function in a future application. In Chapter 3, an analysis was performed to determine if design changes to the proof-of-principle deformable spring body would change the measuring capacity of the load cell. Finite element analysis was used to determine if theoretical modelling could predict the fatigue life and failure location of 3D-printed plastic and metal spring bodies. Using a functional 3D-printed load cell, comprised of the proposed sensor device and deformable spring body, the performance of said load cell was compared to performance targets derived from existing orthopaedic sensing solutions. In Chapter 4, two finite element models of the loading of fracture fixation plates were created to determine if the FXTH87 sensor package could be used to monitor the bone healing process. In Chapter 5, the findings from Chapters 2, 3, and 4 were summarized. Finally, future work related to testing and applications of the proposed sensor was discussed.

1.8 References

1. Amin, S., Achenbach, S. J., Atkinson, E. J., Khosla, S., and Melton, L. J., "Trends in fracture incidence: a population-based study over 20 years," *J. Bone Miner. Res.*, vol. 29, no. 3, pp. 581-589, Mar. 2014, doi: 10.1002/jbmr.2072.

2. Meling, T., Harboe, K., and Søreide, K., "Incidence of traumatic long-bone fractures requiring in-hospital management: a prospective age- and gender-specific analysis of 4890 fractures," *Injury*, vol. 40, no. 11, pp. 1212-1219, Nov. 2009, doi: 10.1016/j.injury.2009.06.003.

3. Joeris, A., Lutz, N., Wicki, B., Slongo, T., and Audigé, L., "An epidemiological evaluation of pediatric long bone fractures - a retrospective cohort study of 2716 pateitns from two Swiss tertiary pediatric hospitals," *BMC Pediatr.*, vol. 14, 20 Dec. 2014, Art no. 314, doi: https://doi.org/10.1186/s12887-014-0314-3.

4. Zioupos, P. and Currey, J. D., "Changes in the stiffness, strength, and toughness of human cortical bone with age," *Bone*, vol. 22, no. 1, pp. 57-66, Jan. 1998, doi: https://doi.org/10.1016/S8756-3282(97)00228-7.

5. Rachner, T. D., Khosla, S., and Hofbauer, L. C., "Osteoporosis: now and the future," *The Lancet*, vol. 377, no. 9773, pp. 1276-1287, 9-15 Apr. 2011, doi: https://doi.org/10.1016/S0140-6736(10)62349-5.

6. Burge, R., Dawson-Hughes, B., Solomon, D. H., Wong, J. B., King, A., and Tosteson, A., "Incidence and economic burden of osteoporosis-related fractures in the United States, 2005-2025," *J. Bone Miner. Res.*, vol. 22, no. 3, pp. 465-475, 4 Dec. 2009, doi: https://doi.org/10.1359/jbmr.061113.

7. Cooper, C., Campion, G., and Melton, L. J., "Hip fractures in the elderly: a world-wide projection," *Osteoporos. Int.*, vol. 2, pp. 285-289, 1992.

8. Judd, K. T. and Christianson, E., "Expedited operative care of hip fractures results in significantly lower cost of treatment," *Iowa Orthop. J.*, vol. 35, pp. 62-64, 2015.

9. Zimmermann, E. A., Busse, B., and Ritchie, R. O., "The fracture mechanics of human bone: influence of disease and treatment," *Bonekey Rep.*, vol. 4, p. 743, 2015, doi: 10.1038/bonekey.2015.112.

10. Weiss, R. J., Montgomery, S. M., Dabbagh, Z. A., and Jansson, K., "National data of 6409 Swedish inpatients with femoral shaft fractures: stable incidence between 1998 and 2004," *Injury*, vol. 40, no. 3, pp. 304-308, Mar. 2009, doi: https://doi.org/10.1016/j.injury.2008.07.017.

11. de Moraes, F. B., da Silva, L. L., Ferreira, F. V., Ferro, A. M., da Rocha, V. L., and Teixeira, K., "Epidemiological and radiological evaluation of femoral shaft

fractures: study of 200 cases," *Rev. Bras. Ortop.*, vol. 44, no. 3, pp. 199-203, 16 Nov. 2015, doi: 10.1016/S2255-4971(15)30068-9.

12. Kwong, Y., Chong, M., Hassan, A., and Kelly, R., "Severity of injuries associated with femoral fractures as a result of motor vehicle collisions," *Arch. Orthop. Trauma Surg.*, vol. 126, pp. 454-457, 23 May 2006, doi: https://doi.org/10.1007/s00402-006-0151-4.

13. AlTurki, A. A., AlAqeely, K. S., Almugren, T. S., and AlZimani, I. S., "Analysis of femoral fracture post motor vehicle accidents," *Saudi Med. J.*, vol. 40, no. 1, pp. 41-44, 2019, doi: 10.15537/smj.2019.1.21547.

14. *"Statistical abstract of the United States: 2011*," U. S. C. Bureau, Washington, DC, USA, [Online] Available: https://www.census.gov/library/publications/2010/compendia/statab/130ed.html

15. Little, N., Rogers, B., and Flannery, M., "Bone formation, remodelling and healing," *Surgery (Oxf)*, vol. 29, no. 4, pp. 141-145, Apr. 2011, doi: https://doi.org/10.1016/j.mpsur.2011.01.002.

16. Marsell, R. and Einhorn, T. A., "The biology of fracture healing," *Injury*, vol. 42, no. 6, pp. 551-555, Jun. 2011, doi: https://doi.org/10.1016/j.injury.2011.03.031.

17. Epari, D. R., Duda, G. N., and Thompson, M. S., "Mechanobiology of bone healing and regeneration: in vivo models," *Proc. Inst. Mech. Eng. H J Eng. Med.*, vol. 224, no. 12, pp. 1543-1553, 30 Apr. 2010, doi: 10.1243/09544119JEIM808.

18. Glatt, V., Evans, C. H., and Tetsworth, K., "A concert between biology and biomechanics: the influence of the mechanical environment on bone healing," *Front. Physiol.*, vol. 7, 24 Ja. 2017, Art no. 678, doi: https://doi.org/10.3389/fphys.2016.00678.

19. Bone, L. B., Johnson, K. D., Weigelt, J., and Scheinberg, R., "Early versus delayed stabilization of femoral fractures. A prospective randomized study," *J. Bone Joint Surg. Am.*, vol. 71, pp. 336-340, 1989.

20. Taljanovic, M. S., Jones, M. D., Ruth, J. T., Benjamin, J. B., Sheppard, J. E., and Hunter, T. B., "Fracture Fixation," *RadioGraphics*, vol. 23, no. 6, pp. 1569-1590, Dec. 2003.

21. Brumback, R. J. and Virkus, W. W., "Intramedullary nailing of the femur: reamed versus nonreamed," *J. Am. Acad. Orthop. Surg.,* vol. 8, no. 2, pp. 83-90, Mar. 2000.

22. Wolinsky, P. R., McCarty, E., Shyr, Y., and Johnson, K., "Reamed intramedullary nailing of the femur: 551 cases," *J. Trauma*, vol. 46, no. 3, pp. 392-399, Mar. 1999.

23. Oh, J. K., Bae, J. H., Oh, C. W., Biswal, S., and Hur, C. R., "Treatment of femoral and tibial diaphyseal nonunions using reamed intramedullary nailing without bone graft," *Injury*, vol. 39, no. 8, pp. 952-959, Aug. 2008, doi: https://doi.org/10.1016/j.injury.2008.02.024.

24. Hak, D. J., Stanley, S., and Goulet, J. A., "Success of exchange reamed intramedullary nailing for femoral shaft nonunion or delayed union," *J. Orthop. Trauma*, vol. 14, no. 3, pp. 178-182, Apr. 2000.

25. Ricci, W., Gallagher, B., and Haidukewych, G. J., "Intramedullary nailing of femoral shaft fractures: current concepts," *J. Am. Acad. Orthop. Surg.*, vol. 17, no. 5, pp. 296-305, May 2009.

26. Spinelli, M. S., Marini, E., Daolio, P. A., and Piccioli, A., "Atypical diaphyseal femoral fractures: considerations on surgical technique," *Injury*, vol. 50, 2, pp. S65-S69, Jul. 2019, doi: https://doi.org/10.1016/j.injury.2019.01.048.

27. Papadokostakis, G., Papakostidis, C., Dimitriou, R., and Giannoudis, P. V., "The role and efficacy of retrograding nailing for the treatment of diaphyseal and distal femoral fractures: a systematic review of the literature," *Injury*, vol. 36, no. 7, pp. 813-822, Jul. 2005, doi: https://doi.org/10.1016/j.injury.2004.11.029.

28. Harris, I., Hatfield, A., and Walton, J., "Assessing leg length discrepancy after femoral fracture: clinical examination or computed tomography?," *ANZ. J. Surg.*, vol. 75, pp. 319-321, 2005.

29. Reina, R., Vilella, F. E., Ramirez, N., Valenzuela, R., Nieves, G., and Foy, C. A., "Knee pain and leg-length discrepancy after retrograde femoral nailing," *Am. J. Orthop.*, vol. 36, pp. 325-328, 2007.

30. Willeumier, J. J., Kaynak, M., van der Zwaal, P., Meylaerts, S. A. G., Mathijssen, N. M. C., Jutte, P. C., Tsagozis, P., Wedin, R., van de Sande, M. A. J., Fiocco, M., and Dijkstra, P. D. S., "What factors are associated with implant breakage and revision after intramedullary nailing for femoral metastases," *Clin. Orthop. Relat. Res.*, vol. 476, no. 9, pp. 1823-1833, Sept. 2018, doi: 10.1007/s11999.0000000000000201.

31. Egol, K. A., Kubiak, E. N., Fulkerson, E., Kummer, F. J., and Koval, K. J., "Biomechanics of locked plates and screws," *J. Orthop. Trauma*, vol. 18, no. 8, pp. 488-493, Sept. 2004.

32. Perren, S. M., "Evolution of the internal fixation of long bone fractures. The scientific basis of biological internal fixation: choosing a new balance between stability and biology," *J. Bone Joint Surg. Br.*, vol. 84, pp. 1093-1110, 2002.

33. Cordey, J., Borgeaud, M., and Perren, S. M., "Force transfer between the plate and the bone: relative importance of the bending stiffness of the screws friction between plate and bone," *Injury*, vol. 31, 3, pp. C21-C28, 2000.

34. Borgeaud, M., Cordey, J., Leyvraz, P., and Perren, S. M., "Mechanical analysis of the bone to plate interface of the LC-DCP and of the PC-FIX on human femora," *Injury*, vol. 31, 3, pp. C29-C36, 2000.

35. Frigg, R., "Locking compression plate (LCP). an osteosynthesis plate based on the dynamic compression plate and the point contact fixator (PC-Fix)," *Injury*, vol. 32, 2, pp. 63-66, 2001.

36. Sommer, C., Gautier, E., Müller, M., Helfet, D. L., and Wagner, M., "First clinical results of the locking compression plate (LCP)," *Injury*, vol. 34, 2, pp. B43-B54, 2003.

37. Wagner, M., "General principles for the use of the LCP," *Injury*, vol. 34, 2, pp. B31-B42, 2003.

38. Miller, D. L. and Goswami, T., "A review of locking compression plate biomechanics and their advantages as internal fixators in fracture healing," *Clin. Biomech.*, vol. 22, no. 10, pp. 1049-1062, Dec. 2007, doi: https://doi.org/10.1016/j.clinbiomech.2007.08.004.

39. Taitsman, L. A., Lynch, J. R., Agel, J., Barei, D. P., and Nork, S. E., "Risk factors for femoral nonunion after femoral shaft fracture," *J. Trauma*, vol. 67, no. 6, pp. 1389-1392, Dec. 2009, doi: 10.1097/TA.0b013e318182afd0.

40. Wu, C. C., "An improved surgical technique to treat femoral shaft malunion: revised reamed intramedullary nailing technique," *Arch. Orth. Traum. Surg.*, vol. 121, pp. 265-270, May 2001, doi: https://doi.org/10.1007/s004020000222.

41. Tzioupis, C. and Giannoudis, P. V., "Prevalence of long-bone non-unions," *Injury*, vol. 38, 2, pp. S3-S9, May 2007, doi: https://doi.org/10.1016/S0020-1383(07)80003-9.

42. Rodriguez, E. K., Boulton, C., Weaver, M. J., Herder, L. M., Morgan, J. H., Chacko, A. T., Appleton, P. T., Zurakowski, D., and Vrahas, M. S., "Predictive factors of distal femoral fracture nonunion after lateral locked plating: a retrospective multicenter case-control study of 283 fractures," *Injury*, vol. 45, no. 3, pp. 554-559, Mar. 2014, doi: https://doi.org/10.1016/j.injury.2013.10.042.

43. Henschel, J., Tsai, S., Fitzpatrick, D. C., Marsh, J. L., Madey, S. M., and Bottlang, M., "Comparison of 4 methods for dynamization of locking plates: differences in the amount and type of fracture motion," *J. Orthop. Trauma*, vol. 31, no. 10, pp. 531-537, Oct. 2017.

44. Leow, J. M., Clement, N. D., Tawonsawatruk, T., Simpson, C. J., and Simpson, A. H. R. W., "The radiographic union scale in tibial (RUST) fractures: reliability of the outcome measure at an independent centre," *Bone Joint Res.*, vol. 5, no. 4, pp. 116-121, 12 Apr. 2016, doi: https://doi.org/10.1302/2046-3758.54.2000628.

45. Bhandari, M., Guyatt, G. H., Swiontkowski, M. F., Tornetta, P., Sprague, S., and Schemitsch, E. H., "A lack of consensus in the assessment of fracture healing among orthopaedic surgeons," *J. Orthop. Trauma*, vol. 16, no. 8, pp. 562-566, Sept. 2002.

46. *An Introduction to MEMS (Micro-electromechanical Systems)*. Loughborough, United Kingdom: PRIME Faraday Partnership, Jan. 2002.

47. NXP Semiconductors. *FXTH870xD, Tire Pressure Monitor Sensor*; FXTH870xD Datasheet, rev. 1.6, NXP Semiconductors: Eindhoven, The Netherlands, Feb. 2019.

48. Eswaran, P. and Malarvizhi, S., "MEMS capacitive pressure sensors: a review on recent development and prospective," *Int. J. Eng. Technol.*, vol. 5, pp. 2734-2746, 2013.

49. Gilbert, M. G., "Principles of pressure transducers, resonance, damping and frequency response," *Anaesth. Intensiv. Care Med.*, vol. 13, pp. 1-6, 2012, doi: 10.1016/j.mpaic.2011.10.010.

50. Popov, V. V., Muller-Kamskii, G., Kovalevsky, A., Dzhenzhera, G., Strokin, E., Kolomiets, A., and Ramon, J., "Design and 3d-printing of titanium bone implants: brief review of approach and clinical cases," *Biomed. Eng. Lett.*, vol. 8, pp. 337-344, 12 Jul. 2018, doi: https://doi.org/10.1007/s13534-018-0080-5.

51. Schwarzkopf, R., Brodsky, M., Garcia, G. A., and Gomoll, A. H., "Surgical and functional outcomes in patients undergoing total knee replacement with patient-specific implants compared with “off-the-shelf” implants," *Orthop. J. Sports Med.*, vol. 3, no. 7, 1 Jul. 2015, doi: https://doi.org/10.1177/2325967115590379.

52. Arbab, D., Reimann, P., Brucker, M., Bouillon, B., and Lüring, C., "Alignment in total knee arthroplasty - a comparison of patient-specific implants with the conventional technique," *Knee*, vol. 25, no. 5, pp. 882-887, Oct. 2018, doi: https://doi.org/10.1016/j.knee.2018.05.017.

53. Murr, L. E., Martinez, E., Amato, K. N., Gaytan, S. M., Hernandez, J., Ramirez, D. A., Shindo, P. W., Medina, F., and Wicker, R. B., "Fabrication of metal and alloy components by additive manufacturing: examples of 3d materials science," *J. Mater. Res. Technol.*, vol. 1, no. 1, pp. 42-54, Jun. 2012, doi: https://doi.org/10.1016/S2238-7854(12)70009-1.

54. Mohamed, O. A., Masood, S. H., and Bhowmik, J. L., "Optimization of fused deposition modeling process parameters: a review of current research and future prospects," *Adv. Manuf.*, vol. 3, pp. 42-53, 25 Feb. 2015, doi: 10.1007/s40436-014-0097-7.

55. Dawoud, M., Taha, I., and Ebeid, S. J., "Mechanical behaviour of ABS: an experimental study using FDM and injection moulding techniques," *J. Manuf.*

Process, vol. 21, pp. 39-45, Jan. 2016, doi: https://doi.org/10.1016/j.jmapro.2015.11.002.

56. Wang, S., Ma, Y., Deng, Z., Zhang, S., and Cai, J., "Effects of fused deposition modeling process parameters on tensile, dynamic mechanical properties of 3d printed polylactic acid materials," *Polym Test*, vol. 86, p. 106483, Jun. 2020, doi: https://doi.org/10.1016/j.polymertesting.2020.106483.

57. Mohamed, O. A., Masood, S. H., and Bhowmik, J. L., "Characterization and dynamic mechanical analysis of PC-ABS material processed by fused deposition modelling: an investigation through I-optimal response surface methodology," *Measurement*, vol. 107, pp. 128-141, Sept. 2017, doi: https://doi.org/10.1016/j.measurement.2017.05.019.

58. Rankouhi, B., Javadpour, S., Delfanian, F., and Letch, T., "Failure analysis and mechanical characterization of 3d printed ABS with respect to layer thickness and orientation," *J. Fail. Anal. and Preven.*, 3 May 2016, doi: 10.1007/s11668-016-0113-2.

59. Bhavar, V., Kattire, P., Patil, V., Khot, S., Gujar, K., and Singh, R., "A review on powder bed fusion technology of metal additive manufacturing," in *4th International conference and exhibition on Additive Manufacturing Technologies-AM-2014*, Banglore, India, Sept. 2014.

60. Oliveira, J. P., Santos, T. G., and Miranda, R. M., "Revisiting fundamental welding concepts to improve additive manufacturing: from theory to practice," *Prog. Mater. Sci.*, vol. 107, p. 100590, Jan. 2020, doi: https://doi.org/10.1016/j.pmatsci.2019.100590.

61. Reijonen, J., Revuelta, A., Riipinen, T., Ruusuvuori, K., and Puukko, P., "On the effect of shielding gas flow on porosity and melt pool geometry in laser powder bed fusion additive manufacturing," *Addit. Manuf.*, vol. 32, p. 101030, Mar. 2020, doi: https://doi.org/10.1016/j.addma.2019.101030.

62. *Laser Additive Manufacturing: Materials, Design, Technologies, and Applications* (Woodhead Publishing Series in Electronic and Optical Materials: Number 88). Sawston, United Kingdom: Woodhead Publishing, 2017.

63. Cunningham, R., Nicolas, A., Madsen, J., Fodran, E., Anagnostou, E., Sangid, M. D., and Rollet, A. D., "Analyzing the effects of powder and post-processing on porosity and properties of electron beam melted Ti-6Al-4V," *Mater. Res. Lett.*, vol. 5, no. 7, pp. 516-525, 23 Jun. 2017, doi: https://doi.org/10.1080/21663831.2017.1340911.

64. Ngo, T. D., Kashani, A., Imbalzano, G., Nguyen, K. T. Q., and Hui, D., "Additive manufacturing (3d printing): a review of materials, methods, applications and challenges," *Compos. B. Eng.*, vol. 143, pp. 172-196, 15 Jun. 2018, doi: https://doi.org/10.1016/j.compositesb.2018.02.012.

65. Javaid, M. and Haleem, A., "Additive manufacturing applications in orthopaedics: a review," *J. Clin. Orthop. Trauma*, vol. 9, no. 3, pp. 202-206, Sept. 2018, doi: https://doi.org/10.1016/j.jcot.2018.04.008.

66. Wong, K. C., "3D-printed patient-specific applications in orthopedics," *Orthop. Res. Rev.*, vol. 8, pp. 57-66, 14 Oct. 2016, doi: 10.2147/ORR.S99614.

67. Lopez-Heredia, M. A., Goyenvalle, E., Aguado, E., Pilet, P., Leroux, C., Dorget, M., Weiss, P., and Layrolle, P., "Bone growth in rapid prototyped porous titanium implants," *J. Biomed. Mater. Res. A*, vol. 85A, no. 3, pp. 664-673, 17 Sept. 2007.

68. Harrysson, O. L. A., Cansizoglu, O., Marcellin-Little, D. J., Cormier, D. R., and West, H. A., "Direct metal fabrication of titanium implants with tailored materials and mechanical properties using electron beam melting technology," *Mater. Sci. Eng. C*, vol. 28, no. 3, pp. 366-373, 1 Apr. 2008, doi: https://doi.org/10.1016/j.msec.2007.04.022.

69. Heinl, P., Müller, L., Körner, C., Singer, R. F., and Müller, F. A., "Cellular Ti-6Al-4V structures with interconnected macro porosity for bone implants fabricated by selective electron beam melting," *Acta Biomater.*, vol. 4, no. 5, pp. 1536-1544, Sept. 2008, doi: https://doi.org/10.1016/j.actbio.2008.03.013.

70. *ISO 13485: Medical devices - Quality management systems - Requirements for regulatory purposes*, International Organization for Standardization, Geneva, Switzerland, 2016.

71. Qiu, C., Adkins, N. J. E., and Attallah, M. M., "Microstructure and tensile properties of selectively laser-melted and of HIPed lased-melted Ti-6Al-4V," *Mater. Sci. Eng. A Struct. Mater.*, vol. 578, pp. 230-239, Aug. 2013, doi: https://doi.org/10.1016/j.msea.2013.04.099.

72. Murr, L. E., Esquivel, E. V., Quinones, S. A., Gaytan, S. M., Lopez, M. I., Martinez, E. Y., Medina, F., Hernandez, D. H., Martinez, E., Martinez, J. L., Stafford, S. W., Brown, D. K., Hoppe, T., Meyers, W., Lindhe, U., and Wicker, R. B., "Microstructures and mechanical properties of electron beam-rapid manufacturing Ti-6Al-4V biomedical prototypes compared to wrought Ti-6Al-4V," *Mater. Charact*, vol. 60, no. 2, pp. 96-105, Feb. 2009, doi: https://doi.org/10.1016/j.matchar.2008.07.006.

73. Koike, M., Greer, P., Owen, K., Lilly, G., Murr, L. E., Gaytan, S. M., Martinez, E., and Okabe, T., "Evaluation of titanium alloys fabricated using rapid prototyping technologies - electron beam melting and lase beam melting," *Materials*, vol. 4, no. 10, pp. 1776-1792, 10 Oct. 2011, doi: https://doi.org/10.3390/ma4101776.

74. Edwards, P. and Ramulu, M., "Fatigue performance evaluation of selective laser melted Ti-6Al-4V," *Mater. Sci. Eng. A Struct. Mater.*, vol. 598, pp. 327-337, 24 Jan. 2014.

75. Sterling, A., Shamsaei, N., Torries, B., and Thompson, S. M., "Fatigue behaviour of additively manufactured Ti-6Al-4V," *Procedia Engineering*, vol. 133, pp. 576-589, 2015.

76. Edwards, P., O'connor, A., and Ramulu, M., "Electron beam additive manufacturing of titanium components: properties and performance," *J. Manuf. Sci. Eng.*, vol. 135, no. 6, p. 061016, Dec. 2013.

77. Rafi, K. H., Karthik, N. V., Starr, T. L., and Stucker, B. E., "Mechanical property evaluation of Ti-6Al-4V parts made using electron beam melting," in *Solid Freeform Fabrication Symposium, SFF23*, Laboratory for Freeform Fabrication at The University of Texas at Austin, 2012.

78. Leuders, S., Thöne, M., Riemer, A., Niendorf, T., Tröster, T., Richard, H. A., and Maier, H. J., "On the mechanical behavious of titanium alloy TiAl6V4 manufactured by selective laser melting: Fatigue resistance and crack growth performance," *Int. J. Fatigue*, vol. 48, pp. 300-307, Mar. 2013, doi: https://doi.org/10.1016/j.ijfatigue.2012.11.011.

79. Benedetti, M., Torresani, E., Leoni, M., Fontanari, V., Bandini, M., Pederzolli, C., and Potrich, C., "The effect of post-sintering treatments on the fatigue and biological behaviour of Ti-6Al-4V ELI parts made by selective laser melting," *J. Mech. Behav. Biomed. Mater.*, vol. 71, pp. 295-306, July 2017, doi: https://doi.org/10.1016/j.jmbbm.2017.03.024.

80. Günther, J., Leuders, S., Koppa, P., Tröster, T., Henkel, S., Biermann, H., and Niendorf, T., "On the effect of internal channels and surface roughness on the high-cycle fatigue performance of Ti-6Al-4V processed by SLM," *Mater. Des.*, vol. 143, pp. 1-11, 5 April 2018, doi: https://doi.org/10.1016/j.matdes.2018.01.042.

81. P3 America Inc. *Popular types of load cells for weighing applications*, P3 America Inc.: San Diego, CA, USA, 19 Nov. 2019.

82. Hoffmann, K., *An introduction to stress analysis and transducer design using strain gauges*. Darmstadt, Germany: HBM.

83. Clark, J. W., Neuman, M. R., Olson, W. H., Peura, R. A., Primiano, F. P., Siedband, M. P., Webster, J. G., and Wheeler, L. A., J. G. Webster, Ed. *Medical Instrumentation: Application and Design*, 4th ed. Hoboken, NJ, USA: John Wiley & Sons, Inc., 3 Feb. 2009.

84. Loadstar Sensors. *iLoad Mini stainless steel miniature load cell*, Loadstar Sensors: Fremont, CA, USA, 1 Apr. 2010.

85. RDP Electrosense Inc. *Capacitive load cell type mcl*; document CD1048K, RDP Electrosense Inc.: Pottstown, PA, USA.

86. International Organization of Legal Metrology. *Metrological Regulation for Load Cells*; Document R60, International Organization of Legal Metrology: Paris, France, 19 Nov. 2015. [Online]. Available: https://assets.publishing.service.gov.uk/government/uploads/system/uploads/attachment_data/file/484413/OIML_R60-1_4CD_clean_version.pdf.

87. McGrath, M. J. and Scanaill, C. N., *Sensor technologies: healthcare, wellness, and environmental applications*. Berkeley, CA, USA: Apress, 2013.

88. Damm, P., Graichen, F., Rohlmann, A., Bender, A., and Bergmann, G., "Total hip joint prosthesis for in vivo measurement of forces and moments," *Med. Eng. Phys.*, vol. 32, pp. 95-100, 2010, doi: 10.1016/j.medengphy.2009.10.003.

89. D'Lima, D. D., Townsend, C. P., Arms, S. W., Morris, B. A., and Colwell, C. W., "An implantable telemetry device to measure intra-articular tibial forces," *J. Biomech.*, vol. 38, pp. 299-304, 2005, doi: 10.1016/j.jbiomech.2004.02.011.

90. Umbrecht, F., Wägli, P., Dechand, S., Gattiker, F., Neuenschwander, J., Sennhauser, U., and Hierold, C., "Wireless implantable passive strain sensor: design, fabrication, and characterization," *J. Micromech. Microeng.*, vol. 20, p. 085005, 2010.

91. Mencattelli, M., Donati, E., Cultrone, M., and Stefanini, C., "Customized load cell for three-dimensional force-moment measurements in orthodontics," in *5th IEEE RAS & EMBS International Conference on Biomedical Robotics and Biomechatronics (BioRob)*, São Paulo, Brazil, 2014, pp. 238-243.

92. Wilson, D. C., Niosi, C. A., Zhu, Q. A., Oxland, T. R., and Wilson, D. R., "Accuracy and repeatability of a new method for measuring facet loads in the lumbar spine," *J. Biomech.*, vol. 39, no. 2, pp. 348-353, 2006, doi: 10.1016/j.jbiomech.2004.12.011.

93. Du, P., Lu, H., and Zhang, X., "Measuring the young's relaxation modulus of PDMS using stress relaxation nanoindentation," in *MRS Proceedings*, Boston, MA, USA, Nov. 2009, vol. 1222.

94. Taylor, S. J. G. and Walker, P. S., "Forces and moments telemetered from two distal femoral replacements during various activities," *J. Biomech.*, vol. 34, no. 7, pp. 839-848, Jul. 2001.

95. Nelson, B. D., "A smart implantable bone fixation plate providing actuation and load monitoring for orthopedic fracture healing," Doctor of Philosophy, Department of Biomedical Engineering, Michigan Technological University, 2019.

96. Graichen, F., Arnold, R., Rohlmann, A., and Bergmann, G., "Implantable 9-channel telemetry system for in vivo load measurements with orthopedic

implants," *IEEE Trans. Biomed. Eng.*, vol. 54, pp. 253-261, 2007, doi: 10.1109/tbme.2006.886857.

97. Crescini, D., Sardini, E., and Serpelloni, M., "Design and test of autonomous sensor for force measurements in human knee implants," *Sens. Actuators A Phys.*, vol. 166, pp. 1-8, 2011, doi: 10.1016/j.sna.2010.12.010.

Chapter 2

2 Development of a Wireless Telemetry Sensor Device to Measure Load and Deformation in Orthopaedic Applications

2.1 Introduction

As described in Chapter 1, instrumentation of sensor packages within orthopaedic implants has long been a challenge due to requirements related to the size of the sensor package, the need for wireless telemetry, and low-power consumption [1,2]. Embedded sensors can be tasked to measure load, strain, temperature, and acceleration. These variables can allow scientists and clinicians to diagnose and monitor implant wear, implant migration, tissue infection, and other factors such as bone healing. In vivo implant data aids in improving orthopaedic implant design and patient rehabilitation practices. Although numerous instrumented implants embedded with sensors have been developed to measure load and strain, deficiencies remain. Most sensor packages are too large to be incorporated into smaller orthopaedic components, such as fracture fixation plates, intervertebral spinal fusion cages, and high tibial osteotomy implants, to name a few. These packages are not limited by the size of the sensor itself, but also by the size of accompanying signal processing, wireless telemetry, and power-management aspects. There is a clear need for a miniature sensor package – with integrated power management and radio frequency (RF) transmission components – that is capable of measuring load and strain inside smaller orthopaedic implants.

Much work has been done by others to develop wireless telemetric sensor packages capable of measuring and transmitting in-vivo load, strain, displacement, temperature, and acceleration. Telemetric sensor packages have been embedded within larger orthopaedic components such as shoulder [3], hip [4–10], knee replacements [11–16], external fixation devices [17,18], and spinal implants [19,20]. Previous work with embedded sensors in internal fixation devices has been unsuccessful in intramedullary nails [21,22]. Sensor packages have been feasible in fracture fixation plates [23–27]; however, the sensorized implants tend to be bulky without featuring supporting sensors

A version of this chapter has been published in the journal *Sensors* [28].

and functionalities associated with integrated microcontroller units. For example, supporting sensors for variables such as acceleration, temperature, pH, and biomarkers are not essential for direct load and displacement measurements, but can provide useful additional information about the environment surrounding the implant.

Most instrumented implants utilize a 9-channel telemetry system for in-vivo load measurements developed by Graichen et al. [29]. To make load and strain measurements, this system features multiple semiconductor strain gauges connected to a transmitter circuit that sends data through an RF transmitter. The 9-channel telemetry package is very effective at obtaining accurate load measurements over a long period of time. The disadvantage of this telemetry sensor package is that it is too large to be incorporated within smaller orthopaedic components, but it has been shown to be feasible in shoulder, hip, knee, and vertebral body replacements. The 9-channel telemetry package occupies a large volume within the orthopaedic components. In comparison, the device proposed in this study is significantly smaller in size and may only occupy a small internal region of the implant, but it does not have multiple channels dedicated to load measurements. In larger components, it may be advantageous to use the 9-channel system with increased measurement capability. However, in smaller orthopaedic components, such as spinal fusion cages, the proposed device would be advantageous as it is feasible for use in measuring a single compressive load.

Many previously described embedded sensors have used inductive coupling as a power source, as it eliminates the need to periodically replace a battery; however, this method is limited as to when and where measurements can be taken, due to the lack of an internal power supply. To make measurements with such a device, patients must strap a metallic coil around the external surface of the body in the region where the sensor package is located. Additionally, the external coil needs to be periodically recharged or wired to a power supply. In cases where continuous monitoring is necessary, alternative methods of power management are required. Internal battery sources are rarely used due to their limited lifespan and the risk of chemical exposure, however, they are beneficial in applications where measurements are taken over shorter time periods, such as monitoring implant strain during bone healing. A piezoresistive energy harvesting system that powers an orthopaedic implant through body movement would be the ideal solution as it allows for long-term continuous monitoring and data transfer. Energy harvesting has been proven to be successful in total knee replacements [30]. Alternatively, energy harvesting from human kinetics remains a challenge in other orthopaedic implants, as it is not capable of generating sufficient levels of current necessary for data acquisition, storage, and transmission in most low-power telemetry sensor packages [31–33].

Another approach, similar to the 9-channel telemetry system, was developed by D'Lima et al. [11] and Kaufman et al. [14] to measure intra-articular tibial loads. This method also features strain gauges placed in strategic locations around the tibial tray to determine the force on each load cell and the center of pressure. The load cells connect to signal conditioning equipment, an analog to digital converter (ADC), and a micro-RF transmitter. The tibial package, although successful, still faces similar size and power management restrictions as the previously described 9-channel telemetry system.

A telemetric intramedullary nail to monitor fracture healing was developed in [21]. A printed circuit board (PCB) and semiconductor strain gauge were used to measure anterior-posterior nail strain and axial compression forces in a small orthopaedic component. However, this method of measuring load and strain was not feasible for implementation within an intramedullary nail as this package was not able to effectively monitor load changes. The common theme of successful sensor packages is the method of load and strain transduction, inductive coupling power supply, and the size of orthopaedic implants they are embedded within. These packages all feature an array of strain gauges connected to signal processing equipment and an RF transmitter and are situated inside larger orthopaedic components. For embedded sensing devices to be successful in smaller orthopaedic components, an alternative mechanism of load and strain transduction must be developed.

Recent advancements in the field of automotive sensor design, specifically microelectromechanical system (MEMS)-based technology, have made alternative methods of load and strain transduction feasible for implantation within orthopaedic components. The FXTH87 (Figure 2.1) is a commercially available tire-pressure sensor package developed by NXP Semiconductors (Eindhoven, The Netherlands). This wireless package includes a pressure sensor, a two-axis accelerometer, and a temperature sensor. With the modifications proposed in this report, this package is ideally suited for future use in orthopaedic applications as it can be incorporated inside small enclosures and has the necessary components to record and transmit sensor data.

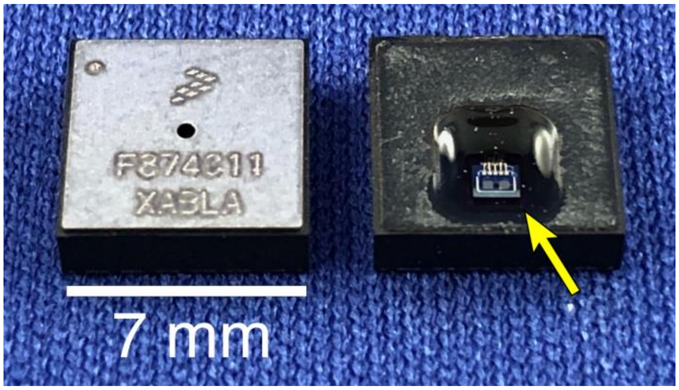

Figure 2.1: FXTH87 tire pressure sensor component. The intact package, as provided by the manufacturer is shown on the left. On the right, the protective cover has been removed, exposing the capacitive transducer (arrow).

This chapter proposes technical modifications to a commercially available wireless telemetric tire-pressure sensor that converts it into a compact, low-power, load and displacement sensor that may be feasible for future use in orthopaedic applications. The full range of physical deformation of the capacitive transducer was quantified. A relationship was reported between compressive deformation and output signal value from the sensor package. In addition, the sensor package was calibrated to measure the load required to cause the compressive deformation. In the event that the sensor package would be used to track activity or to activate sensor transmissions, the two-axis accelerometer was calibrated over a range of ±5 g. The exact power requirements and RF transmission distances were obtained in order to estimate its feasibility for future use in an orthopaedic implant. To illustrate the feasibility of our package, the modified sensor was calibrated when embedded inside a small-scale custom strain member that was designed to transduce compression. The resulting correlation between deformation and signal, accompanied with its size and functionality, make this device an effective solution for measuring load, displacement, acceleration, and temperature. This approach may be applicable for use in many small orthopaedic implants, including fracture fixation plates, intervertebral spinal fusion cages, and high tibial osteotomy implants.

2.2 Methods

2.2.1 FXTH87 Sensor Characteristics

As was described in Section 1.2, the proposed sensor package, the FXTH870511DT1 (FXTH87), features an 8-bit 4 MHz CPU, 315/434 MHz RF transmitter, 6 channel 10-bit ADC, 125 kHz LF receiver, pressure sensor, dual-axis accelerometer, temperature sensor, and additional components, making the FXTH87 a fully functional wireless telemetry package [34]. All sensors, transmitting equipment, memory, and CPU for the FXTH87 are housed inside a miniature package measuring 7 mm × 7 mm × 2 mm, making it one of the smallest pressure sensing packages in the world. The FXTH87 utilizes a capacitive pressure transducer to obtain pressure measurements. For the sensor configuration described in this thesis, instead of measuring air pressure, the onboard capacitive transducer was modified (as described below) and then calibrated to measure load and deformation by manipulating the distance between the electrode and the diaphragm using a 3D-printed mechanical indenter.

2.2.2 FXTH87 Circuit Board Design

A PCB for the main sensor chip and surrounding circuitry was designed in EAGLE Autodesk (Autodesk, San Rafael, CA, USA) following basic principles for optimal RF transmission [35]. Two different PCB’s were designed. The first board was only capable of transmitting RF signals and was 19 mm × 16 mm × 0.4 mm (excluding circuit components). The second board acted as a transceiver which could send RF signals and receive LF signals; the received LF signals act to control the functionality and programming of the FXTH87. The additional functionality came at the cost of a slightly larger size: 26 mm × 16 mm × 0.4 mm. For the purpose of the experiments in this paper, the LF functionality was not required, and the one-way transmitter PCB was used (Figure 2.2).

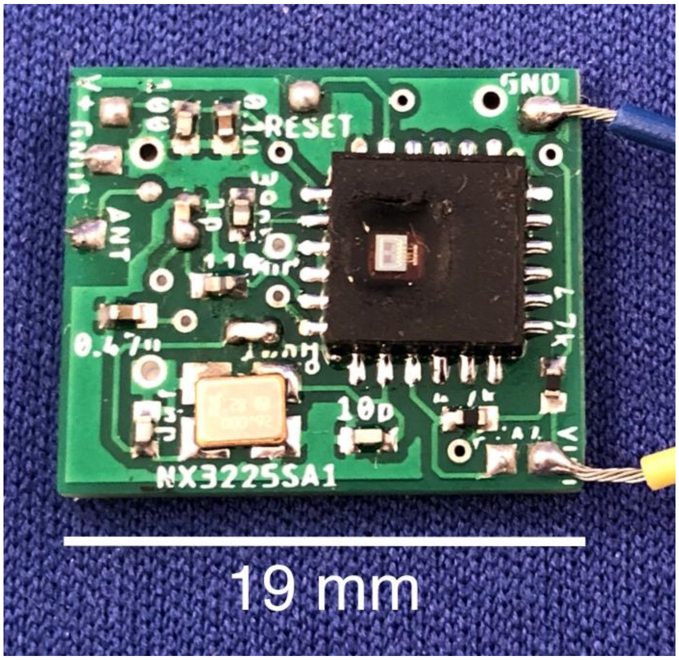

Figure 2.2: FXTH87 tire pressure sensor mounted to custom PCB without LF capabilities.

It is important to note that a dedicated antenna component was not required in this design. RF communication was achieved by transmitting from a copper pad (1.1 mm × 1.1 mm), which is labeled as ANT on the left side of the PCB (Figure 2.2). Given that the FXTH87 is a quad flat no-lead (QFN) electrical component, reflow soldering was performed using a heated plate following the approximate reflow profile for NXP's QFN components [36].

The FXTH87 sensors were flashed using demonstration code and were set to transmit continuously at a rate of 25 Hz (confirmed through oscilloscope tests). An FRDMKW019032 (FRDM) NXP transceiver (NXP Semiconductors) was used to receive the RF messages from the FXTH87 sensor. The FRDM transceiver sent the information via serial communication to a graphical user interface (GUI) provided by the vendor.

The GUI displayed outputs including pressure, temperature, acceleration, voltage, and various status bits. The transducer data was recorded with 9-bit precision (512 analog-to-digital counts). Given that the FXTH87 sensor is being used to quantify deformation, the discretized data was recorded in arbitrary counts, as opposed to the manufacturer's default setting of pressure in kPa. The temperature sensor has a reported precision of one degree Celsius over a range from −54 °C to 199 °C, however, the accuracy of the temperature sensor is not investigated in this chapter. The FXTH87 incorporates dual-axis accelerometers; the Z-axis accelerometer is valid over a range of -30 *g* to 30 *g* whereas the X-axis accelerometer has a range of -10 *g* to 10 *g*. The manufacturer's specified precision of the X and Z-axis accelerometers are approximately 0.039 *g* and 0.118 *g*, respectively.

2.2.3 Modifications to FXTH87 for Deformation Sensing

To transform the FXTH87 sensor from an ambient pressure sensor to a device that could measure load, an elastic coupling medium was required that would allow a mechanical indenter to depress the capacitive transducer. Without the introduction of a suitable coupling medium, the transducer would be easily damaged by the indenter. The ideal coupling medium would be an electrically insulative, two-part elastomer with a relatively low elastic modulus. In addition, said elastomer should be non-exothermic and room-temperature vulcanized.

The material chosen for the coupling medium was a commercial polydimethylsiloxane (PDMS) elastomer, Sylgard 184 (The Dow Chemical Company, Midland, MI, USA). Sylgard 184 behaves as a nearly incompressible material as it has a Poisson's ratio ~0.5 [37]. The elastomer was applied to the external membrane of the capacitive transducer (Figure 2.3d) on ten FXTH87 sensors using a micropipette. The two-component Sylgard 184 composition followed the recommended 10 to 1 mix ratio [38]. Prior to the application of Sylgard 184 to the sensor package, the mixture was deaerated in a vacuum chamber at 50 kPa for 20 min. All ten sensors were laid flat and cured for a minimum of 48 h at room temperature before testing.

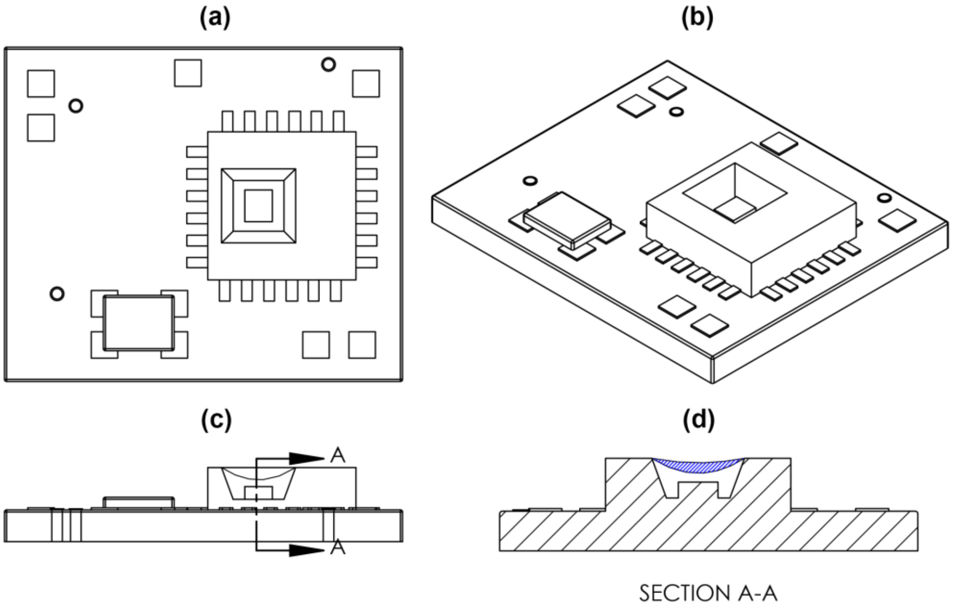

Figure 2.3: Sketch of FXTH87 on custom PCB. (a) Top view of FXTH87 and PCB. (b) Isometric view of FXTH87 and PCB. (c) Side view of FXTH87 and PCB. The Capacitive transducer membrane is defined by the concave line above the rectangular box, which depicts the location of the capacitive transducer. (d) Cross section view of the FXTH87 and PCB. Blue hatched region depicts the volume filled with Sylgard 184 on the surface of the capacitive transducer membrane.

The sensors were divided into two groups, based on the amount of Sylgard 184 applied to the external transducer membrane. The required volume of Sylgard 184 was predetermined from a micro-CT scan of the FXTH87; a 3D volume-of-interest software utility was used and found the volume of the external sensor cavity to be approximately 3 μL. The nominal prescribed volume was dispensed using a micropipette, however, variations in the deposited volume were observed due to the viscosity of uncured Sylgard 184. The actual volume of elastomer dispensed was verified gravimetrically using the known density of Sylgard 184, which is reported as 1.027 g/mL [37]. The sensors were then grouped based on the actual volume of dispensed elastomer. Group 1 and group 2 consisted of sensors with approximately 2 μL and 3 μL of Sylgard 184, respectively (Table 2.1). It is important to note that both groups had a visibly inward concave meniscus. Each group was tested to observe the effects of the elastomer volume on the maximum amount of compressive deformation that the sensor could withstand.

Table 2.1: Volume of Sylgard 184 applied to FXTH87 sensors.

Sensor (Group 1)	Sylgard 184 Volume (μL)	Sensor (Group 2)	Sylgard 184 Volume (μL)
A	2.26	F	3.44
B	1.96	G	2.75
C	2.26	H	3.24
D	2.26	I	2.85
E	2.06	J	2.95

2.2.4 Calibration of Deformation and Load

To calibrate the modified sensor package against both deformation and load, two experiments were performed. In the first case, a known value of surface deformation (i.e. indentation) was applied over the measuring range of the sensor. Compressive deformation was applied to the elastomeric coupling medium, using a commercial material testing machine (Model 3343, Instron, Norwood, MA USA) and a hemispherical-tipped indenter. The indenter was 3D-printed in polylactic acid (PLA) plastic, with a tip radius of 1.6 mm. The sensor package was supplied with 3V using a voltage supply to eliminate the need for a battery and to ensure that the voltage level remained consistent between sensors and trials. The PCB was placed directly on the non-deformable metal plate at the base of the Instron, constrained within a 3D printed mounting jig that was used to align all of the sensors directly below the indenter (Figure 2.4). The mounting jig was also clamped to the plate to eliminate any movement. Compressive load was recorded using a 50 N load cell (Model 2519-102, Instron) and the Instron Bluehill software (Instron). Compressive load and deformation were recorded at a rate of approximately 14 Hz. Two sets of experiments were carried out based on the amount of Sylgard 184 adhered to the external transducer membrane. The maximum compressive deformation applied to the sensors with 2 μL and 3 μL of Sylgard 184 was 350 μm and 400 μm, respectively. Compressive deformation was applied at a rate of 350 μm/min for sensors with 2 μL of Sylgard 184 and 400 μm/min for sensors with 3 μL of Sylgard 184, to achieve full compressive deformation of each group of sensors in the same time interval.

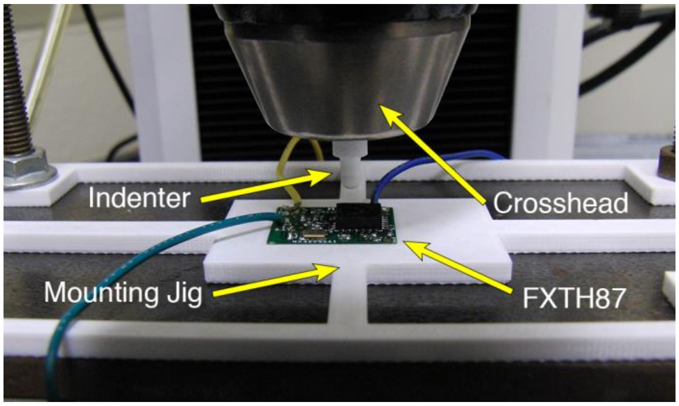

Figure 2.4: Instron 3343 applying compressive deformation to the FXTH87.

The aim of the second experiment was to calibrate a custom structural enclosure that was developed to demonstrate a proof-of-principle application of our sensor package (Figure 2.5). In other words, a custom load cell was developed and tested by combining a deformable structural component and a displacement sensor. While this enclosure is not an orthopaedic component, it is important to determine if the sensor is capable of being calibrated to measure loads in a simple deformable body. Successful calibration would indicate that the sensor is feasible to be embedded and calibrated within complex deformable bodies, such as custom orthopaedic components. The proof-of-principle deformable enclosure featured four cantilever beams designed to deflect approximately 500 µm under a compressive force. The lid of the enclosure was designed to hold a locknut and ball-point set screw with a ball radius of 1.25 mm. When a force is applied to the lid component the cantilever beams deform and the lid moves vertically downward towards the sensor. The locknut and ball-point set screw interact with capacitive transducer sensor as the enclosure deforms. The set screw acted as an adjustable indenter that allowed the starting point of the deformation to be altered. The enclosure was 3D printed in PLA using a Dremel 3D40 system (Dremel, Mt. Prospect, IL, USA); printing parameters were set to 100% infill density.

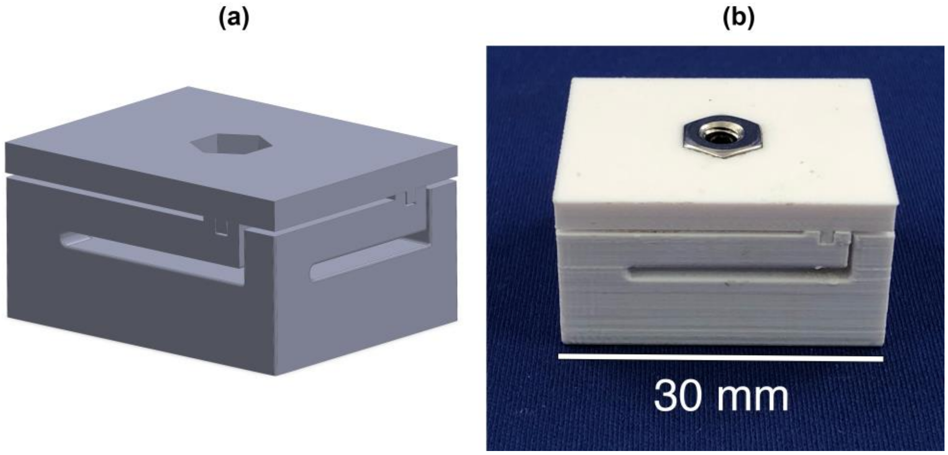

Figure 2.5: (a) SolidWorks model of compression enclosure. (b) 3D printed compression enclosure.

Calibration of the sensor package when it was embedded inside the compression enclosure was performed by applying compressive deformation to the enclosure and measuring the change in signal value and compressive load. The sensor package was held firmly inside the enclosure with wires protruding out of the base to an external power source, a DC power supply. The set screw housed in the lid was adjusted to a position that just barely came into contact with the surface of the capacitive transducer. This ensured that any amount of compression of the enclosure would result in displacement of the top plate of the capacitive transducer and increase the output signal value. Ten trials of compressive deformation were applied to the enclosure using an Instron 3343 and the flat head of a bolt measuring 1.5 cm in diameter.

A hysteresis test was performed on the compression enclosure and sensor package to determine the difference in signal output during loading and unloading cycles. During the loading phase, compressive deformation was applied to the enclosure and embedded sensor until the sensor output signal value reached its maximum capacity. The unloading phase returned the crosshead of the Instron to its original position at the start of the test. Five cycles of loading and unloading were applied to the package.

2.2.5 Acceleration Experiments

To perform an acceleration calibration, each sensor package was secured in a custom 3D printed enclosure that was mounted to a rotary table (Model PSR300, Intellidrives, Philadelphia, PA, USA) (Figure 2.6). The sensor package was oriented so that the onboard X and Z axis accelerometers were in line with the rotational acceleration axis of the table. Note that the orientation of the package could be reversed within each enclosure to measure both positive and negative acceleration. The sensor package was powered using a 3V, 120 mA·h CR1632 coin battery to eliminate the need for wires connecting to a voltage supply. Constant rotational speed was used to apply rotational acceleration to the sensor package over the range of $-5\ g$ to $+5\ g$ at intervals of $0.5\ g$. The rotary table was allowed several seconds to achieve steady state prior to each increase in acceleration. The average and standard deviation of the experimental acceleration were obtained after reaching steady state at each acceleration level.

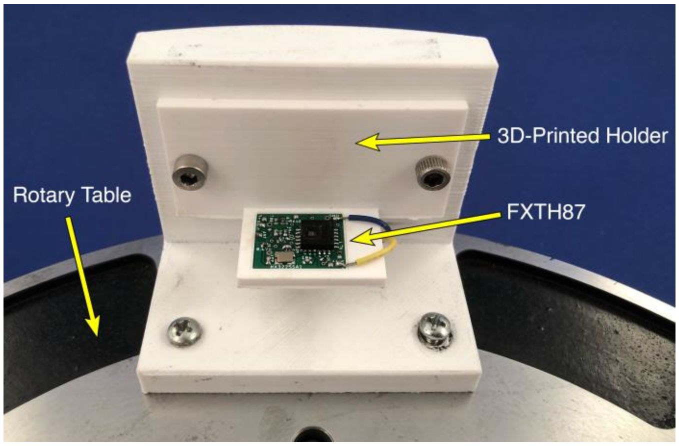

Figure 2.6: FXTH87 oriented to measure positive X-axis acceleration on rotary table.

2.2.6 Power Management

The power consumption of the FXTH87 sensor was investigated to characterize the current draw and evaluate its feasibility for use in wireless telemetric orthopaedic implants. For this experiment, the FXTH87 was programmed to transmit at 1 Hz and the transmission power was set to the nominal value of 5 dBm. The input power trace of the

FXTH87 was connected in series with a precision adapter, the µCurrent, and an oscilloscope was attached in parallel to the output terminals of the µCurrent adapter (EEVBlog, Sydney, Australia). The µCurrent adapter is a device that converts an input current to an amplified voltage for easier analysis. This device overcomes burden voltage, which is ideal since the FXTH87 circuit functions off a low voltage and minimal current draw. To achieve a clear waveform on the oscilloscope, the middle conversion factor of 1 mV/1 µA was selected on the µCurrent, however, a 1.2 Ω shunt resistor was placed in parallel between the input terminals of the µCurrent. This resulted in an effective conversion factor of 1 mV/10 µA from the µCurrent adapter to the oscilloscope.

2.2.7 RF Transmission

The ability to wirelessly transmit the sensor data from an implanted state is an important aspect of a telemetry system. To characterize the performance of the RF transmission of the FXTH87 in our proposed configuration, several tests were conducted to determine the maximum range of transmission. A baseline test was conducted in open-air, followed by tests in which the sensor was sandwiched between two layers of bovine muscle tissue (steak); tests were repeated with three different tissue thicknesses on each side of the sensor (i.e. 17.5, 35 and 52.5 mm). Three trials were performed for each condition, and the maximum observed transmission distance was averaged.

2.2.8 Data Analysis

To analyze the data, resampling was required to achieve a consistent number of data points between the recorded data from the Instron and the FXTH87 sensor package. A MATLAB script was created to import the data sets for each trial into MATLAB (MathWorks, Natick, MA, USA). The recorded data from the sensor package was resampled using the built in MATLAB function, resample. The resulting sampling rate of the transducer matched the rate of the Instron.

To determine if there was a relationship between reported signal and compressive deformation, the output signal value from the FXTH87 sensor package was plotted against compressive deformation in Prism (GraphPad, San Diego, CA, USA). Separate graphs were generated to illustrate the performance of an individual sensor and the two groups of sensors filled with different amounts of Sylgard 184. A trendline was applied to the signal versus compressive deformation graph of sensor A over a linear region of the plot ranging from 150 to 350 µm to evaluate the sensitivity. The standard deviation of the signal units over the linear portion of this graph were averaged to determine the uncertainty in indenter position when the sensor package is displaying a specific signal value. Compressive load was plotted against compressive deformation to characterize the load required to reach specific levels of displacement and the maximum internal sensor resistive force. To develop a calibration curve for the compression enclosure, ten compression trials were performed; compressive load from the Instron was plotted against output signal value from the FXTH87 sensor package. The data was fitted to a non-linear Equation (Equation 2.1) generated by Prism:

Equation 2.1: Non-linear equation that was fitted to the calibration data.

$$y(x) = A\,x/(B + x) + Cx + D$$

Using an additional compression trial, the measurement error of the load sensor was determined. To determine if the deformable enclosure and sensor exhibited hysteresis, the signal values from the sensor were plotted against load from the Instron 3343 during the cyclic deformation test.

For each of the ten sensors tested on the rotary table, the sensor data points were averaged at each acceleration level. To verify the expected linear correlation between the rotary table acceleration and the sensor acceleration, the sensor data for each board was shifted by a constant offset equal to its average sensor data with known zero acceleration. This alteration does not affect the trend in the sensor acceleration data but ensures that each sensor is calibrated to have approximately zero offset. To characterize the performance of the accelerometers, the average value and standard deviation of the experimental sensor data at each acceleration interval were plotted against the theoretical acceleration value. A linear trendline was applied to the data to generate a calibration curve for the X and Z-axis accelerometers.

The data points which were captured from the oscilloscope relating to the FXTH87 power consumption over an entire cycle were formatted using Excel software. The raw voltage data was converted to the corresponding current value using the 1 mV/10 uA conversion factor of the µCurrent adapter. The current waveform was broken up into three general regions: STOP1 (lowest power standby mode), sensor readings, and transmission. The process of sensor readings includes full sensor measurements and compensation. A noisy signal captured from the oscilloscope was subtracted off and then the average current draw for each mode was calculated using Excel. The area under the curve was used to determine the total milliamp-hours required for a 1 Hz transmission cycle. A graph displaying the FXTH87 sensor package's instantaneous current draw was plotted against time.

2.3 Results

2.3.1 Compressive Deformation Experiments

The deformation experiments from the Instron demonstrated that there was a monotonically increasing relationship between the FXTH87 output signal value and compressive deformation. The plots for sensor A were highlighted to illustrate the performance of an individual sensor. The sensitivity of the signal versus compressive deformation plot for sensor A was 2.15 signal units/µm over the linear region of the graph (Figure 2.7a). The average standard deviation of the signal value over the linear region of the graph was 2.91 signal units. This corresponds to an uncertainty in position of ±1.35 µm. The inherent internal resistive force of the modified load sensor did not exceed 1.41 ± 0.01 N (mean ± standard deviation) (Figure 2.7b).

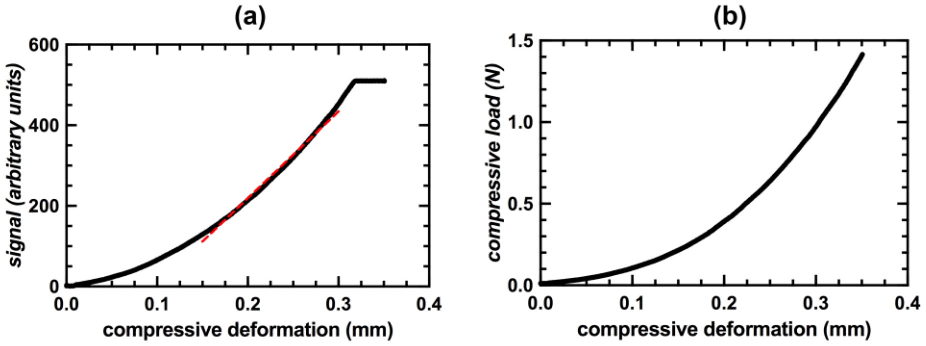

Figure 2.7: (a) FXTH87 signal value during compressive deformation for Sensor A. (b) Internal resistive force of Sensor A during compressive deformation.

The amount of compressive deformation and load required to reach the maximum output signal value was similar between sensors but never identical, even for sensors with the same amount of Sylgard 184. For the five sensors filled with 2 μL of Sylgard 184 it took 290 ± 16 μm of compressive deformation to reach the maximum output signal value (Figure 2.8a). The five sensors filled with 3 μL of Sylgard 184 took 350 ± 24 μm of compressive deformation to reach the maximum output signal value (Figure 2.8b). The maximum internal sensor resistive force required to cause complete compression of the capacitive transducer was 1.10 ± 0.07 N for sensors filled with 2 μL of Sylgard 184 and 1.19 ± 0.09 N for sensors filled with 3 μL of Sylgard 184.

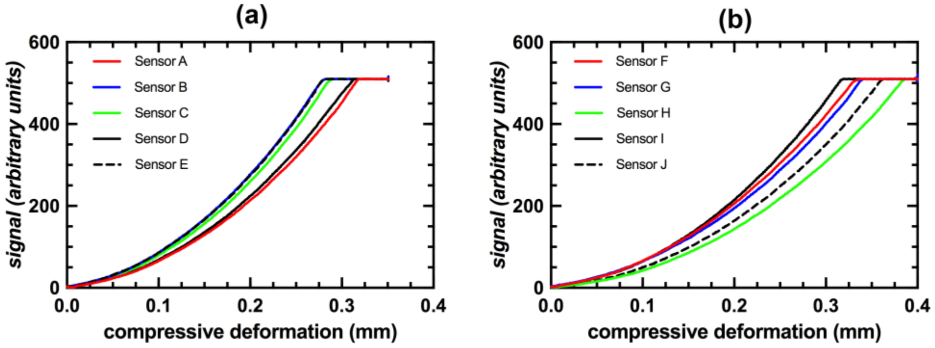

Figure 2.8: (a) FXTH signal value during compressive deformation for sensors in Group 1 (A-E). (b) FXTH signal value during compressive deformation for sensors in Group 2 (F-J).

The compression enclosure exhibited a positive relationship between compressive load and signal value with an R^2 value of 0.9992 (Figure 2.9). The average measuring error of the load sensor was approximately 2% (Figure 2.10, Table 2.2). A compressive load of approximately 35 N was required to fully compress the enclosure and the capacitive transducer. Hysteresis of the signal values corresponded to an average of less than 1 N between loading and unloading cycles (Figure 2.11). This value corresponds to a hysteresis error of less than 3%.

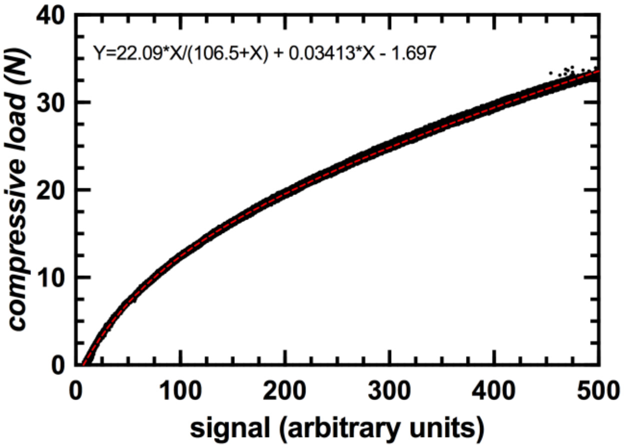

Figure 2.9: Calibration curve for sensor integrated within a 3D-printed compression enclosure.

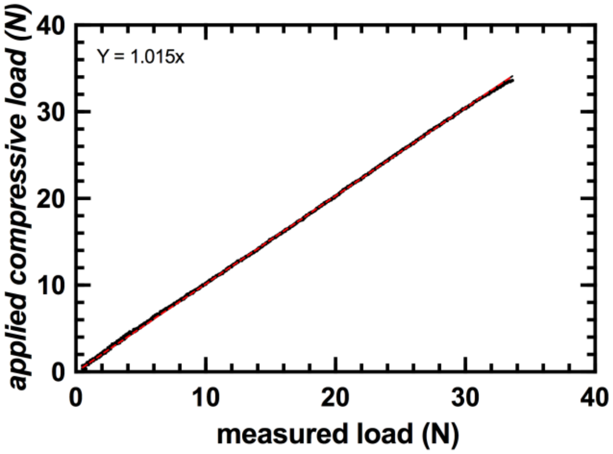

Figure 2.10: Applied compressive load from Instron vs. measured compressive load from calibrated FXTH87 and 3D-printed deformable body.

Table 2.2: Average measuring error of the calibrated FXTH87 over five ranges of signal values.

FXTH87 Signal Range (arbitrary units)	Measuring Error (percent)
0-100	4.6%
100-200	1.2%
200-300	1.5%
300-400	1.6%
400-500	1.1%
0-500	~2%

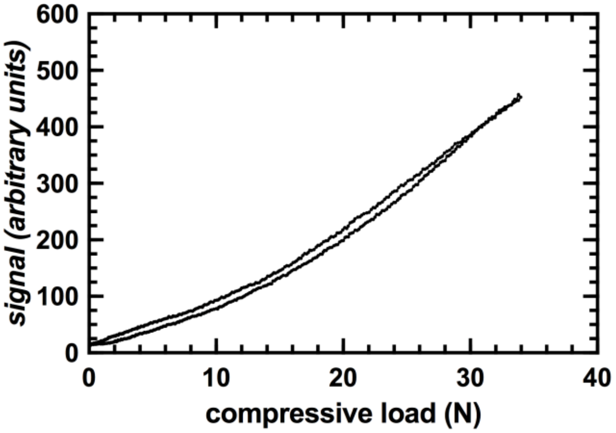

Figure 2.11: Hysteresis curve for sensor integrated within a 3D printed compression enclosure.

2.3.2 Acceleration and Power Management

The R^2 value of the linear regression analysis for the X and Z-axis acceleration was 0.9985 and 0.9966, respectively (Figure 2.12). The average standard deviation of the acceleration values for all the intervals combined was ± 0.10 *g* for X-axis acceleration and ± 0.15 *g* for Z-axis acceleration.

The average current draw of the FXTH87 while operating in standby was 14 µA, with a standard deviation of 115 µA. The average current draw while the sensor package is performing full measurements and compensations is 1.5 mA, with a standard deviation of 0.8 mA.

The highest power consumption was observed while the sensor package was transmitting RF signals and was found to have an average current draw of 6.8 mA at 3.3V, with a standard deviation of 0.7 mA (Figure 2.13). The total milliamp-hours required for one complete pulse width cycle was 4.09×10^{-5} mA·h.

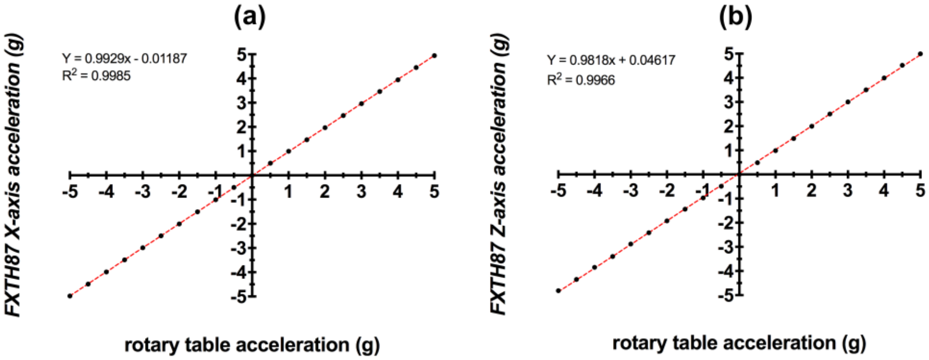

Figure 2.12: (a) Calibration curve for X-axis accelerometer for Sensors A-J. (b) Calibration curve for Z-axis accelerometer for Sensors A-J.

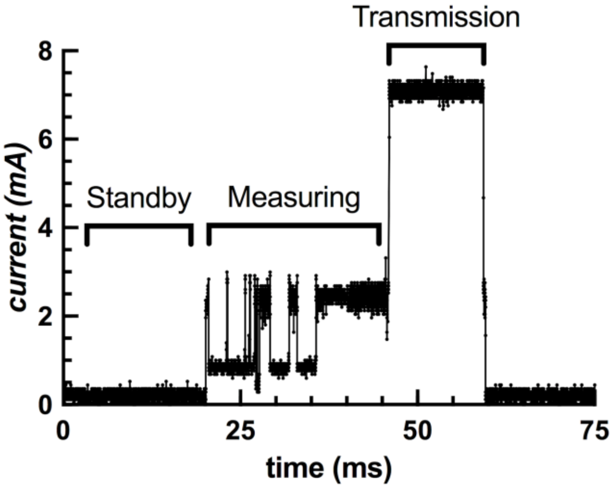

Figure 2.13: Current draw of the FXTH87 sensor package during a single transmission cycle.

2.3.3 RF Transmission

The maximum transmission distance in open air before the transceiver lost communication with the sensor was 9.5 m. Adding 17.5 mm of tissue had no discernable effect on the maximum transmission distance. Increasing the tissue depth to 35 mm and 52.5 mm caused the transmission distance to drop to 6 m and 4.5 m, respectively.

2.4 Discussion

We have demonstrated that it is feasible to modify a commercial wireless MEMS pressure sensor package to measure compressive deformation. Our investigation shows that there is a positive monotonic relationship between output signal value and the amount of compressive deformation applied. The FXTH87 tire pressure sensor package could detect very small changes in the deformation of its elastomer-coated diaphragm, allowing us to determine the position of an indenter to within ±1.35 µm. The maximum amount of compressive deformation that could be applied to the sensor ranged from 250 µm to 400 µm, depending on the amount of Sylgard 184 applied to the sensor diaphragm. This information is important because in future applications—where the sensor package is embedded—the enclosure must not exceed these deformation levels or else permanent damage may occur.

It is important to note that sensitivity and position uncertainty was determined over the region of the linear regression line (150 µm to 300 µm). The sensitivity and position uncertainty will change based on where the linear regression line is placed, however, this demonstrates that the sensor could be preloaded to ensure that it operates in the linear region. This may be useful in certain applications where the required deformation is a fraction of the full range and a linear relationship is required.

The amount of Sylgard 184 applied to the sensor package had an influence on the outcome. Sensors that were filled with more Sylgard 184 required more compressive deformation to reach the maximum signal value. This was expected since the mechanical indenter had to compress slightly more Sylgard 184 during deformation. With this information, a larger volume of Sylgard 184 could be applied to the pressure transducer to increase the amount of compressive deformation that the FXTH87 package could measure. On the contrary, the smaller volume of Sylgard 184 would be beneficial in applications such as orthopaedic sensing, as the full range of signal values can be obtained with minimal deformation. Due to the size restrictions of many implants, it is expected that an implant capable of deforming onto the sensor would only be deforming a very small amount. If deformation of the implant was larger than the capacity of the sensor, the mechanism contacting the capacitive transducer could be adjusted to prevent sensor overloading. The internal sensor resistive force was similar within each set of sensors, likely due to the small discrepancy in the amounts of Sylgard 184. It would be expected that a larger quantity of Sylgard 184 would increase the compressive load required to cause full deformation of the transducer. Although compressive deformation was applied at a linear rate, both the applied load and thus signal value were not linearly correlated with the compressive deformation. When Sylgard 184 is under compression, the stress/strain curve has a linear elastic region until strain values of approximately 55%, which is then followed by a nonlinear region [37]. During the tests performed in this study, it is expected that the Sylgard 184 remains in the linear elastic region of the stress/strain curve as two distinct phases are not observed in the data. The characteristics of the capacitive transducer are likely responsible for the observed non-linearity, as capacitance is inversely proportional to the distance between the parallel plates of the transducer ($C \propto 1/d$). Even though the signal value is not linearly correlated with deformation, within each sensor package the relationship is consistent and repeatable every time compressive deformation is applied. This repeatability allows a calibration curve to be generated for a compression enclosure with an embedded FXTH87 sensor package. The FXTH87 package was also calibrated to act as a load sensor by quantifying the relationship between the signal value and the compressive load. Once the calibration was generated, the compressive load can be directly determined by monitoring the output signal value from the FXTH87. The compact wireless telemetric sensor proposed in this study was effectively tasked to measure micrometer-level deformation and load in a small-scale compression enclosure.

Using the calibration curve that was generated for our 3D printed strain member, the FXTH87 could be used to measure both small-scale deformation and loads of up to 35 N. The small internal resistive force of the FXTH87 is inherently accounted for during the calibration of the deformable member. The error of the load sensor is low; however, it could be further reduced by performing additional calibration trials, therefore improving the quality of the calibration curve. The small increased measuring error observed over the signal range of 0-100 units was a result of a few outlier points at the early limits of the experiment. This was likely caused by the initial contact between the indenter and the elastic coupling medium. However, for the most part, the error in the signal range from 0-100 units is similar to the error of the other signal ranges. Therefore, over the majority of the measuring range of the sensor, the measuring error is closer to 1%. The sensor package is capable of being embedded within enclosures of all sizes and fabricated from any material; thus, there is no limit on the amount of load the package can measure, as long as the deformation resulting from that load is within the measurable range of 250–400 µm. This principle is utilized in many commercial load sensors with varying capacities; the same strain gauge can be used to record measurements, but the structure of the strain member is altered to change the operating range. The hysteresis exhibited between the loading and unloading cycles of the compression enclosure was a small and consistent value throughout all tests. This will allow a future user to easily correct for the small discrepancy between cycles during calibration experiments. It is expected that a majority of the observed hysteresis is a result of the plastic compression enclosure, and not due to the sensor and the applied Sylgard 184. Pure Sylgard 184 has been shown to have minor hysteresis [39]. In future applications, if minimizing hysteresis is a primary goal, it is important to embed the sensor in an enclosure with minimal inherent hysteresis.

This study has shown that there is a positive linear relationship between experimental and applied acceleration, with a constant offset that could be compensated through calibration. This result was important to obtain, as this information shows that this package is capable of measuring acceleration along two axes in enclosures of all sizes. Calibrating the accelerometers allows the possibility of using the accelerometers as a trigger to alter the measurement duty cycle of the sensor package. This scenario would be likely in the case where batteries are tasked to power the package. The accelerometers could be used to temporarily increase the duty cycle during periods of higher acceleration and then lower the duty cycle during rest. Carefully controlling the number deformation/load measurements and RF transmissions will assist in prolonging the lifetime of the battery.

The experiments relating to the power consumption of the FXTH87 were very promising, indicating the feasibility of using a coin-cell battery to power the sensor package inside orthopaedic implants. The results showed that the FXTH87 consumed about 14 ± 115 µA while operating in the lowest power standby mode. Based on the high standard deviation, this measured current usage is primarily dominated by noise, despite the attempt to correct for noise. The FXTH87 data sheet states that the current consumption in STOP1 should be about 1 µA, which suggests that power consumption could be even lower than reported here. The milliamp-hours required for a one second cycle of standby, sensor acquisitions, and transmission in the FXTH87 was found to be 4.09×10^{-5} mA·h, whereas a typical CR-1632 battery provides capacity of approximately 120 mA·h. The FXTH87 could therefore operate for about 2.9 million transmission cycles. When acquiring and transmitting at the maximum rate of 25 Hz, the average power consumption of the FXTH87 sensor package can be as low as 11 mW; in this configuration, the device would operate continuously for over 36 h from a 120 mA·h battery. During standby mode, the FXTH87 was measured to have a power consumption of 42 µW, meaning it would last at least one year with the same power source. In a scenario where the FXTH87 is embedded in an implant, it is highly unlikely that the maximum transmission rate would be required at all times; typically, the FXTH87 would be programmed to trigger transmission at its maximum capacity of 25 Hz for a brief window, lasting no more than a few minutes. This would allow a clinician to monitor the patient data during an examination, then the FXTH87 would return to standby mode to prolong the battery life of the package. In other words, the device will almost always be operating in one of two states, standby mode or at maximum transmission capacity. This is beneficial in cases where orthopaedic implants need to be monitored at several timepoints in the weeks or months following surgery. In comparison, the power consumption of the 9-channel telemetry system described in [29] is approximately 5 mW when transmitting at a rate of 125 Hz. While the power consumption of the telemetry system used to measure intra-articular tibial forces was not specified, it was stated that 40 mW was adequate to power the system [11]. The sensor package and telemetry system devised in [15] required approximately 230 mW during transmission, 1.7 mW during sensor measurements, and 320 µW during standby. The FXTH87 is comparable to the previously described telemetry packages in terms of power consumption, and thus should be feasible for use in orthopaedic applications.

Based on the RF transmission tests conducted in this paper, it is clear that the sensor package in its described configuration is capable of transmitting signals through tissue. These results are significant as it proves that a traditional antenna component is not required in this design, allowing for the size of the sensor PCB to be minimized. Noting that transmission distance decreases with increased tissue depth, it is possible that the default 5 dBm output power of the FXTH87 might need to be increased in some applications. The FXTH87 transmission output power can be adjusted through the Dynamic RF Power Correction firmware routine [34].

While the objective of the FXTH87 sensor package is similar to previously developed embedded systems, the method of measuring deformation and load described in this study presents a number of unique advantages. The FXTH87 sensor and circuit board is effectively able to record and transmit sensor data in a package that occupies a volume less than a cubic centimeter. The full extent of the size of the implantable 9-channel telemetry system and strain gauges developed in [29] is never explicitly stated. However, it is evident that the volume of this package is significantly greater than the FXTH87 package, as the telemetry system occupies a large portion of the head and stem of joint replacement implants. Similar telemetry systems developed by [11,14], face the same challenges, as the requirements for inductive coupling occupy a majority of the internal cavity of the implants. While some very small strain monitoring systems have been developed for intramedullary nails [21], [22], they have not been successful due to the poor signal strength of their respective telemetry systems and a lack of supporting strain gauges. The FXTH87 sensor package has no practical limitations on the amount of load that it can measure, as long as the deformation resulting from the applied force does not exceed the maximum deformation capability of the capacitive transducer. In the current study, tests with a compression enclosure containing the capacitive transducer resulted in load measurement error of 1-2%, which is comparable with previously described sensor packages. For example, a hip prosthesis developed by [6] that utilizes the telemetry system described in [29] was calibrated to measure forces ranging from 2 to 5 kN, with an average measuring error ranging from 0.4% to 0.9%. An instrumented tibial implant developed in [11] was calibrated to measure loads of 2000 N with average errors of around 1%.

In terms of size comparison, the three telemetry systems described in [11,15,29] all occupy a significantly larger volume than the FXTH87 package due to the transmitting circuitry and additional components required for inductive coupling. The FXTH87 is competitive in terms of low-power consumption in comparison to other devices but it is limited to transmission rates less than 25 Hz. While the FXTH87 sensor package is one of the smallest sensing packages available, it also provides more supporting components than the previously described sensing and telemetry devices. In addition to the capacitive transducer, RF transmitter and 8-bit 4 MHz central processing unit (CPU) the FXTH87 also features a temperature sensor, two axis accelerometer, 125 kHz LF receiver, internal timers and clocks, 6 channel 10-bit ADC, 16 KB of flash memory, and 512-byte RAM. The miniature size of the FXTH87 package along with the built-in components make this sensor package an effective solution to record and transmit load, deformation, temperature, and acceleration.

One potential limitation of this approach is the possibility of hysteresis and stress relaxation, which might alter the calibration over time. The elastomer used here (Sylgard 184) is a viscoelastic material and exhibits properties such as creep and stress relaxation [40,41]. It is expected that in certain applications of the FXTH87 sensor package, an indenter may be holding the coated capacitive transducer membrane in a compressed state for extended periods of time. When held in compression at a specific strain value, the load and signal value are expected to decrease slightly over time, due to stress relaxation of the PDMS elastomer. The experiments presented in this study were performed immediately after the elastomer had cured. In future experiments, the sensors should be preconditioned, which would allow the elastomer to undergo compression set prior to calibration, therefore, reducing the effect of stress relaxation and drift of the signal value over extended periods of compression. This phenomenon does not influence the outcome of this study; however, it may alter the profile of the calibration curve. Depending on the application, the sensor package could be exposed to large amounts of cyclic loading. While the tests performed in this study demonstrate small hysteresis in the short term, a long-term hysteresis experiment should be performed to quantify the FXTH87 signal difference between the loading and unloading cycles. The mixture ratio for the two components of the elastomer used in this study was based on the Dow Chemical Company published guidelines for Sylgard 184 preparation [38]. It is expected that the mechanical properties of the Sylgard 184 could be altered by changing the mixture ratio of the base and curing agents. Altering the viscoelastic properties of the transduction medium could further minimize stress relaxation and hysteresis. Alternatively, another type of elastomer could have been used to achieve similar functionality to the Sylgard 184. It was beyond the scope of this study to evaluate alternative elastomers and Sylgard 184 compositions. While other options could be explored, the performance of the Sylgard 184 was sufficient for the intended future application.

The target application of the FXTH87 wireless telemetric load and deformation sensor is orthopaedic implants that are too small to accommodate conventional strain-gauge sensing packages. The results of this study show that a repurposed tire-pressure sensor may be feasible for use in orthopaedic applications, as it is capable of monitoring small-scale deformation that can be calibrated into load measurements, has minimal power consumption, and can effectively transmit through tissue. Depending on the accompanying spring body, the sensor could be used in regenerative medicine and tissue engineering applications [42]. For example, the proposed package could potentially be embedded within fracture fixation plates to monitor the load and strain acting on the plate during patient rehabilitation. This information could be used to predict failure of the fixation plate and monitoring the plate strain over time should quantify the process of bone union. In addition, in the future it may be possible to connect supporting sensors to unused analog-to-digital converters on the FXTH87 to monitor physiological variables such as pH, oxygen tension, and other biomarkers [42]. Current mechanisms of measuring load in fracture fixation plates depend on sensors monitoring the change in surface strain on the implant. It may be possible to convert this flexure force into a compressive force, which would allow the proposed sensor to be embedded within a fixation plate to record load data. The proposed sensor inherently measures a vertical force; however, it is possible to embed the sensor in custom enclosures that transduce flexure, tension, and torque into compressive forces. In addition, the vertical mechanism of load measurement is well-suited for implants that are naturally under compression. For example, the sensor could also be embedded within intervertebral spinal-fusion cages to monitor in-vivo spinal loads and the bone healing process following spinal-fusion surgery. Another example application could be the measurement of loads inside a high-tibial osteotomy implant following surgery. The FXTH87 sensor package could also replace the sensor packages currently used to measure loads in larger components, such as knee implants. The information that could be obtained from these instrumented implants could improve future implant design and assist physicians in guiding patient rehabilitation practices. Knowledge of the forces acting on implants could also allow patients to identify at risk activities and self-monitor their recovery process. While the proposed sensor package is a key feature of a telemetric implant, there are several other factors that must be taken into consideration to ensure that the package is successful. For instance, the package must be sealed in a hermetic enclosure to prevent harm to the patient. The RF signal from the device must be capable of passing through said hermetic enclosure to an external receiver. Finally, the device, power source, and supporting implant must adhere to regulatory guidelines before being safely implanted in a patient. Outside of orthopaedic applications, this sensor package has the capability of being utilized for many load and strain sensing applications due to its size and functionality. These applications include, but are not limited to, in-vivo pressure measurements, activity tracking, infection monitoring (via temperature), and benchtop research experiments using cadaveric specimens. In the current enclosure configuration, the sensor package was designed to measure compressive deformation and loads; however, this sensor could also be embedded within custom structural enclosures that are designed to transduce tension, flexion, and torque.

2.5 Acknowledgements

This work was supported in part by the Canadian Institute of Health Research (Foundation Program) under Grant FDN-148474, the Ontario Research Fund (Research Excellence) under Grant RE-07-666, and The Collaborative Training Program in

Musculoskeletal Health Research at Western University. D. W. Holdsworth is supported as the Dr. Sandy Kirkley Chair in Musculoskeletal Research at Western University.

2.6 References

1. D'Lima, D., Fregly, B.J., and Colwell, C.W., "Implantable sensor technology: measuring bone and joint biomechanics of daily life in vivo," *Arthritis Res. Ther.*, vol. 15, no. 203, 2013, doi:10.1186/ar4138.

2. O'Connor, C. and Kiourti, A., "Wireless sensors for smart orthopedic implants," *J. Bio- Tribo-Corrosion*, vol. 3, no. 1127, 2017, doi:10.1007/s40735-017-0078-z.

3. Westerhoff, P., Graichen, F., Bender, A., Rohlmann, A., and Bergmann, G., "An instrumented implant for in vivo measurement of contact forces and contact moments in the shoulder joint," *Med. Eng. Phys.*, vol. 31, pp. 207–213, 2009, doi:10.1016/j.medengphy.2008.07.011.

4. Bergmann, G., Graichen, F., Siraky, J., Jendrzynski, H., and Rohlmann, A., "Multichannel strain gauge telemetry for orthopaedic implants," *J. Biomech.*, vol. 21, pp. 169–176, 1988, doi:10.1016/0021-9290(88)90009-7.

5. Graichen, F. and Bergmann, G., "Four-channel telemetry system for in vivo measurement of hip joint forces," *J. Biomed. Eng.*, vol. 13, pp. 370–374, 1991, doi:10.1016/0141-5425(91)90016-z.

6. Damm, P., Graichen, F., Rohlmann, A., Bender, A., and Bergmann, G., "Total hip joint prosthesis for in vivo measurement of forces and moments," *Med. Eng. Phys.*, vol. 32, pp. 95–100, 2010, doi:10.1016/j.medengphy.2009.10.003.

7. Graichen, F., Bergmann, G., and Rohlmann, A., "Hip endoprosthesis for in vivo measurement of joint force and temperature," *J. Biomech.*, vol. 32, pp. 1113–1117, 1999, doi:10.1016/s0021-9290(99)00110-4.

8. Davy, D.T., Kotzar, G.M., Brown, R.H., Heiple, K.G., Goldberg, V.M., Heiple, K.G., Jr., and Berilla, J., Burstein, A.H., "Telemetric across measurements total the hip after arthroplasty," *J. Bone Jt. Surg.*, vol. 70, pp. 45–50, 1998.

9. Kotzar, G.M., Davy, D.T., Goldberg, V.M., Heiple, K.G., Berilla, J., Brown, R.H., Burstein, A.H., and Heiple, K.G., Jr., "Telemeterized in vivo hip joint force data: a report on two patients after total hip surgery," *J. Orthop. Res.*, vol. 9, pp. 621–633, 1991, doi:10.1002/jor.1100090502.

10. Ruther, C., Timm, U., Fritsche, A., Ewald, H., Mittelmeier, W., Bader, R., and Kluess, D., "A new approach for diagnostic investigation of total hip replacement loosening," In *Biomedical Engineering Systems and Technologies*; Springer: Berlin/Heidelberg, Germany, pp. 74–79, 2013.

11. D'Lima, D.D., Townsend, C.P., Arms, S.W., Morris, B.A., and Colwell, C.W., "An implantable telemetry device to measure intra-articular tibial forces," *J. Biomech.*, vol. 38, pp. 299–304, 2005, doi:10.1016/j.jbiomech.2004.02.011.

12. Heinlein, B., Graichen, F., Bender, A., Rohlmann, A., and Bergmann, G., “Design, calibration and pre-clinical testing of an instrumented tibial tray,” *J. Biomech.*, vol 40, pp. S4–S10, 2007, doi:10.1016/j.jbiomech.2007.02.014.

13. Morris, B.A., D’limaD.D., Slamin, J., Kovacevic, N., Arms, S.W., Townsend, C.P., and Colwell, C.W., “e-Knee: evolution of the electronic knee prosthesis - telemetry technology development,” *J. Bone Jt. Surg.-Am.*, vol. 83a, pp. 62–66, 2001, doi:10.2106/00004623-200100021-00013. (In English)

14. Kaufman, K.R., Kovacevic, N., Irby, S.E., and Colwell, C.W., “Instrumented implant for measuring tibiofemoral forces,” *J. Biomech.*, vol. *29*, pp. 667–671, 1996, doi:10.1016/0021-9290(95)00124-7.

15. Crescini, D., Sardini, E., and Serpelloni, M., “Design and test of an autonomous sensor for force measurements in human knee implants,” *Sens. Actuators A Phys.*, vol. 166, pp. 1–8, 2011, doi:10.1016/j.sna.2010.12.010.

16. Almouahed, S., Gouriou, M., Hamitouche, C., Stindel, E., and Roux, C., “Design and evaluation of instrumented smart knee implant,” *IEEE Trans. Biomed. Eng.*, vol. 58, pp. 971–982, 2010, doi:10.1109/tbme.2010.2058806.

17. Grasa, J., Gomez-Benito, M.J., González-Torres, L., Asiaín, D., Quero, F., and García-Aznar, J.M., “Monitoring in vivo load transmission through an external fixator,” *Ann. Biomed. Eng.*, vol. 38, pp. 605–612, 2010, doi:10.1007/s10439-009-9889-5.

18. Claes, L. and Cunningham, J.L., “Monitoring the mechanical properties of healing bone,” *Clin. Orthop. Relat. Res.*, vol. 467, pp. 1964–1971, 2009, doi:10.1007/s11999-009-0752-7.

19. Rohlmann, A., Gabel, U., Graichen, F., Bender, A., and Bergmann, G., “An instrumented implant for vertebral body replacement that measures loads in the anterior spinal column,” *Med. Eng. Phys.*, vol. 29, pp. 580–585, 2007, doi:10.1016/j.medengphy.2006.06.012.

20. Rohlmann, A., Graichen, F., Weber, U., and Bergmann, G., “Monitoring in vivo implant loads with a telemeterized internal spinal fixation device,” *Spine*, vol. 25, pp. 2981–2986, 2000, doi:10.1097/00007632-200012010-00004.

21. Wilson, D.J., Morgan, R.L., Hesselden, K.L., Dodd, J.R., Janna, S.W., and Fagan, M.J., “A single-channel telemetric intramedullary nail for in vivo measurement of fracture healing,” *J. Orthop. Trauma*, vol. 23, pp. 702–709, 2009, doi:10.1097/bot.0b013e3181b01c49.

22. Greve, D., Oppenheim, I., and Chen, A., “An instrumented intramedullary implant to monitor strain in fracture healing,” In Proceedings of the 2012 IEEE International Ultrasonics Symposium, Dresden, Germany, pp. 1220–1223, 7–10 Oct. 2012 doi:10.1109/ultsym.2012.0304.

23. Borchani, W., Aono, K., Lajnef, N., and Chakrabartty, S., “Monitoring of postoperative bone healing using smart trauma-fixation device with integrated self-powered piezo-floating-gate sensors,” *IEEE Trans. Biomed. Eng.*, vol. 63, pp. 1463–1472, 2016, doi:10.1109/tbme.2015.2496237.

24. McGilvray, K.C., Unal, E., Troyer, K.L., Santoni, B.G., Palmer, R.H., Easley, J.T., Demir, H.V., and Puttlitz, C.M., “Implantable microelectromechanical sensors for diagnostic monitoring and post-surgical prediction of bone fracture healing,” *J. Orthop. Res.*, vol. 33, pp. 1439–1446, 2015, doi:10.1002/jor.22918.

25. Tan, Y., Hu, J., Ren, L., Zhu, J., Yang, J., and Liu, D., “A passive and wireless sensor for bone plate strain monitoring,” *Sensors*, vol. 17, no. 2635, 2017, doi:10.3390/s17112635.

26. Seide, K., AlJudaibi, M., Weinrich, N., Kowald, B., Jürgens, C., Müller, J., and Faschingbauer, M., “Telemetric assessment of bone healing with an instrumented internal fixator,” *J. Bone Jt. Surgery. Br. Vol.*, vol. 94, pp. 398–404, 2012, doi:10.1302/0301-620x.94b3.27550.

27. Melik, R., Perkgoz, N.K., Unal, E., Puttlitz, C., and Demir, H.V., “Bio-implantable passive on-chip RF-MEMS strain sensing resonators for orthopaedic applications,” *J. Micromech. Microeng.*, vol. 18, pp. 115017, 2008, doi:10.1088/0960-1317/18/11/115017.

28. Anderson, W.D., Wilson, S.L.M., Holdsworth, D.W., “Development of a wireless telemetry sensor device to measure load and deformation in orthopaedic applications,” *Sensors*, vol. 20, no. 23, pp. 6772, 2020, doi:10.3390/s20236772

29. Graichen, F., Arnold, R., Rohlmann, A., and Bergmann, G., “Implantable 9-channel telemetry system for in vivo load measurements with orthopedic implants,” *IEEE Trans. Biomed. Eng.*, vol. 54, pp. 253–261, 2007, doi:10.1109/tbme.2006.886857.

30. Platt, S.R., Farritor, S., Garvin, K., and Haider, H., “The use of piezoelectric ceramics for electric power generation within orthopedic implants,” *IEEE/ASME Trans. Mechatron.*, vol. 10, pp. 455–461, 2005, doi:10.1109/tmech.2005.852482.

31. A Hannan, M., Mutashar, S., A Samad, S., and Hussain, A., “Energy harvesting for the implantable biomedical devices: issues and challenges,” *Biomed. Eng. Online*, vol. 13, no. 79, 2014, doi:10.1186/1475-925x-13-79.

32. Cochran, G.V.B., Kadaba, M.P., and Palmieri, V.R., “External ultrasound can generate microampere direct currents in vivo from implanted piezoelectric materials,” *J. Orthop. Res.*, vol. 6, pp. 145–147, 1988, doi:10.1002/jor.1100060119.

33. Niell, E. and Elvin, A., “Implantable bone strain telemetry sensing system and method,” U.S. Patent 6,034,296, 7 Mar. 2000.

34. NXP Semiconductors. *FXTH870xD, Tire Pressure Monitor Sensor*; FXTH870xD Datasheet, rev. 1.6; NXP Semiconductors: Eindhoven, The Netherlands, February 2019.

35. NXP Semiconductors. *Compact Integrated Antennas*; AN2731, Revised September 2015; NXP Semiconductors: Eindhoven, The Netherlands, 2005.

36. NXP Semiconductors. *Assembly Guidelines for QFN (Quad Flat No-Lead) and SON (Small Outline No-Lead) Packages*; AN1902, Revised February 2018; NXP Semiconductors: Eindhoven, The Netherlands, Sept. 2008.

37. Johnston, I.D., McCluskey, D.K., Tan, C.K.L., and Tracey, M.C., "Mechanical characterization of bulk Sylgard 184 for microfluidics and microengineering," *J. Micromech. Microeng.*, vol. 24, 2014, doi:10.1088/0960-1317/24/3/035017.

38. The Dow Chemical Company. *SYLGARDTM 184 Silicone Elastomer*; 11-3184; The Dow Chemical Company: Midland, MI, USA, 2017.

39. Carroll, J.D., Long, K., Deibler, L., and Ford, K., "Mechanical behavior and damage mechanisms of encapsulant-filled elastomers," In Proceedings of the SEM 2015 Annual Conference and Exposition on Experimental and Applied Mechanics, Costa Mesa, USA, 8-11 Jun. 2015.

40. Schneider, F., Fellner, T., Wilde, J., and Wallrabe, U., "Mechanical properties of silicones for MEMS," *J. Micromech. Microeng.*, vol. 18, 2008, doi:10.1088/0960-1317/18/6/065008.

41. Findley, W.N., Lai, J.S., and Onaran, K., "*Creep and Relaxation of Nonlinear Viscoelastic Materials*," Dover Publications: New York, NY, USA, 1976.

42. Klosterhoff, B.S., Tsang, M., She, D., Ong, K.G., Allen, M.G., Willett, N.J., and Guldberg, R.E., "Implantable sensors for regenerative medicine," *J. Biomech. Eng.*, vol. 139, pp. 021009–02100911, 2017, doi:10.1115/1.4035436.

Chapter 3

3 Mechanical Analysis of 3D-Printed, High-Capacity Miniature Wireless Load Cells

3.1 Introduction

Development of high-capacity, 3D-printed, miniature wireless load cells have long been a challenge as there was a need for a small sensor package capable of monitoring load with a sophisticated telemetry and power management system [1]. The modifications to the commercially available FXTH87 tire pressure sensor described in Chapter 2 have enabled the development of miniature wireless load cells. Wireless sensor packages can be tasked to measure load and deformation in both remote and small-scale applications. Depending on the design of the deformable spring body that accompanies the sensor package, the novel load cells can be configured to monitor forces in applications ranging from orthopaedic components to industrial and commercial measurement applications. Many of these future applications would require the load cell to be functional for millions of cycles. Due to the wide range of potential applications, the load cells must have an adjustable load capacity to ensure they are able to meet the needs of the application. While many load cells with varying load capacity and prolonged fatigue life are commercially available today, almost all of them rely on a wired cable for data transfer and power. As a result, these packages are too large to be feasible in most small-scale measurement applications. There is a clear need for miniature, high-capacity deformable spring bodies with varying load capacity that can accommodate the instrumentation of the novel FXTH87 load sensor. In addition, the load cell spring body must have a sufficient fatigue life for long-term testing applications.

As modifying miniature capacitive pressure transducers to measure deformation and load is a recent achievement (described in Chapter 2), work has not been published describing the development of possible spring bodies that could accompany said sensors. To develop these structures, metal and plastic 3D-printing is a promising manufacturing method that can be used to quickly fabricate components of complex geometry. Custom structures can be designed to be deformable with different load capacities, based on material selection,

A modified version of this chapter is in preparation for submission to *Fatigue & Fracture of Engineering Materials & Structures*.

all while accommodating the placement of a miniature sensor package. While work describing the creation of custom deformable spring bodies for miniature capacitive transducers has not been previously presented, much work has been published that describes fatigue performance of 3D-printed Ti-6Al-4V, comparisons between numerical and experimental fatigue analysis, and development of small-scale load sensors that utilize capacitive methods to measure load. In addition, an analysis of different commercially available load cells with varying spring body mechanisms can be performed to determine which method is best for the FXTH87 load sensor. All of this previously published material can be used to validate the tests performed in this chapter, the results of said tests, and justify why the spring body design proposed in this chapter was selected.

Much work has been done by others to develop small-scale capacitive based load cells [2-7]. The described load sensors are all accompanied by a custom deformable spring body. While each individual sensor and spring body form a successful load cell, each package is limited by their proposed sensor. The described packages are all much larger than the FXTH87 sensor package. In addition, the load cells are not wireless and making them wireless would further increase their overall size, as additional components would have to be added. In [2], a silicone load cell with capacitive sensing elements was described. The silicone load cell is capable of measuring load of up to 1000 kg, which is impressive for a load cell with a spring body not fabricated using metal. The size of their actual capacitive sensing element is comparable to the size of the FXTH87 package. However, this package is wired and requires additional components for signal processing. While it is difficult to determine the overall size of their complete load cell, it appears that the FXTH87 and accompanying spring body would be significantly smaller in size and would have wireless transmission capabilities. In [3], a miniature multi-axis capacitive force-torque sensor was developed for biomechanical applications. They utilize a capacitive transducer with comb electrodes to monitor fingertip forces of up to 60 N. The size of the sensor and spring body components is approximately 1 cm^2 with a thickness of only a couple hundred microns. This is comparable to the size of the FXTH87 sensor package. However, this system has a reduced load capacity and requires a wired cable for data acquisition and power. If this package was altered to have functionality comparable to the FXTH87, many components would have to be added which would greatly increase the size of the device. In [4-7], four different miniature capacitive load cells were described. Each capacitive load sensor (parallel plate or comb electrode) was adhered to a thin wafer made of silicon. These load sensors are capable of monitoring forces of hundreds of Newtons. Each described sensor package is larger than the FXTH87 sensor package and lacks functionalities such as integrated signal processing and wireless transmission. Similar to the previously described devices, to alter these packages to make them perform comparable to the FXTH87, the size of each package would significantly increase. In all of these papers the fatigue life of their load cells is not presented; however, as most of the capacitive load cells are instrumented on spring bodies fabricated in flexible silicon structures it is expected that they would be capable of lasting for millions of cycles. While previously described load cells may have a fatigue life longer than the FXTH87 embedded in a 3D-printed deformable spring body, the superior small-size and functionality of the FXTH87 makes it advantageous in many applications.

As was described in the introduction to this thesis, much work has been done to quantify the fatigue performance of 3D-printed Ti-6Al-4V [8-11]. The conclusions of these papers indicate that the fatigue life of 3D-printed titanium alloy may be significantly less than wrought titanium alloy. This is because the fatigue performance of additively manufactured components is highly influenced by porosity, residual stress, build orientation, and surface roughness. This was true for parts 3D-printed using selective laser melting, electron beam melting, and laser engineered net shaping. In [8], the fatigue performance of SLM 3D-printed titanium alloy was analyzed as a function of build orientation and surface condition. In this study, the 3D-printed specimens were not subjected to heat treatment. They found that regardless of surface condition or build orientation, the fatigue life of 3D-printed titanium alloy was significantly less than the performance of wrought titanium alloy [8]. In [9], the fatigue performance of Ti-6Al-4V additively manufactured using laser engineered net shaping was determined to be less than wrought Ti-6Al-4V. In [10] and [11], Ti-6Al-4V components additively manufactured using electron beam melting had a fatigue life less than that of wrought Ti-6Al-4V. As the fatigue performance of 3D-printed Ti-6Al-4V is expected to be less than wrought titanium alloy, it is important that the design of the deformable spring body is optimized for a long fatigue life. One method to help optimize the design of the deformable spring body is to determine the theoretical fatigue life of the component. Theoretical fatigue analysis in software such as Fe-Safe (Dassault Systèmes, Vélizy-Villacoublay, France) has been shown to predict the experimental fatigue life of specimens with a high degree of accuracy [12]. This has only been shown to be accurate in materials with an extensive database of mechanical properties. As fatigue analysis of 3D-printed Ti-6Al-4V is an emerging area of study, there are currently no published studies that are capable of predicting the experimental fatigue performance of 3D-printed Ti-6Al-4V using fatigue analysis software. The work described in this chapter observes the difference between theoretical and experimental fatigue life of 3D-printed Ti-6Al-4V. Quantifying the difference between theoretical and experimental fatigue life of the proposed deformable spring body can help optimize the design of future iterations of the spring body and determine if the design promotes a lengthy fatigue life.

With the development of the successful miniature wireless load sensor described in Chapter 2, accompanying spring bodies can be designed to generate a family of loads cells with varying load capacities. To determine which spring body design is best for the described sensor, an analysis of commercially available load cell spring bodies can be performed. In Section 1.4.1 of this thesis, multiple different spring body designs were introduced. Beam, S-type, and button spring bodies are the most commonly used spring bodies available today. Beam-type load cells feature a series of strain gauges adhered to the surface of a metal beam. When load is applied to the beam, the beam deforms, and the resulting deflection is monitored by the strain gauges. To generate load cells of varying capacity, the dimensions of the metal beam are typically held constant, but varying amounts of material is removed from the beam interior. Similar to beam-type load cells, S-type load cells typically feature strain gauges adhered to a metallic deformable structure arranged in the shape of an “S”. Finally, a button load cell is a small and compact circular load cell that is commonly equipped with internal strain gauges and is best at measuring compression. For the sensor described in Chapter 2, a modified button load cell is preferable as it is compact and is effective at monitoring axial forces. S-type load cells could accompany the FXTH87 load cell, but the size of the package would greatly exceed the size of a button load cell. Beam-type load cells are not the best natural fit as other designs are better at measuring axial compression. Similar to S-type load cells, the size of beam-type load cells would have to increase to house the FXTH87. While a modified button load cell may be the best overall design shape for the FXTH87, aspects from each different spring body design can be implemented into the custom spring body. The spring elements of the button load cell can be converted to cantilever beams, deformable structures with known deflection and stress equations that can be easily customized to deform under varying load capacity. This proposed beam-button hybrid load cell design is deformable, compact, easily adjustable, and can accommodate the placement of the proposed FXTH87 load sensor.

This chapter quantifies the performance of the proposed miniature wireless load cell spring body using both theoretical and experimental mechanical testing. The full range of load cell capacity was quantified for multiple design iterations of the spring body, using finite element analysis and compression testing. A relationship was reported between increasing cantilever beam dimensions and increasing load capacity of the spring body. One of the spring bodies that was 3D-printed in Ti-6Al-4V was calibrated with the proposed FXTH87 sensor package to measure additional sensor performance variables that were not quantified in Chapter 2. These variables included creep, dead load output return, and repeatability performance of the load cell device. The results of the tests are compared to the performance targets proposed in Section 1.5 to determine whether or not this capacitive load cell is comparable to previously described devices. Theoretical and experimental fatigue analysis was performed on structures of increasing load capacity to determine the fatigue life of spring bodies fabricated using plastic and metal 3D printing. The device described in this thesis is an effective, unique instrument capable of measuring a wide variety of load values and may be feasible for use in many biomedical, industrial, and commercial applications.

3.2 Methods

3.2.1 Load Cell Spring Body Design

The two-component rectangular deformable spring body discussed in the introduction was modelled using 3D design software called SolidWorks (Dassault Systèmes, Vélizy-

Villacoublay, France). As was described in Chapter 2, the spring body features four rectangular cantilever beams that deform when a compressive force is applied to the lid component. The design features a hard stop to prevent excessive deformation of the cantilever beams and lid component to ensure that no damage is done to the sensor package embedded within the base component. To test how changing the dimensions of the cantilever beams affects the load capacity of the spring body, multiple iterations of the spring body were developed. In subsequent designs of the spring body the width of the cantilever beams was increased from 2 mm to 4 mm at 0.5 mm increments. From the deflection equations of rectangular cantilever beams (Equation 3.1), increasing beam width would theoretically increase the force required to cause full compression of the spring body. Other variables such as height and length of the beams were held constant.

Once a general spring body design was determined, a step-by-step process was developed to predict the load capacity of the enclosures. The first step to determine the load capacity of the spring body was to use the mechanical equations for the deformation of cantilever beams. Using these equations, the dimensions of the cantilever beams can be estimated. The equation for the deflection of a cantilever beam with a single load at the end (Equation 3.1) is a function of the applied load (F), the length of the beam (L), the modulus of elasticity of the material used to fabricate the beam (E), and the moment of inertia (I) [13].

Equation 3.1: Equation for deflection of a cantilever beam with an end load.

$$\delta_{max} = \frac{FL^3}{3EI}$$

The equation for the moment of inertia for a solid rectangular cross section (Equation 3.2) is a function of the width of the beam (b), and the height of the beam (h) [13].

Equation 3.2: Equation for moment of inertia of a rectangular cross section.

$$I = \frac{bh^3}{12}$$

As there is a limit to the amount of deformation that can be applied to the sensor package, the maximum deflection of the beam is a known value. The deflection equation can be rearranged to solve for force or applied load. While dimensions of the cantilever beam were not constrained during the initial phase of design, predictive dimensions could be made. For example, for the sensor board to be able to fit within the enclosure of cantilever beams, the length of the beams had to be long enough to create an internal area of sufficient size. If the deformation and force being applied to the cantilever beam were known the deflection equation could be rearranged to solve for the proper length, width, or height of the beam. As length and height are both cubed, changing these variables has a greater impact on the force required to cause deformation of the beams than the width.

Once dimension values were set to satisfy adequate deformation under a specific force, the maximum stress levels at varying points throughout the beam can be calculated. The stress value can be compared against the published value for the yield strength of the material used in beam fabrication to ensure that maximum deformation of the beam does not result in plastic irreparable damage. In addition, this can also be early predictor of improved fatigue life if the maximum stress is well below the yield strength of the material. The equation for maximum stress at the maximum moment (fixed end of the beam) (Equation 3.3) is a function of the distance to a point from the neutral axis (y_{max}), the force applied (F), the length of the beam (L), and the moment of inertia (I) [13].

Equation 3.3: Equation for maximum stress in at the fixed end of a cantilever beam.

$$\sigma_{max} = \frac{y_{max} F L}{I}$$

While this simple stress calculation may not be the best way to determine the stresses throughout the beam, it is a fast check of the design that can be completed before the 3D model is tested in finite element analysis (FEA) software.

3.2.2 3D Printing of Spring Bodies

To demonstrate the effect material properties have on the load capacity of the spring body, the five different spring bodies were fabricated in both PLA and titanium alloy (Ti-

6Al-4V). Plastic and metal 3D printing was used to rapidly generate a series of these custom structures. Plastic 3D printing was performed using a Dremel 3D45 printer, which utilizes FDM to generate the structures. Using the 3D model of the spring body in SolidWorks, a stereolithographic (STL) file was generated. The STL file was then imported into slicing software called Simplify3D (Simplify3D, Cincinnati, OH, USA). This software generates supports for the part, separates the part into layers for the 3D printer to build, and allows the user to adjust printing parameters such as infill %, nozzle temperature, and filament feed rate. A printing instruction file (gcode) was exported from Simplify3D and imported into the Dremel 3D45 to initiate the build. All plastic parts were 3D printed using white Dremel PLA filament with a 1.75 mm diameter. Spring bodies were also 3D printed in titanium alloy (Figure 3.1) at ADEISS (Additive Design in Surgical Solutions Centre, London, Canada), an ISO 13485 compliant facility that provides advanced medical and dental 3D printing solutions. At ADEISS, parts were fabricated using an AM400 printer (Renishaw plc, Wotton-under-Edge, United Kingdom) that utilizes SLM to build the structures. Post fabrication, the metal components were subjected to grit blasting and a custom heat treatment process derived by ADEISS to relieve the built-up thermal stresses from printing. The specific heat treatment process for the structures involved subjecting the parts to an incrementally increasing temperature environment in an argon gas chamber. The chamber was heated to 350 °C and held at this temperature for 30 minutes. The temperature was then raised to 850 °C and held for 60 minutes. After the hour, the chamber was naturally cooled, and the parts were removed when it was physically safe to do so (below 100 °C). Both plastic and metal 3D printed parts were made with specified nominal 100% infill to reduce the chance that there might be internal porosity in the cantilever beams.

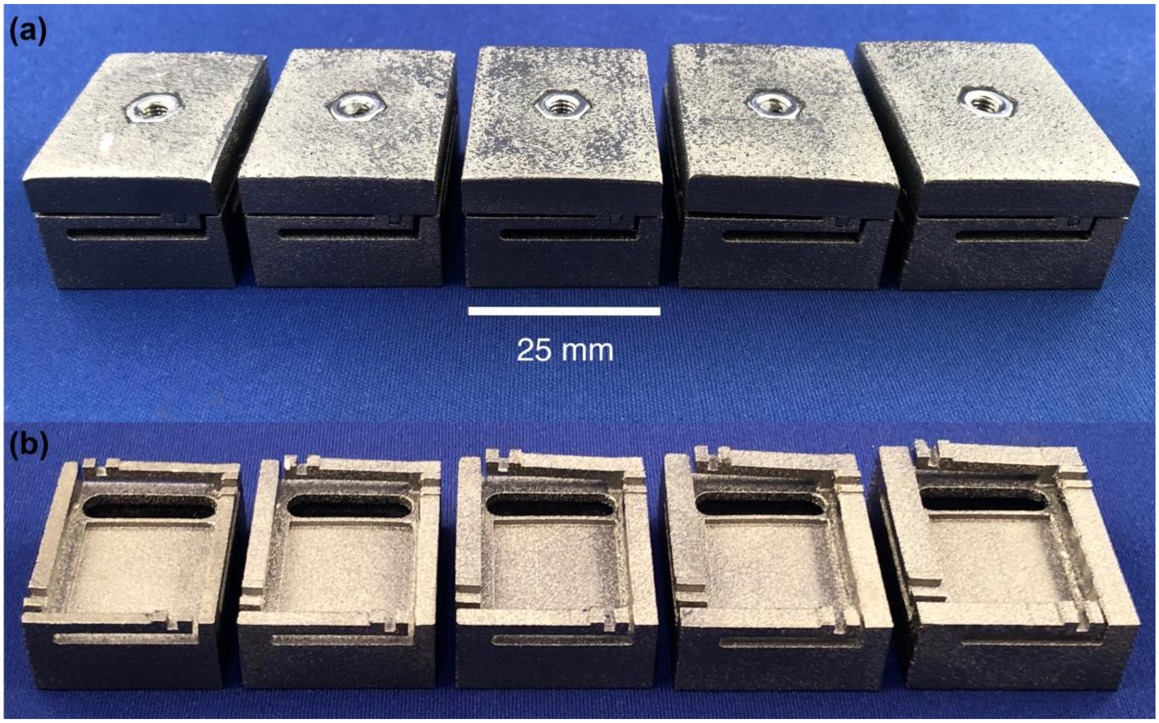

Figure 3.1: Five size iterations of the spring body 3D-printed in Ti-6Al-4V. (a) Spring body comprised of lid and base components. (b) Lid component removed, base exposed.

During the fabrication process of the Ti-6Al-4V spring bodies, a small defect was produced on each size iteration of the spring body. This defect was likely caused by residual thermal stresses in the 3D printing process. Residual stresses are created due to temperature gradients in the structure from the surface to the core [14]. The material inside the structure cools slower than the material on the surface of the part, which induces stress [15]. Common indications that residual stresses influenced part structure include warping and cracks. Eliminating residual stresses can be challenging in complex parts, such as our proposed spring bodies, as the structures need to be oriented in certain positions to be built without major defects. The defect observed in our parts was a slight warping of one of the smaller cantilever beams. The beam was slightly slanted upward above a level position and was not perfectly flat like the other three beams (Figure 3.2). In Figure 3.2, the yellow arrow indicates the location of the start of the defect. From the base to the tip, the beam slightly peels upward. This causes the unfixed end of the cantilever beam to higher than the fixed end. While the discrepancy in height is only about a millimeter, the defect influences the performance of both the single cantilever beam and the two-component structure as a whole. To fully deform the cantilever beam with the defect, the amount of deformation must be slightly increased. Therefore, it is likely that the stresses in that individual beam will be higher and will result in premature failure. While it may seem like this defect eliminates this structure from being effectively tested, due to the testing procedures described below this defect can be mitigated to still provide accurate results. For example, the defect may cause the specimen to fail due to fatigue much sooner than expected. However, due to experiment design, the performance of the remaining cantilever beams can be effectively evaluated. Full analysis of the defect and how it affected the experimental results is described in the discussion.

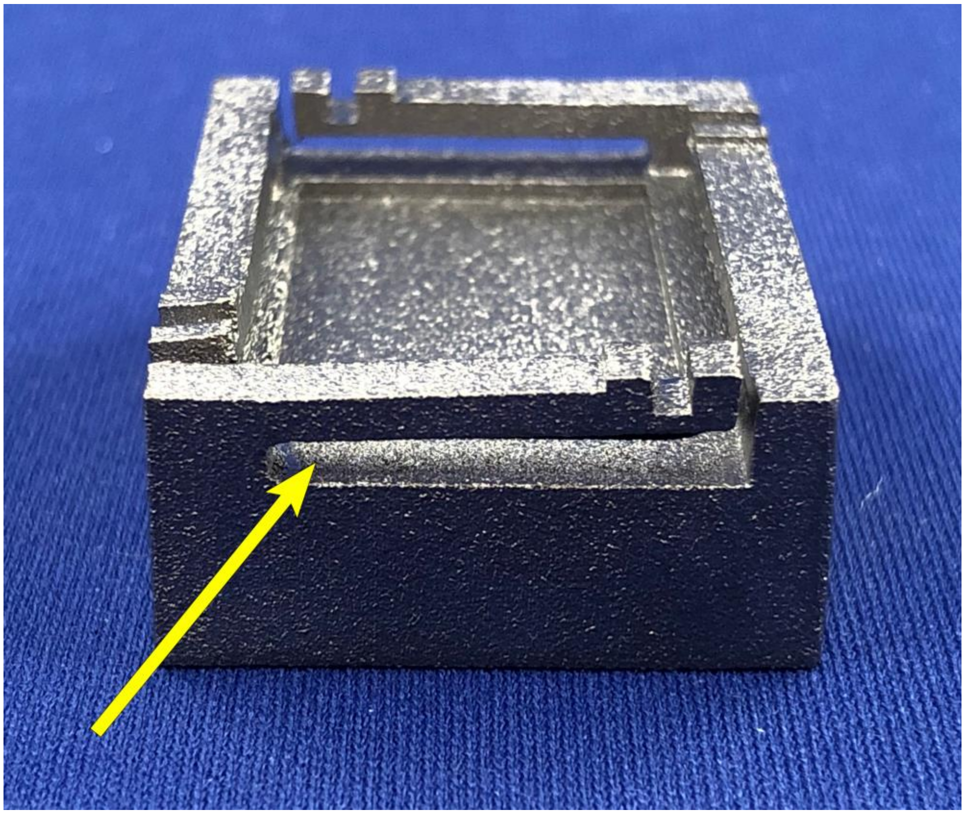

Figure 3.2: Location of the start of the defect on the fixed end of the shorter cantilever beams (arrow).

3.2.3 Load Cell Theoretical Mechanical Testing

To determine the theoretical performance of the spring body of the load cell the structure was modelled using finite element analysis software. The spring body was subjected to compression and cyclic compression testing to determine the load capacity of different load cell designs and their corresponding fatigue life.

3.2.3.1 Spring Body Compressive Deformation Analysis

To test the theoretical load capacity of the spring bodies, the 3D model of the two-component enclosure was imported into a finite element analysis software package (ABAQUS, Dassault Systèmes, Vélizy-Villacoublay, France). Theoretical spring body load capacity is defined as the force that is required to deform the cantilever beams and lid component until the lid reaches the built-in hard stop, the fixed end of the cantilever beams. In other words, the force required to compress the spring body by approximately 500 µm. Linear static analysis with quadratic tetrahedral elements (spaced every 0.25 mm) was used to model the spring bodies (Figure 3.3). All objects were defined to be 100% solid structures made with a homogenous material. Compression testing of the spring bodies was performed on the five size iterations in two different materials, PLA and Ti-6Al-4V. PLA was defined to have an elastic modulus of 3.5 GPa and a Poisson’s ratio of 0.36 [16]. Titanium alloy was defined to have an elastic modulus of 113.8 GPa and a Poisson’s ration of 0.342 [17]. Load was applied to the top surface of the lid component as a pressure force to ensure the load was evenly spread over the entire lid. The bottom surface of the base component holding the cantilever beams was held fixed to prevent movement. At the interaction between the lid and base component, surface-to-surface contact was modelled with an interaction property defined by penalty friction formulation with a coefficient of friction of 0.9. From the theoretical analysis, the load capacity and regions of maximum stresses can be determined.

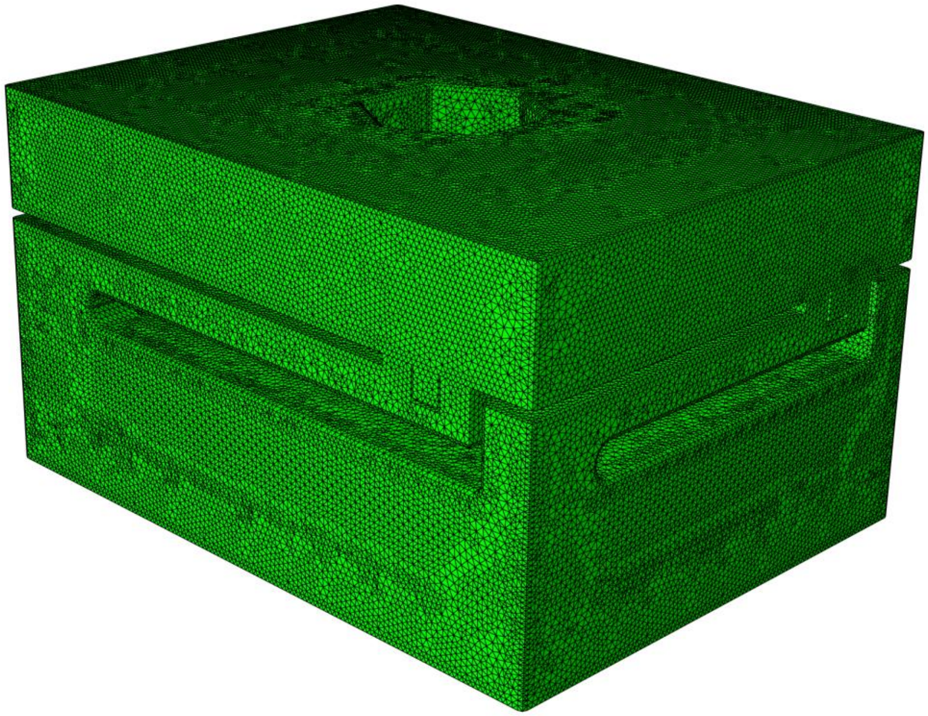

Figure 3.3: Mesh of the spring body in ABAQUS. Over 100,000 elements were typically required to model the test structures.

3.2.3.2 Spring Body Fatigue Analysis

To estimate the fatigue life of the spring bodies, the spring body finite element model was imported into fatigue analysis software called Fe-Safe. Fe-Safe can estimate the number of cycles until a structure fails due to fatigue. To do this, the software reads the finite element model from ABAQUS to evaluate the geometry of the structure being tested, the load being applied, and the regions of high stress values. It is expected that in most scenarios the object fails due to fatigue at a location very close to the location of maximum stress determined by ABAQUS [12]. In ABAQUS, an analysis can be performed on a structure when only the elastic modulus and Poisson’s ratio of a material are known. Fe-Safe is more complex in that the program requires a number of specific fatigue parameters for the selected material. In addition to elastic modulus and Poisson’s ratio, Fe-Safe requires additional variables such as the ultimate strength and yield strength of the material, as well as the fatigue strength, ductility, and cyclic strain hardening exponents and coefficients (Table 3.1). While the ultimate strength and yield strength of the material are reported within a standard material properties sheet, specific fatigue parameters of a material are not readily available. This is especially the case for 3D printed materials such as Ti-6Al-4V and PLA, as advanced fatigue testing needs to be performed to obtain these fatigue parameters empirically. However, Fe-Safe is able to approximate the fatigue parameters of an unknown material if the static material properties are known. This approximation technique, known as Seeger's method, uses the ultimate strength of the material to predict the unknown fatigue exponents and coefficients [18]. The fatigue parameters of 3D-printed Ti-6Al-4V and PLA used for analysis are presented in Table 3.2. Static material properties for titanium alloy and PLA were acquired from their respective material datasheets [16, 17].

Table 3.1: Fatigue parameters required by Fe-Safe for testing.

Symbol	Property	Units
E	Elastic Modulus	GPa
ν	Poisson's Ratio	Dimensionless
Su	Ultimate Strength	MPa
Sy	Yield Strength	MPa
b	Fatigue Strength Exponent	Dimensionless
σ'_f	Fatigue Strength Coefficient	MPa
c	Fatigue Ductility Exponent	Dimensionless
ε'_f	Fatigue Ductility Coefficient	Dimensionless
K'	Cyclic Strain Hardening Coefficient	Dimensionless
n'	Cyclic Strain Hardening Exponent	Dimensionless

Table 3.2: Fatigue parameters for Ti-6Al-4V and PLA required by Fe-Safe for testing.

Material	E	ν	Su	Sy	b	σ'_f	c	ε'_f	K'	n'
Ti-6Al-4V	113	0.34	950	880	-0.1	1586	-0.69	0.35	1833	0.14
PLA	3.5	0.36	73	70	-0.09	88.5	-0.58	0	97.35	0.15

Previous work describing the fatigue analysis of 3D-printed Ti-6Al-4V structures have presented similar values to the ones listed here [12]. As this is simply an approximation of the fatigue parameters of a material, it is likely that the true parameters of the material are slightly different. Previous work describing a sensitivity analysis of each fatigue parameter has indicated that slightly changing a parameter has little effect on the fatigue life, especially at lower number of cycles [19]. Until advanced fatigue material testing has been performed on 3D-printed Ti-6Al-4V and PLA, using Seeger's method to approximate fatigue parameters is the best method of obtaining the unknown values. While this method of fatigue analysis is simple, the popularity of 3D-printed materials has resulted in numerous studies emerging today that are attempting to model and predict the dynamic performance of 3D-printed metals. These studies are incorporating properties such as surface roughness and lack-of-fusion pores into their theoretical fatigue analysis [20, 21].

With the fatigue parameters for titanium alloy and PLA in hand, the ten ABAQUS models described in Section 3.2.3.1 were imported into Fe-Safe. Five size iterations of the spring body were tested in titanium alloy and PLA to determine their theoretical fatigue life. As was described, the spring bodies were compressed to their load capacities, or the load required to fully compress the spring body approximately 500 µm. Using each file from ABAQUS, Fe-Safe simulated a cyclic analysis of the proposed loading profile. Fe-Safe determines fatigue life by performing a strain-life analysis using the stresses and strains from the ABAQUS model and the material properties presented in Table 3.2. A detailed description of the process Fe-Safe uses to calculate fatigue life can be found in [18]. After the simulation is complete, Fe-Safe exports a file to ABAQUS that identifies the number of cycles until failure and the location on the object where crack initiation occurred.

3.2.4 Load Cell Experimental Mechanical Testing

To determine the experimental performance of the spring body and the load cell, the structure was subjected to different compressive deformation experiments. The spring body was subjected to compression and cyclic compression testing to determine the load capacity of different load cell designs and their corresponding fatigue life. The load cell, comprised of a metal spring body and embedded FXTH87 sensor, was tested to calibrate a metal spring body. In addition, the performance of the load cell was determined by subjecting the load cell to test procedures presented in the load cell regulatory requirements document R60 [22] described in Section 1.5.

3.2.4.1 Compressive Deformation Experiments

The spring body of the load cell was subjected to experimental compression and cyclic compression tests to determine the experimental load capacity of the enclosure and the fatigue life. To calibrate a metal load cell, an FXTH87 sensor was embedded within one of the metal spring bodies and subjected to multiple trials of compressive deformation.

Similar to the theoretical load capacity defined in Section 3.2.3.1, the experimental load capacity of the enclosure is defined as the load that is required to fully compress the lid of the enclosure until it reaches the hard stop. To determine the experimental load capacity of the spring bodies compressive deformation was applied to the five size iterations of the 3D printed titanium alloy and PLA spring bodies (Figure 3.4). Compressive deformation was applied to the top surface of the lid component of the enclosures using an Instron 3343 (Instron, Norwood, MA, USA). Compressive deformation was applied to the specimens at a rate of 500 µm/min. Compressive load was recorded using a 50 N load cell (Model 2519-102, Instron) for enclosures fabricated in PLA, a 1000 N load cell (Model 2519-105, Instron) for enclosures fabricated in titanium alloy, and the Instron Bluehill software (Instron). Compressive load and deformation were recorded at a rate of approximately 14 Hz.

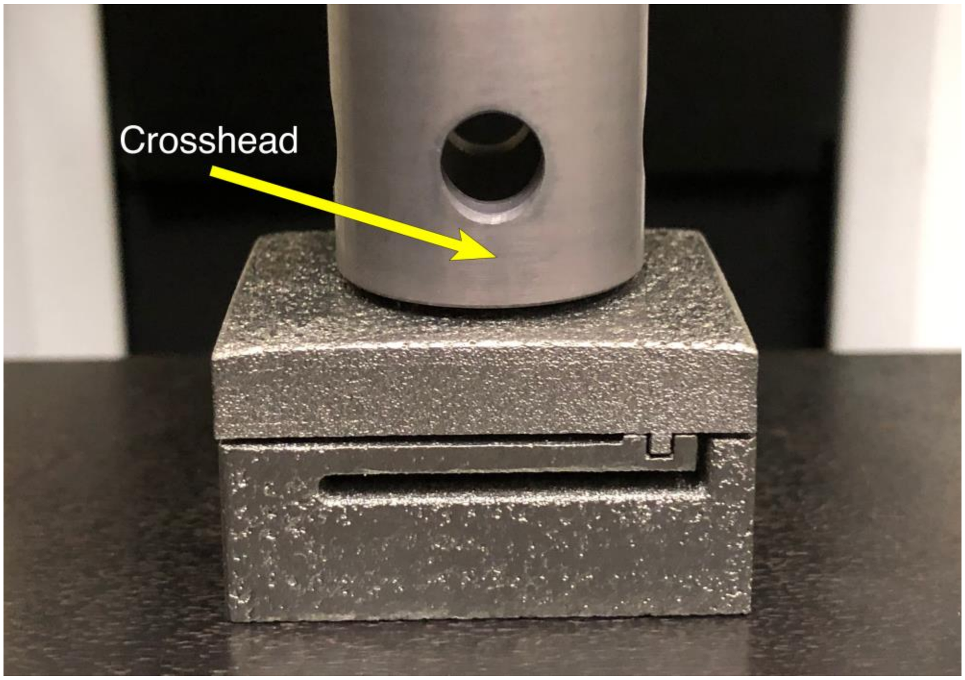

Figure 3.4: Instron 3343 testing apparatus during all compressive deformation experiments.

Experimental load capacity was determined by observing a sharp flexion point on the plot of compressive load vs. deformation as reported by the Instron in Bluehill. As deformation is applied to the spring body, the compressive load increases linearly. In the initial phase of the test, it is reasonable to say that deformation is relatively easy as there is open space for the lid and cantilever beams to deform to. As the lid component of the spring body reaches the hard stop there is no more room to deform. At this point, to further deform the load cell, it would require solid titanium alloy or PLA to deform; the force required to deform a solid block of titanium alloy or PLA is significantly greater than the force that is required to deform the cantilever beams. The change of phases from beam deformation to solid material deformation at the hard stop is easily observable on the load vs. deformation plot of the Instron. When small amounts of deformation are applied to the spring body in a hard stop position, the load required to cause said deformation increases rapidly. Therefore, the transition point on the load vs. deformation plot of the enclosure easily defines the experimental load capacity of the enclosure.

The test procedure to calibrate a metal load cell, comprised of a metal spring body and FXTH87 sensor, is similar to the PLA load cell calibration method described in Chapter 2. Calibration of the sensor package when it was embedded inside the metal spring body was performed by applying compressive deformation to the enclosure and measuring the change in signal value and compressive load. The sensor package was held firmly inside the enclosure with wires protruding out of the base to an external power source, a DC power supply. The set screw housed in the lid was adjusted to a position that just barely came into contact with the surface of the capacitive transducer. This ensured that any amount of compression of the enclosure would result in displacement of the top plate of the capacitive transducer and increase the output signal value. Ten trials of compressive deformation were applied to the enclosure using an Instron 3343.

To determine the experimental fatigue life of the metal and plastic spring bodies, the enclosures were subjected to cyclic compressive deformation. Cyclic compressive deformation was applied to the spring bodies using a commercial material testing device, the Instron ElectroPuls E10000 (Instron) (Figure 3.5). This machine is capable of applying compressive forces of up to 10 kN and can perform dynamic tests at 100 Hz. Compressive load was recorded using a 10 kN load cell (Model 2527-202, Instron) and the Instron Bluehill software.

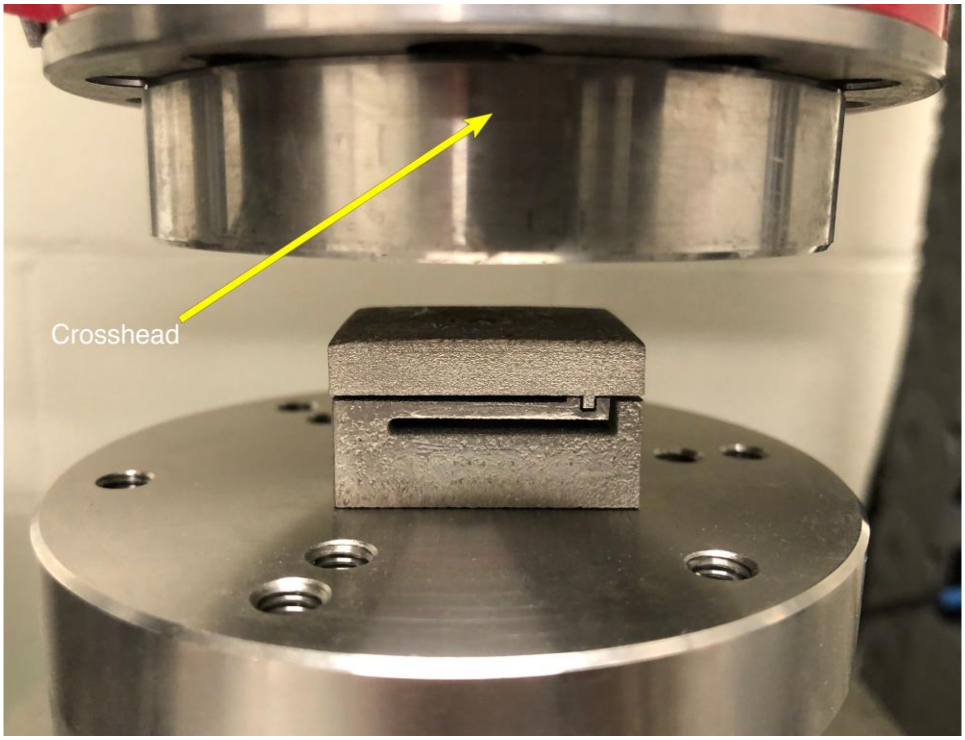

Figure 3.5: ElectroPuls E10000 apparatus during cyclic compression experiments (supporting fixation structure and clamps not included for visibility).

The spring bodies were sandwiched between two flat surfaced metal plates. The top plate, in contact with the flat lid component, was the bottom surface of the crosshead, the actuator applying deformation to the specimen. The bottom plate, in contact with the base of the spring body, was the top surface of the load cell used for testing. To ensure the spring bodies remained in a stable position during the test, a supporting alignment enclosure was clamped to the base plate on top of the load cell. All ten fatigue tests were run at 10 Hz at a stress ratio of R = 0.1 until specimen failure or runout (specified as 10^6 cycles). Stress ratio is defined as the ratio of minimum stress to maximum stress during a cycle. While the stress ratio is constant for each spring body, the physical force being applied to each enclosure is different depending on its load capacity. In other words, each of the plastic and metal enclosures were loaded to their individual maximum deformation capacity. As the design of each spring body is different, fully compressing each enclosure will result in a different maximum load value. The minimum force applied to the spring bodies was approximately 10% of the maximum load capacity. This ensured that the crosshead of the Instron was always in contact with the top surface of the lid component. The fatigue tests performed on the Instron were all operated by displacement control. Each specimen was slightly loaded to eliminate slack before each test commenced. The displacement of the crosshead was set to ensure the structure reached maximum compression. Displacement control was selected instead of load control so that no excessive damage was done to the spring bodies. When operating in displacement control, when the first cantilever arm of the specimen breaks the test can continue to run, albeit with a reduction in the load required to compress the spring body. If load control was used, when the first cantilever arm breaks, the Instron would adjust the applied displacement to ensure certain load thresholds were met; this could result in overloading of the specimen.

3.2.4.2 Testing of Calibrated Load Cell

Once the calibration of the load cell, comprised of the FXTH87 sensor and metal spring body, was completed, additional compression experiments were performed on the load cell to quantify its performance. Load cell test procedures were developed from document R60 outlined in Section 1.5 that present metrological regulations for strain-gauge based load cells [22]. As was previously described, to develop test procedures the maximum and minimum measuring range of the load cell needs to be determined. The metal spring body used during the calibration was the smallest size iteration of the metal enclosures. From compression testing, it was determined that the experimental load capacity of the load cell was approximately 160 N. The compressive displacement required to achieve this maximum value was approximately 500 µm. As was presented in Chapter 2, this displacement value exceeds the 350 µm displacement capacity of the sensor package. Therefore, the sensor and spring body were calibrated over the initial 350 µm of deformation of the spring body. The load required to deform the spring body 350 µm was approximately 120 N. This maximum value of 120 N sets the measuring range of the load cell, as the sensor is calibrated to measure loads from 0 N to 120 N. For the test procedures described below, approximately 0 N refers to the minimum load of the measuring range and 120 N refers to the maximum load of the measuring range. It is approximated that the minimum load of the measuring range is 0 N to simplify the test procedure. In reality, the smallest load the load cell can measure is actually a value slightly larger than 0 N, no matter how finely adjusted the set screw is in relation to the membrane of the capacitive transducer in the FXTH87. For example, placing a piece of paper on of the load cell will not generate a response from the sensor as the weight of the piece of paper is not large enough to cause any deformation of the cantilever beams. For the spring body used in testing, the force required to move the cantilever beams out of a position of rest is less than 0.5 Newton. With the measuring range established for the load cell, test procedures can be constructed.

Document R60 outlines a test to determine the repeatability error of the load sensor. To determine the repeatability error of the load cell three trials of compressive deformation were performed. The load cell was compressed to the maximum load of the measuring range of the sensor package, or in other words the upper most limit of the calibration. Using the three trials, repeatability error was determined by calculating the standard deviation as a percent of the mean at the maximum load value. As was described in Section 1.5, previously described load sensors tasked to measure orthopaedic loads had repeatability errors ranging from less than 1% to approximately 8% [23-25].

Document R60 outlines procedures to measure the creep error of a load cell. To determine the creep error of the calibrated load cell, the load cell was loaded to and held at its maximum capacity of 120 N and the output value was recorded over 30 minutes. In the load sensor proposed in this thesis, the load sensing mechanism is very different from previously described load sensors. By coupling a capacitive transducer with Sylgard 184, an elastomeric material with viscoelastic properties, the output sensor signal may be susceptible to drift, as the elastomeric medium will undergo stress relaxation when held in a constant position. As the elastomeric material is coupled to the capacitive transducer, this material relaxation will likely cause the output signal value from the sensor to quickly decrease over the first few minutes but will then stabilize and reach steady state. The output sensor signal value graph from the creep test is expected to closely resemble the stress relaxation plot of Sylgard 184 [26]. While it is not explicitly stated, from the work described in [26], the load required to deform Sylgard 184 decreased by approximately 5% over a period of two minutes. As the Sylgard 184 is coupled to the capacitive transducer, it is expected that during the creep test outlined by document R60 the output signal value from the sensor will decrease by at least 5%. Document R60 also provides the test procedure to measure dead load output return. Immediately before and after the 30-minute creep test, the minimum value of the load measuring range is recorded. As dead load output return is not a measure commonly reported in orthopaedic sensing applications, it is challenging to identify an optimal performance target. With that being said, it is advantageous for the dead load output return to be as close to 0 N as possible. This indicates that the sensor quickly rebounded following the 30-minute creep test and is ready to be used to record subsequent measurements.

3.2.5 Data Analysis

To determine if there was a relationship between theoretical and experimental load capacity of the plastic and metal spring bodies, the load capacity of each spring body was plotted against the increasing width of the cantilever beams. To observe the difference between theoretical and experimental fatigue life of plastic and metal spring bodies, a table was generated with the number of cycles to failure for each size iteration of the spring bodies. In addition, from ABAQUS, figures of stress distribution were provided to illustrate the regions of high stresses in the spring body during maximum compression. Using the output file from Fe-Safe, a figure depicting the theoretical location of structure failure was presented. A figure of the location of structure failure during experimental fatigue tested was included to compare theoretical and experimental failure locations.

Similar to the procedure described in Chapter 2, during the load cell calibration, to analyze the data, resampling was required to achieve a consistent number of data points between the recorded data from the Instron and the FXTH87 sensor package. A MATLAB script was created to import the data sets for each trial into MATLAB. The recorded data from the sensor package was resampled using the native MATLAB function, resample. The resulting sampling rate of the transducer matched the rate of the Instron. To develop a calibration curve for the load cell, ten compression trials were performed; compressive load from the Instron was plotted against output signal value from the FXTH87 sensor package. The data was fitted to a non-linear equation (Equation

3.4) generated by Prism, as was described in Chapter 2. To observe the creep response of the sensor, the output value from the load cell was plotted against time.

Equation 3.4: Non-linear equation that was fitted to the calibration data.

$$y(x) = A\,x/(B + x) + Cx + D$$

3.3 Results

3.3.1 Spring Body Compressive Testing

The theoretical and experimental compressive deformation experiments demonstrate that even a small change in the dimensions of the cantilever beam result in structures that require more load to fully deform (Figure 3.6, 3.7). As the width of the cantilever beams increased, so did the maximum load capacity of the spring bodies. Theoretical compression testing of the spring bodies served as a good indicator of experimental performance. On average, the load difference between the theoretical and experimental load capacities of the spring body were 0.54 N for PLA enclosures and 44 N for titanium alloy enclosures.

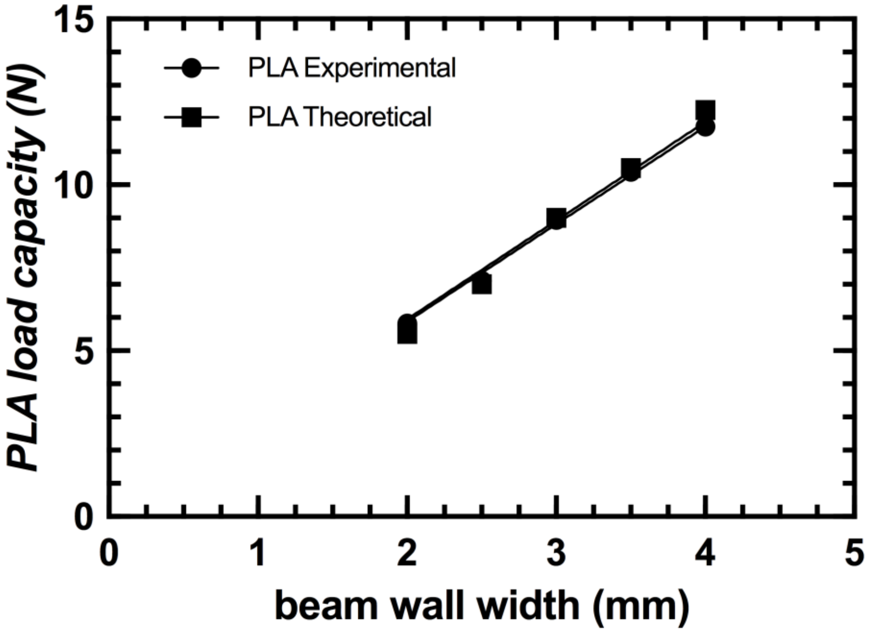

Figure 3.6: Theoretical and experimental PLA load capacity vs. cantilever beam wall width.

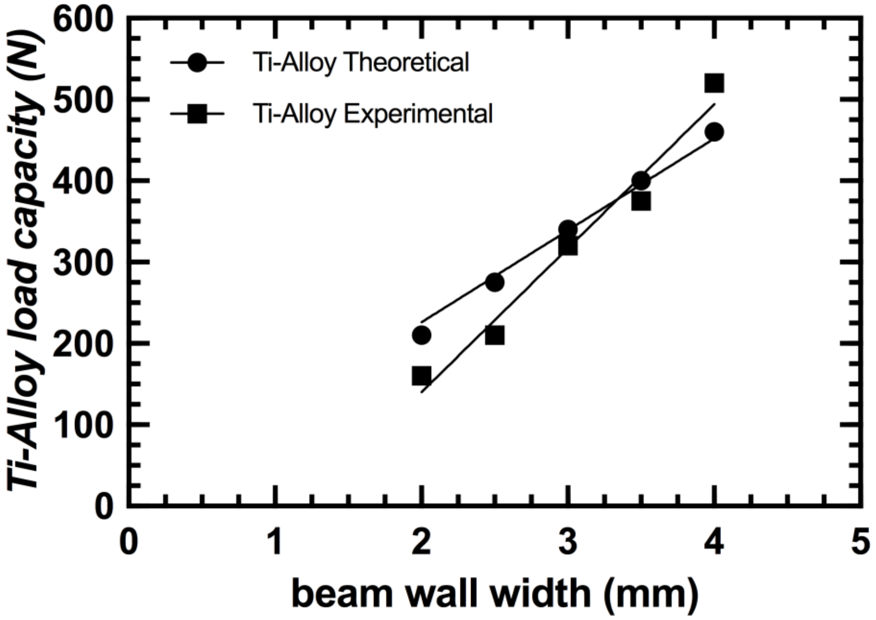

Figure 3.7: Theoretical and experimental Ti-6Al-4V load capacity vs. cantilever beam wall width.

The theoretical and experimental cyclic compression experiments demonstrate that fatigue modelling can be used as an effective tool to estimate the fatigue life of the load cells and can identify the location of failure. For structures modelled in PLA, the theoretical and experimental fatigue life was identical. Fe-Safe estimated that the PLA spring bodies would not fail under the load applied (Table 3.4). This was mirrored in the experimental tests as the PLA enclosures successfully completed 10^6 without any indication of failure. For structures modelled in Ti-6Al-4V, the theoretical fatigue life prediction was a good indicator of the experimental performance. The theoretical analysis of fatigue life predicted that the spring bodies would undergo more cycles than were observed during experimental testing (Table 3.3). As was described in the methods, there was a defect on one of the cantilever beams on each titanium spring body. First beam failure always occurred at the defect location. Due to the design of the test (cyclic compression using Instron displacement control), the rest of the beams could be evaluated. Therefore, the second beam break is the best indicator of fatigue life as it represents failure of an intact and undeformed cantilever beam. Full failure analysis is discussed in Section 3.4.

Table 3.3: Theoretical and experimental number of cycles to fatigue failure for spring bodies fabricated in Ti-6Al-4V. (*) indicates failure on cantilever beam with a defect.

Cycles to failure (Cycles)	Cantilever beam wall width (mm)				
	2 mm	2.5 mm	3 mm	3.5 mm	4 mm
1st Break	256,000*	94,000*	102,000*	51,000*	36,000*
2nd Break	736,000	310,000	250,000	162,000	122,000
Fe-Safe Prediction	804,000	401,000	306,000	170,000	277,000

Table 3.4: Theoretical and experimental number of cycles to fatigue failure for spring bodies fabricated in PLA.

Cycles to failure (Cycles)	Cantilever beam wall width (mm)				
	2 mm	2.5 mm	3 mm	3.5 mm	4 mm
1st Break	Runout	Runout	Runout	Runout	Runout
Fe-Safe Prediction	10^8	10^8	10^8	10^8	10^8

Fe-Safe was able to successfully predict the location of failure for the spring bodies 3D printed in titanium alloy. From the stress distribution pattern during the compressive deformation tests in ABAQUS, it is observed that high stresses in the spring body occur at the fixed end of the cantilever beams (Figure 3.8). More specifically, the regions of maximum stress concentration occur at the fixed ends of the two shorter cantilever beams. It is important to note that the average value of maximum stress observed at full compression of the titanium alloy spring bodies was approximately 880 MPa. This value is very similar to the published tensile and compressive yield stress values of 880 MPa and 970 MPa for Ti-6Al-4V [17]. In the output file from Fe-Safe, the predicted failure location (Figure 3.9) was observed to be in the same region as the point of maximum stress. From the experimental fatigue tests, the location of failure on the 3D printed structures (Figure 3.10) was observed to be in a similar spot to the location predicted by Fe-Safe.

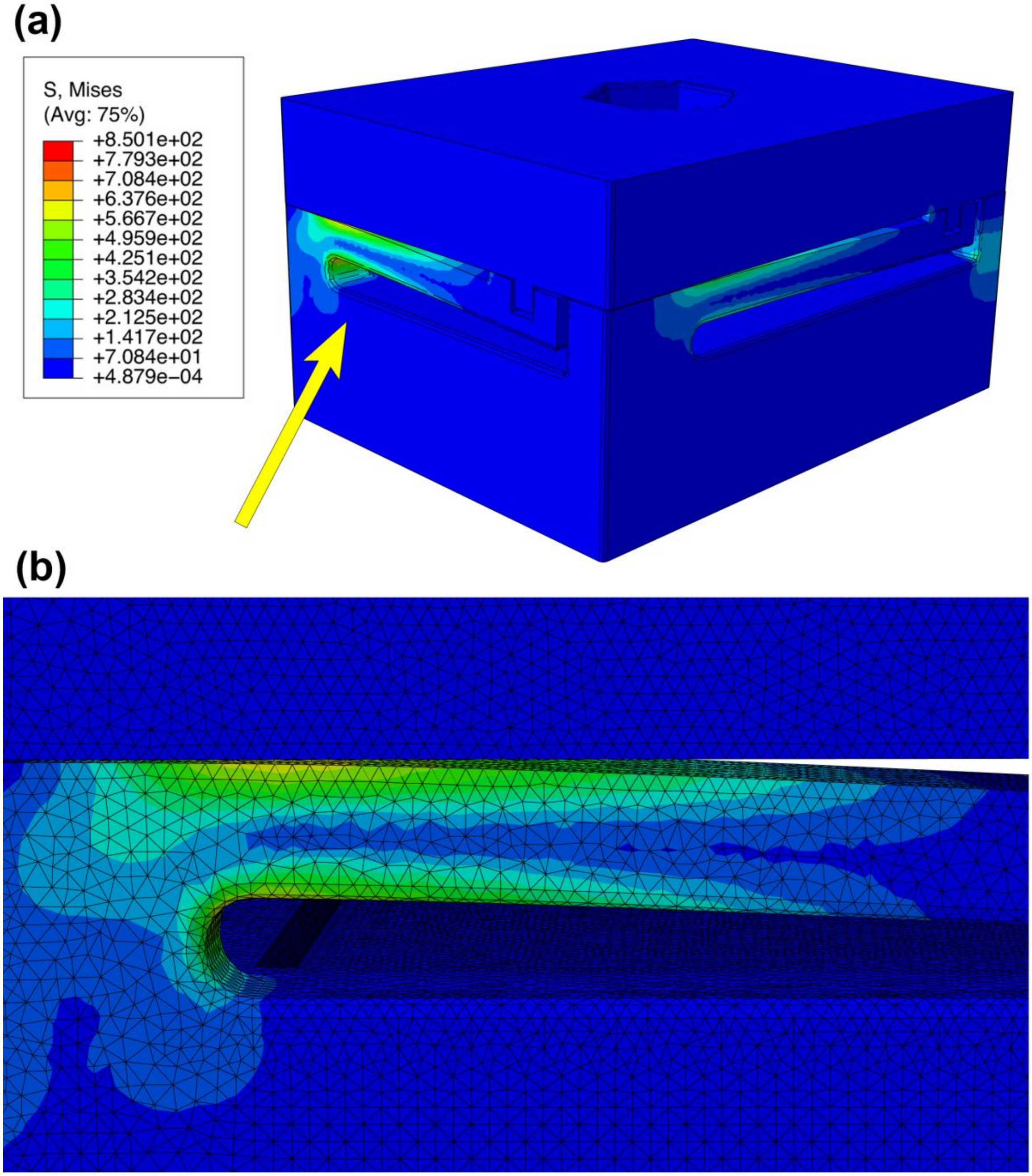

Figure 3.8: (a) Maximum stress location from ABAQUS during compression tests (arrow). (b) Close up view of location of maximum stress at fixed end of short cantilever beam.

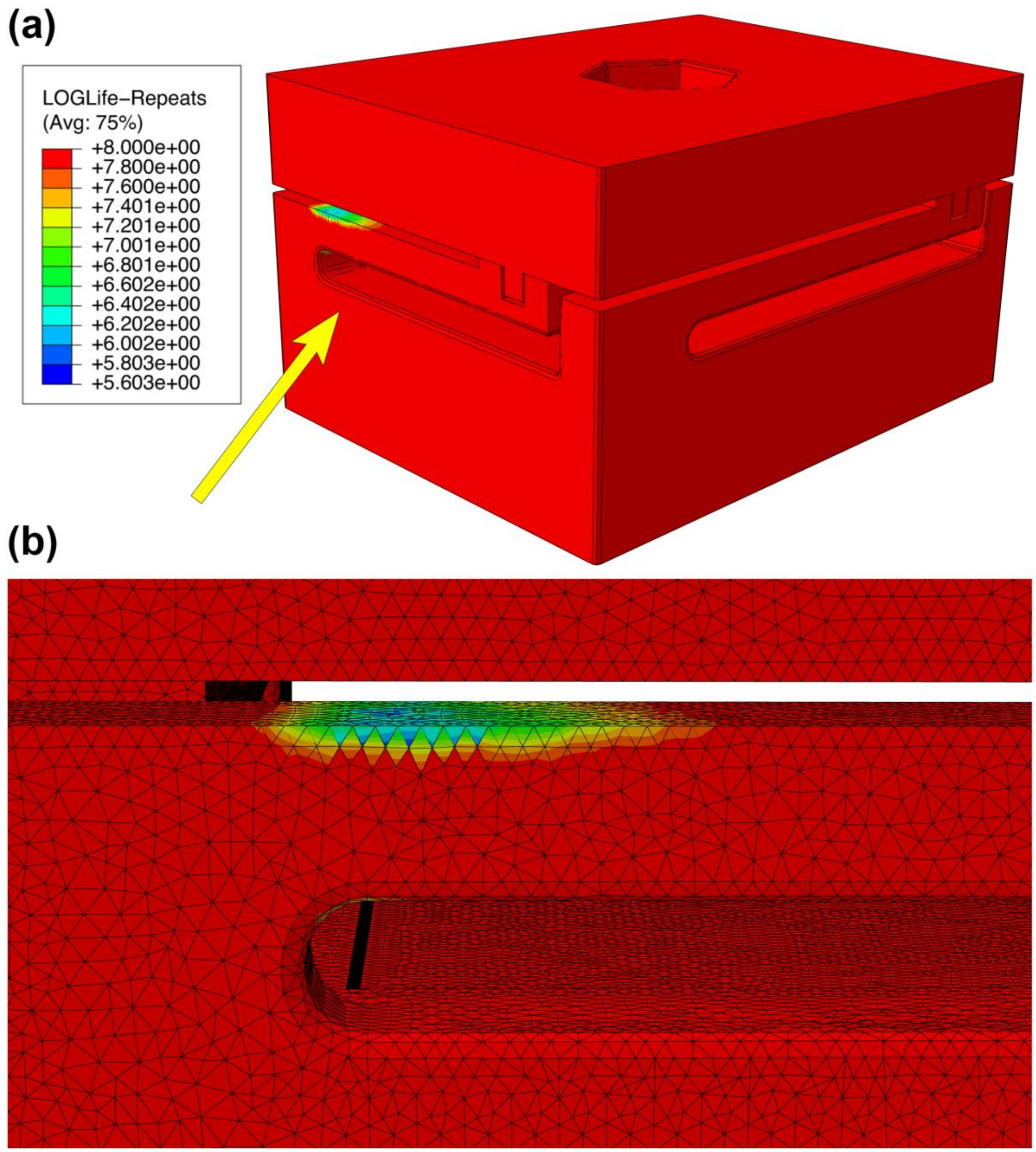

Figure 3.9: (a) Failure region predicted by Fe-Safe (arrow) in number of cycles. (b) Close up view of estimated failure location at fixed end of shorter cantilever beam.

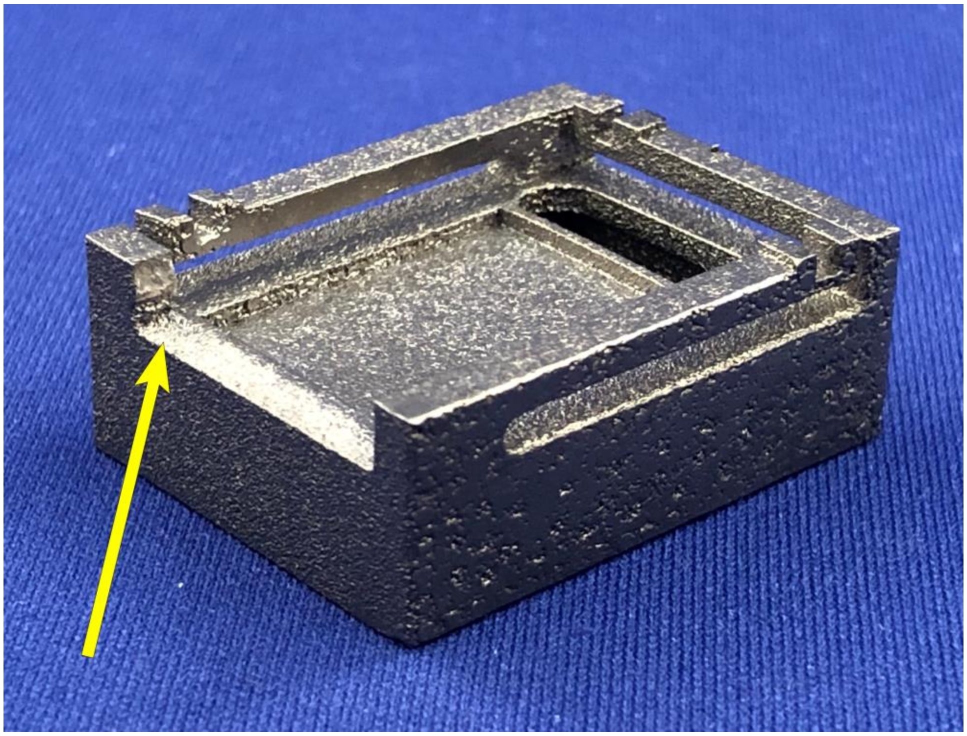

Figure 3.10: Failure location (1st break) during experimental fatigue testing (arrow). Failure in subsequent beams occurred in the same location near the fixed end of the cantilever beams.

3.3.2 Calibrated Load Cell Testing

During calibration, the titanium alloy load cell and sensor exhibited a positive relationship between compressive load and signal value with an R^2 value of 0.9992 (Figure 3.11). The average measuring error of the load sensor was approximately 2%. A compressive load of approximately 120 N was required to fully compress the enclosure and the capacitive transducer. The repeatability error between three different loading trials was less than 1%. This value is comparable to the repeatability error observed in the sensors previously described in Section 1.5.

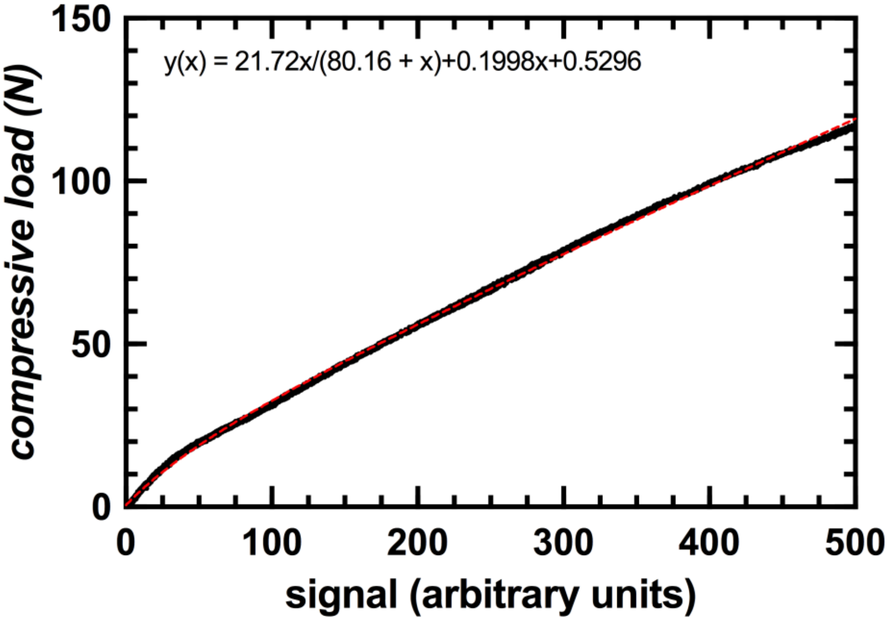

Figure 3.11: Calibration curve of 120 N metal spring body enclosure.

During the creep test, the output signal response of the sensor significantly decreased over the 30-minute time span of the test (Figure 3.12). After 20 minutes, the output value from the capacitive transducer dropped approximately 10.3 N. After 30 minutes, the output signal value changed approximately 10.7 N from the value recorded at the start of the test. The sensor output signal decreased by approximately 10%, which is greater than the expected load drop of approximately 5% that was observed in [26]. The change in dead load output return, which was measured immediately before and after the creep test, was observed to be 2.2 N.

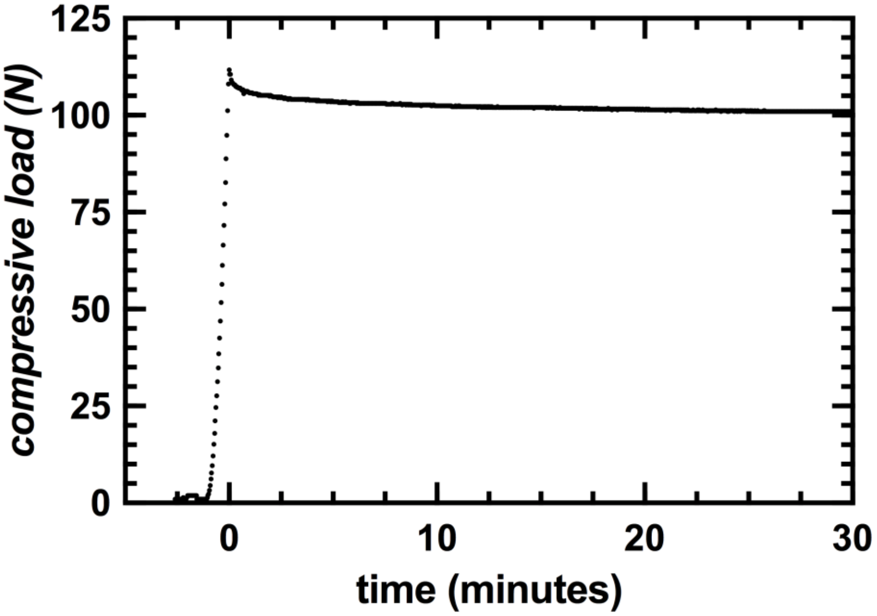

Figure 3.12: Compressive load from the FXTH87 sensor vs. time during 30-minute creep test on the Ti-6Al-4V load cell package.

3.4 Discussion

The results of this study have demonstrated that it is feasible to modify design parameters of a cantilever beam to achieve structures that require varying compressive forces to fully deform. The investigation shows that there is a relationship between theoretical and experimental load capacity in spring bodies 3D-printed in PLA and Ti-6Al-4V. The larger difference between Ti-6Al-4V theoretical and experimental load capacity is likely due to the defect present in one of the cantilever beams. A correlation between theoretical and experimental load capacity will allow spring bodies to be rapidly designed and fabricated for use in custom load measurement applications. In addition, the spring bodies can all easily accommodate the FXTH87 sensor and supporting PCB described in Chapter 2. The spring bodies can be designed to require a significant force to deform while only deforming a couple of hundred microns. This makes these spring bodies a perfect fit for the supporting FXTH87 sensor package as they deform the full capacity of the capacitive transducer of the sensor without damaging any components.

The correlation between theoretical and experimental performance of the spring bodies will significantly decrease the time from design to prototype. In this study, changing only one design parameter of the cantilever beam was analyzed. Changing the width of the cantilever beam by even half a millimeter was able to change the load capacity of the spring body. Width was selected as the parameter to be altered as this would still allow the overall size of the spring body to be quite small. However, if size is not a primary concern, then there are other variables that can be adjusted that could result in a significant load capacity change. The most obvious variable that can be changed is the material that is used to fabricate the spring body. A material can be selected based on the application of the spring body and load cell. For example, if the spring bodies were 3D-printed in cobalt chrome then the load capacity of the spring bodies would greatly increase as the modulus of elasticity of cobalt chrome (~210 GPa) is significantly higher than titanium alloy (114 GPa) [27]. In a scenario where small loads are being measured and a long fatigue life is desired, a thermoplastic material may be an ideal material candidate. Aside from material properties and cantilever beam width, the two most important variables that effect load capacity are the length and height of the cantilever beam. From the equation that describes deflection of a rectangular cantilever beam (Equation 3.1), it is evident that length and height are a significant determinate of the deformation capacity of the structure. In the equation, both length and height influence the deformation to the third power, whereas width has a linear effect. Therefore, a small change in the height or length of the cantilever beam can have significant impacts on the load capacity of the spring bodies. Based on their location in the equation, increasing the height and/or decreasing the length of the cantilever beam would increase the load capacity of the spring body. By altering the material used in fabrication and the dimensions of the cantilever beam there are many methods of changing the load capacity of the spring. However, by changing the dimensions of the cantilever beam, the overall size of the load cell may increase. In the future, these variables can be adjusted to develop structures with theoretical load capacities well over a thousand Newtons.

During fatigue testing, theoretical fatigue modelling was a good indicator of experimental fatigue life. The spring bodies fabricated in PLA did not fail due to fatigue, as predicted by the Fe-Safe model. If the fatigue failure caused by the cantilever beam defect (1st beam break) is ignored and the first failure of an intact cantilever beam (2nd beam break) is analyzed, the spring bodies fabricated in Ti-6Al-4V trended towards failing earlier than predicted by the fatigue model. This was to be expected for several reasons, the first being that the structure modelled in ABAQUS and Fe-Safe was a perfectly solid homogenous material with the properties of Ti-6Al-4V. It is reasonable to say that the structure modelled in ABQUS and Fe-Safe was representative of a spring body perfectly fabricated in pure wrought titanium alloy. As was described in Section 3.1, there have been a number of studies that show that the mechanical fatigue properties of 3D-printed Ti-6Al-4V are less than conventionally manufactured titanium alloy [8-11]. From this consideration alone it was expected that the 3D-printed spring bodies would fail before Fe-Safe predicted. Another contributing factor that resulted in early first failure of the metal 3D-printed spring bodies were the slight defects to the structure, which were caused during the fabrication process. As was described in the methods, in each of the five metal 3D-printed spring bodies, one of the four cantilever beams was slightly raised above a level position. While this defect was reduced in the smaller size iterations of the metal spring bodies, the larger enclosures suffered a greater defect. This defect was introduced during the 3D metal printing process, most likely due to residual thermal stress. For a complex structure like the spring bodies, the objects had to printed in an orientation that would not require any internal supports. It would be challenging to remove internal supports without compromising the integrity of the cantilever beams. Multiple fabrication iterations of the metal spring body were performed at ADEISS, a metal 3D printing facility, to try and find an orientation that reduced the defects as much as possible. In the future, if this general spring body design is selected, additional fabrication analysis needs to be performed to ensure the structures are printed exactly as modelled. With regards to the defects on the current spring bodies, the location of initial beam fatigue failure was always on the cantilever beam with the defect. This is because the cantilever beams with a defect had to undergo significantly more compressive deformation to reach full compression. Therefore, the stresses in the defective cantilever beam were likely much higher than predicted, which resulted in early failure. The inherent mechanical properties of 3D-printed titanium alloy and the small defects present in one of the cantilever beams are the main factors that lead to failure sooner than expected. In general, we found that the structures failed before the number of cycles predicted by the fatigue modelling software. This result is still promising even when failure was approximately 50,000 to 100,000 cycles before predicted failure. It validates what was described throughout this section; that the inherent mechanical properties of 3D-printed Ti-6Al-4V are influencing the fatigue life. By measuring the experimental fatigue life of these 3D-printed structures, it may be possible to tune the fatigue modelling process to achieve fatigue predictions comparable to experimental results. This would involve adjusting the mechanical material parameters required for fatigue modelling, which were presented in Section 3.2.3.2. Future work would involve developing a feedback loop where results of experimental fatigue tests would be used to tune fatigue parameters in the initial modelling phase. The work presented in this thesis is the first step towards developing a gold standard for accurate fatigue prediction modelling of 3D-printed Ti6Al-4V.

From the experimental fatigue testing it was observed that the location of failure on the cantilever beams was very similar to the location of failure predicted by Fe-Safe and the region of maximum stress predicted by ABAQUS. This argument still holds true even with the presence of the described defect on the one of the smaller cantilever beams. The location of second cantilever beam failure on the spring bodies was always at the base of the intact shorter cantilever beam. Due to the design of the fatigue test apparatus and method, the cyclic compression test continued as intended, even when one of the cantilever arms was broken. As the test was operated by displacement control, no additional load was applied to any of the remaining cantilever beams. With results that suggest that the failure location can be predicted before experimental testing, an analysis can be performed to determine alterations that can be made to the spring body in the early phase of design to decrease regions of high stress. Consequently, this will help to extend the fatigue life of the spring body. From the results, the location of highest stress and fatigue failure is at the fixed end of the shorter cantilever beams. This is expected because from Equation 3.1, the shorter the length of the cantilever beam, the more force is required to deform the unfixed end of the beam the same amount as the long beams. This larger required force increases the stresses in the shorter cantilever beam. A rectangular spring body was developed to generate the smallest possible enclosure that could accompany the FXTH87 sensor package. However, one of the best ways to decrease stress and increase the fatigue life of the load cell is to develop a spring body that is symmetrical. This spring body would likely be square or circular in shape. A symmetrical spring body would redistribute the forces evenly over each of the cantilever beams. Another strategy that could be used to decrease stress concentrations could be to eliminate sharp corners and edges at the fixed end of the cantilever beams. When a structure features a sudden change in cross section, such as a sharp corner or edge, high local stresses occur near the discontinuity [13]. Adding a fillet to the fixed end of the cantilever beam could redistribute some of the local stresses and decrease the maximum overall stress at these locations. From the work presented in Chapter 2, it is likely that the FXTH87 will have a maximum deformation capacity of less than 500 microns. Therefore, in a future design the maximum deformation capacity of the spring body can be reduced to match the capacity of the sensor. Less deformation of the cantilever beams would result in reduced maximum stress in the cantilever beams and would likely lead to a longer fatigue life. By slightly changing the design of the spring body, it may be possible to greatly extend the fatigue life of the enclosure.

In addition to design changes, there are a number of post processing techniques that can be applied to 3D-printed metal components to increase their respective fatigue lives. Post-processing techniques such as hot isostatic pressing (HIP) and shot peening are effective at improving fatigue life by reducing porosity and residual stresses [28-30]. In addition, decreasing surface roughness can increase the fatigue performance of 3D printed objects [31]. Methods of decreasing surface roughness include polishing, chemical etching, electrochemical polishing, shot peening, and laser-ablation [31]. Future tests on the metal 3D-printed load cells could involve fabricating several versions of each spring body design, applying different post-processing techniques to each component, then observing the fatigue life. This would identify what post-processing techniques are most effective at improving the fatigue life of the custom geometry of the spring body.

As for the fatigue life of the present iteration of the spring body, the structures printed in titanium alloy all failed before reaching one million cycles. In comparison, many commercially available strain gauge load cells are fatigue-rated for up to 10^8 cycles. The spring bodies in these commercial load cells are currently not fabricated using 3D printing, partly due to concerns about the inherent fatigue properties of 3D printed materials. One of the objectives of this thesis was to develop a load cell that could be rapidly developed using 3D printing. This saves time in the process from design to prototype and it allows many different versions of the spring body to be fabricated within a few hours. It is certainly possible that the spring bodies described in this thesis could be machined from materials similar to the ones used in current commercially available load cells. In future studies, a performance comparison between spring bodies fabricated using different techniques would help to optimize the load cell package. While the fatigue life of the present iteration of the spring is relatively short compared to many commercially available devices, it does not completely preclude the spring body from being used. One application where a miniature device with reduced fatigue life may still be feasible is in orthopaedic fixation components that are retrieved after a period of weeks. Loading cycles applied to the implant are likely in the range of hundreds of thousands of cycles to a few million, not hundreds of millions of cycles, which is what many commercial load cells are designed for. With that being said, if the spring body of the FXTH87 load cell was fabricated differently then it may have an increased fatigue life. The small overall size of the FXTH87 load cell and wireless telemetry capabilities make this device advantageous, in comparison to strain gauge load cells, in remote small-scale applications. As was described in Chapter 2 the smallest wireless telemetric strain gauge load cell packages used in orthopaedic applications are all significantly larger than the device described in this thesis. In addition, commercially available wireless resistive and capacitive load cells are significantly greater in size than the FXTH87 load cell, as they require additional space for signal processing and telemetry components.

The results of this study demonstrate that the FXTH87 sensor package could be calibrated when embedded within a deformable metal spring body. Similar to the spring body described in Chapter 2, the error of the load sensor is low, but may further be reduced by performing additional calibration trials. The fact that the FXTH87 can be calibrated in a metal enclosure provides additional evidence that the sensor can be calibrated in a deformable enclosure of any material so long as the maximum deformation of the spring body does not exceed the displacement capacity of the

FXTH87. Therefore, there is no limit to the amount of load that the sensor package can measure. In future studies, calibrating spring bodies with load capacities up to and over 1 kN can also be performed. It is expected that the modified FXTH87 sensor package will provide similar performance, regardless of the design of the surrounding spring body. As was previously described, by adjusting cantilever beam dimensions, it is possible to develop spring bodies of higher load capacities even in materials such as plastic with an inherently low elastic modulus. Plastic load cells that are capable of measuring loads of up to 1 kN or more can be designed by simply changing the design of the cantilever beams, as demonstrated in Figure 3.13. These spring bodies will all be compatible for use with the FXTH87 so long as they deform without damaging in the sensor.

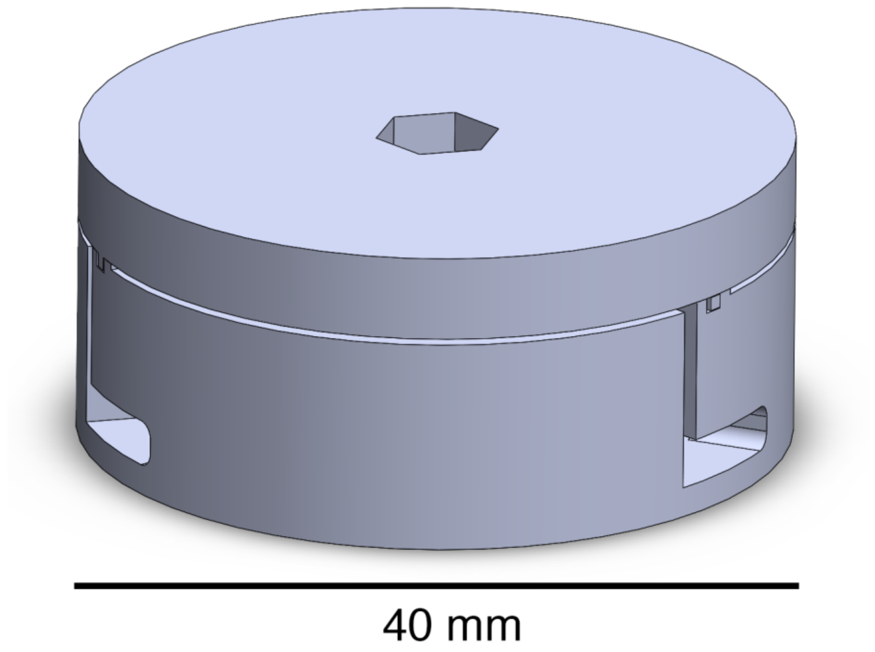

Figure 3.13: Concept for a plastic (PLA) 1 kN spring body in SolidWorks.

During compression trials of the calibrated load cell, it was found that the device was highly repeatable as there was only a small difference in the output signal values between trials. The repeatability error of the proposed sensor package would be acceptable in future orthopaedic applications as the amount of error between trials, less than 1%, indicates that the results of consecutive tests will be almost identical when using the same calibrated sensor. As was first reported in Chapter 2 and subsequently quantified again in this chapter, the average measuring error of the sensor package was approximately 2%. This is comparable to the previously described sensors discussed in Chapter 2 and well below the acceptable error limit proposed in Section 1.5.2. During the creep test on the load cell, the output signal value decreased continuously over a period of 30 minutes. The 10% decrease in load after 30 minutes was greater than the expected load decrease of 5% [26]. However, the test performed in [26] was significantly shorter than the test performed in this thesis (2 minutes instead of 30 minutes) so it is reasonable to assume that the percent load decrease could be similar. Finally, the change in dead load output return was approximately 2.2 N. This indicates that immediately following the creep test the Sylgard 184 may not have fully returned to its original position. This phenomenon can be mitigated by allowing the Sylgard 184 to rebound before commencing another test. In general, the load cell met nearly all of the performance targets for implantable load sensors proposed in Section 1.5.2. It was expected that the load cell developed in the thesis would be susceptible to creep due to the inherent behaviour of the Sylgard 184 applied to the capacitive pressure transducer. The drift observed in the signal value is not likely to be caused by the capacitive transducer of the FXTH87 because when the sensor is held at elevated pressure environments (e.g., within an automobile tire) the signal value does not change over time. If it did, then in the commercial application of the package, the tire-pressure measurement system would erroneously report a leak, as the pressure would appear to slowly decrease over time. The drift observed in the signal value during the creep test is more likely caused by the inherent stress relaxation response of viscoelastic materials [32]. When Sylgard 184 is held at constant strain, which is occurring during the test performed in this study, the stress value resulting from the onset of strain decreases over time. The response of the modified FXTH87 package is very similar to the published stress relaxation response of viscoelastic materials [32]. To ensure the load cell described in this thesis is feasible for use in applications where the package could be compressed for long periods of time, drift compensation has to be performed. While the response of the capacitive load cell did significantly drift over the first 5 minutes, from that point on the signal was fairly constant. This is an encouraging finding, because in some orthopaedic applications the load would be constant over long periods of time. If the signal continued to drop off to zero, then our sensor would not be feasible to record long-term static measurements. In this chapter, the signal response was only monitored for 30 minutes. Future tests of the sensor could involve monitoring the signal response over a period of days or weeks. If the sensor continues to perform as was observed in the time between 5 and 30 minutes during the creep test, it is reasonable to expect that sensor signal output would remain constant during this long-term test, further demonstrating that the sensor is capable of monitoring static loads. As was described in Chapter 2, during dynamic loading tests the sensor exhibited minimal hysteresis. The signal decrease observed during the static creep tests does not significantly influence the signal output during dynamic tests. This indicates that the sensor may perform better in dynamic applications such as fracture fixation and joint replacement.

In comparison to commercially available capacitive load cells, the FXTH87 and accompanying spring body are much smaller in overall size and have similar error values [33, 34]. All of the commercially available devices require wires for power and data collection. This reduces their feasibility in remote sensing applications. If commercial devices were to become wireless it would be expected that the overall size of the package would increase to include signal processing and transmission components. The performance of wired capacitive load cells is equal or better to the FXTH87 load cell in a number of tests. For example, commercial capacitive load cells do not experience the same signal drift that was observed in the FXTH87. Some packages can measure high load values with minimal deformation of the accompanying spring body. In certain devices the maximum deformation of the spring body is significantly smaller than the range of the FXTH87. In addition, the signal response of commercial capacitive load cells is linear, with low hysteresis and repeatability error. While the FXTH87 load cell may not perform to the same level as larger wired capacitive load cells, it is a significant achievement to demonstrate that a miniature wireless telemetric package is capable of measuring load and deformation with comparable error values. This indicates that the FXTH87 sensor package is feasible to use in numerous load and displacement monitoring applications, so long as it can be embedded within an appropriate deformable spring body.

In the future, additional experiments should be performed on the described load cell to further analyze its functionality. Document R60 that describes the metrological and technical requirements for load cells also requires that resistive load cells are subjected to loading in environments with changing temperature, humidity, and pressure [22]. These tests quantify how the output signal value from the load cell changes when operating in different environments. The benefit of using the FXTH87 is that the sensor was designed by NXP Semiconductors to operate in a very difficult environment. In its commercial application, the FXTH87 tire pressure sensor is able to withstand significant elevated pressure environments and almost any ambient temperature. The sensor operates during constant acceleration changes during driving and can withstand sharp impacts. As the natural operating environment of the FXTH87 is quite harsh, using the sensor in an orthopaedic application may actually be a much gentler environment. In biomedical applications, the temperature, pressure, and humidity would be tightly controlled. Therefore, adjustments, if any, could be made to the sensor package to prepare the device for specific environmental conditions. While it is expected that the sensor will successfully operate in various temperature, pressure, and humidity environments, verifying the performance of the sensor would further demonstrate that the device is feasible for biomedical applications. Without performing the tests, it is possible to estimate how the FXTH87 load cell would perform. As reported in the datasheet, the FXTH87 sensor is rated for use in temperatures ranging from −40 °C to 125 °C [35]. If the sensor is capable of operating over this large range it is likely the capacitive transducer would operate similar to how it performs at room temperature. However, it is unclear how the silicone elastomer applied to the surface of the capacitive transducer, Sylgard 184, will perform at temperature extremes. This test would be beneficial if the FXTH87 was to be tasked in commercial applications with either very high or low temperature conditions. In biomedical applications, the Sylgard 184 is expected to behave as was described in Chapter 2 as the in-vivo temperature environment is not much higher than room temperature and is well within the temperature capacity of the sensor. If the FXTH87 load cell was to be used in environments with increased humidity, modifications could be made to the package to prevent the system from failing. Encapsulating the PCB in an elastomer has been shown to protect electrical components from in-vivo environments [36-38]. Of the three environmental scenarios listed, testing the FXTH87 load cell in a pressurized environment may be the most interesting, as the capacitive transducer onboard the FXTH87 is a pressure sensor by design. While the external surface of the transducer has been modified with Sylgard 184, it is not clear if an increased pressure environment would alter load measurements. If a pressurized environment did affect the behaviour of the modified pressure sensor, then the FXTH87 load cell may only be rated for use in normal atmospheric conditions. Lastly, document R60 states under general requirements that load cells must be capable of performing their normal task when electrical disturbances are introduced [22]. Electrical disturbances are classified as power voltage variations, short-time power reductions, and surges. Due to the tightly controlled environment of orthopaedic components, the FXTH87 would not be exposed to these electrical disturbances. In general, the FXTH87 performs well during electrical disturbances such as power loss. For example, following loss of power during a battery change, the FXTH87 immediately resumes functionality. In addition to electrical disturbances, the document requires that the load cells are not susceptible to electromagnetic fields depending on the application of the device. The FXTH87 does have some level of inherent resistance to electromagnetic fields as it is able to function as intended in the presence of transmissions of varying frequency from foreign sources. It is important that the FXTH87 load cell can withstand disturbances so that the device can continue to operate as intended or does not fail completely. This is critical in orthopaedic applications where the load cell is embedded in a patient and cannot be easily accessed to replace or reprogram.

Building off the work described in Chapter 2, the results of the work presented in this chapter have culminated to a conclusion indicating that the proposed sensor package is feasible for use in biomedical applications as the sensor, in combination with a supporting spring body, have met the proposed performance targets for implantable load sensors described in Section 1.5.2. The modified FXTH87 sensor demonstrated multiple times that the measuring error was approximately 2%, which was comparable to previously described orthopaedic load sensors. The sensor provided a signal response that was highly repeatable, which allowed the sensor package to be effectively calibrated. From Chapter 2, the sensor error, load resistance, deformation capacity, hysteresis error, sensitivity, transmission range, and power consumption of the modified FXTH87 all met the proposed performance targets. In fact, in comparison to previously developed sensors, the FXTH87 performed better in areas such as power management. The work in Chapter 3 indicated that the sensor has no limit to the amount of load that it can measure, as the sensor can be embedded in deformable structures customized to measure different loads. This chapter demonstrated that fatigue modelling of the load cell spring bodies could be used as an effectively tool to predict the experimental performance of the structures. In the future, this work will help us to develop spring bodies to accompany the FXTH87 that have a sufficient fatigue life for their intended application. Finally, this chapter laid the groundwork for developing a fatigue model capable of accurately predicting the fatigue life of 3D-printed Ti-6Al-4V. To conclude, the modified FXTH87 and supporting spring bodies may be one of the smallest load cells of its kind that can meet our proposed performance targets and be feasible for use in biomedical applications.

3.5 Acknowledgements

The authors would like to thank Tom Chmiel from ADEISS for his help fabricating the metal spring body components tested during this Chapter and Todor Ivanov for his help performing compression and fatigue modelling in ABAQUS and Fe-Safe. This work was supported in part by the Canadian Institute of Health Research (Foundation Program) under Grant FDN-148474, the Ontario Research Fund (Research Excellence) under Grant RE-07-666, and The Collaborative Training Program in Musculoskeletal Health Research at Western University. D. W. Holdsworth is supported as the Dr. Sandy Kirkley Chair in Musculoskeletal Research at Western University.

3.6 References

1. D’Lima, D. D., Fregly, B. J., and Colwell, C. W., "Implantable sensor technology: measuring bone and joint biomechanics of daily life in vivo," *Arthritis Res. Ther.*, vol. 15, 2013, Art no. 203, doi: https://doi.org/10.1186/ar4138.

2. Wiegerink, R., Zwijze, R., Krijnen, G., Lammerink, T., and Elwenspoek, M., "Quasi-monolithic silicon load cell for loads up to 1000 kg with insensitivity to non-homogenous load distributions," *Sens. Actuators A Phys.*, vol. 80, no. 2, pp. 189-196, 10 Mar. 2000.

3. Brookhuis, R. A., Sanders, R. G. P., Ma, K., Lammerink, T. S. J., de Boer, M. J., Krijnen, G. J. M., and Wiegerink, R. J., "Miniature large range multi-axis force-torque sensor for biomechanical applications," *J. Micromech. Microeng.*, vol. 25, p. 025012, 22 Jan. 2015.

4. Sun, Y., Nelson, B. J., Potasek, D. P., and Enikov, E., "A bulk microfabricated multi-axis capacitive cellular force sensor using transverse comb drives," *J. Micromech. Microeng.*, vol. 12, pp. 832-840, 2002.

5. Mentink, M. J. A., Van Duren, B. H., Murray, D. W., and Gill, H. S., "A novel flexible capacitive load sensor for use in a mobile unicompartmental knee replacement bearing: an in vitro proof of concept study," *Med. Eng. Phys.*, vol. 46, pp. 44-53, 16 May 2017.

6. Saari, M., Xia, B., Cox, B., Krueger, P. S., Cohen, A. L., and Richer, E., "Fabrication and analysis of a composite 3d printed capacitive force sensor," *3D Print. Addit. Manuf.*, vol. 3, 3, pp. 137-141, 2016, doi: 10.1089/3dp.2016.0021.

7. Aebersold, J., Walsh, K., Crain, M., Martin, M., Voor, M., Lin, J., Jackson, D., Hnat, W., and Naber, J., "Design and development of a mems capacitive bending strain sensor," *J. Micromech. Microeng.*, vol. 16, pp. 935-942, 30 Mar. 2006.

8. Edwards, P. and Ramulu, M., "Fatigue performance evaluation of selective laser melted Ti-6Al-4V," *Mater. Sci. Eng. A Struct. Mater.*, vol. 598, pp. 327-337, 24 Jan. 2014.

9. Sterling, A., Shamsaei, N., Torries, B., and Thompson, S. M., "Fatigue behaviour of additively manufactured Ti-6Al-4V," *Procedia Engineering*, vol. 133, pp. 576-589, 2015.

10. Edwards, P., O’connor, A., and Ramulu, M., "Electron beam additive manufacturing of titanium components: properties and performance," *J. Manuf. Sci. Eng.*, vol. 135, no. 6, p. 061016, Dec. 2013.

11. Rafi, K. H., Karthik, N. V., Starr, T. L., and Stucker, B. E., "Mechanical property evaluation of Ti-6Al-4V parts made using electron beam melting," in *Solid*

Freeform Fabrication Symposium, SFF23, Laboratory for Freeform Fabrication at The University of Texas at Austin, 2012.

12. Duan, Y., Gonzalez, J. A., Kulkarni, P. A., Nagy, W. W., and Griggs, J. A., "Fatigue lifetime prediction of a reduced-diameter dental implant system: Numerical and experimental study," *Dent. Mater.*, vol. 34, pp. 1299-1309, 1 June 2018, doi: https://doi.org/10.1016/j.dental.2018.06.002.

13. Beer, F. P., Johnston, E. R., DeWolf, J. T., and Mazurek, D. F., *Mechanics of Materials*, Sixth ed. McGraw-Hill, 2012.

14. Sames, W. J., List, F. A., Pannala, S., Dehoff, R. R., and Babu, S. S., "The metallurgy and processing science of metal additive manufacturing," *Int. Mater. Rev.*, vol. 61, no. 5, pp. 315-360, 2016, doi: 10.1080/09506608.2015.1116649.

15. Li, C., Liu, Z. Y., Fang, X. Y., and Guo, Y. B., "Residual stress in metal additive manufacturing," *Procedia CIRP*, vol. 71, pp. 348-353, 2018, doi: https://doi.org/10.1016/j.procir.2018.05.039.

16. Farah, S., Anderson, D. G., and Langer, R., "Physical and mechanical properties of PLA, and their functions in widespread applications — A comprehensive review," *Adv. Drug Deliv. Rev.*, vol. 107, pp. 367-392, Dec. 2016, doi: http://dx.doi.org/10.1016/J.ADDR.2016.06.012.

17. "Titanium Ti-6Al-4V (Grade 5), Annealed." ASM Aerospace Specification Metals Inc. http://asm.matweb.com/search/SpecificMaterial.asp?bassnum=MTP641.

18. Safe Technology Ltd. *Fe-Safe User Manual Version 6.2*; Volume 2: Fatigue Theory Reference Manual, chapter 3, section 3.5, Safe Technology Ltd: Sheffield, UK, 31 Oct. 2002.

19. Chan, T. K., "A practical simulation methodology to improve fatigue life prediction of engine oil cooler undergoing pressure cycle testing," Master of Applied Science, McMaster University, 2013.

20. Dinh, T. D., Han, S., Yaghoubi, V., Xiang, H., Erdelyi, H., Craeghs, T., Segers, J., and Van Paepegem, W., "Modeling detrimental effects on high surface roughness on the fatigue behaviour of additively manufactured Ti-6Al-4V alloys," *Int. J. Fatigue*, vol. 144, p. 106034, 2021, doi: https://doi.org/10.1016/j.ijfatigue.2020.106034.

21. Le, V.-D., Pessard, E., Morel, F., and Prigent, S., "Fatigue behaviour of additively manufactured Ti-6Al-4V alloy: The role of defects on scatter and statistical size effect," *Int. J. Fatigue*, vol. 140, p. 105811, 2020, doi: https://doi.org/10.1016/j.ijfatigue.2020.105811.

22. International Organization of Legal Metrology. *Metrological Regulation for Load Cells*; Document R60, International Organization of Legal Metrology: Paris, France, 19 Nov. 2015. [Online]. Available: https://assets.publishing.service.gov.uk/government/uploads/system/uploads/attachment_data/file/484413/OIML_R60-1_4CD_clean_version.pdf.

23. Umbrecht, F., Wägli, P., Dechand, S., Gattiker, F., Neuenschwander, J., Sennhauser, U., and Hierold, C., "Wireless implantable passive strain sensor: design, fabrication, and characterization," *J. Micromech. Microeng.*, vol. 20, p. 085005, 2010.

24. Mencattelli, M., Donati, E., Cultrone, M., and Stefanini, C., "Customized load cell for three-dimensional force-moment measurements in orthodontics," in *5th IEEE RAS & EMBS International Conference on Biomedical Robotics and Biomechatronics (BioRob)*, São Paulo, Brazil, 2014, pp. 238-243.

25. Wilson, D. C., Niosi, C. A., Zhu, Q. A., Oxland, T. R., and Wilson, D. R., "Accuracy and repeatability of a new method for measuring facet loads in the lumbar spine," *J. Biomech.*, vol. 39, no. 2, pp. 348-353, 2006, doi: 10.1016/j.jbiomech.2004.12.011.

26. Du, P., Lu, H., and Zhang, X., "Measuring the young's relaxation modulus of PDMS using stress relaxation nanoindentation," in *MRS Proceedings*, Boston, MA, USA, Nov. 2009, vol. 1222.

27. Hussein, M. A., Mohammed, A. S., and Al-Aqeeli, N., "Wear characteristics of metallic biomaterials: a review," *Materials*, vol. 8, pp. 2749-2768, May 2015, doi: doi:10.3390/ma8052749.

28. Qiu, C., Adkins, N. J. E., and Attallah, M. M., "Microstructure and tensile properties of selectively laser-melted and of HIPed lased-melted Ti-6Al-4V," *Mater. Sci. Eng. A Struct. Mater.*, vol. 578, pp. 230-239, Aug. 2013, doi: https://doi.org/10.1016/j.msea.2013.04.099.

29. Leuders, S., Thöne, M., Riemer, A., Niendorf, T., Tröster, T., Richard, H. A., and Maier, H. J., "On the mechanical behaviour of titanium alloy TiAl6V4 manufactured by selective laser melting: Fatigue resistance and crack growth performance," *Int. J. Fatigue*, vol. 48, pp. 300-307, Mar. 2013, doi: https://doi.org/10.1016/j.ijfatigue.2012.11.011.

30. Benedetti, M., Torresani, E., Leoni, M., Fontanari, V., Bandini, M., Pederzolli, C., and Potrich, C., "The effect of post-sintering treatments on the fatigue and biological behaviour of Ti-6Al-4V ELI parts made by selective laser melting," *J. Mech. Behav. Biomed. Mater.*, vol. 71, pp. 295-306, July 2017, doi: https://doi.org/10.1016/j.jmbbm.2017.03.024.

31. Günther, J., Leuders, S., Koppa, P., Tröster, T., Henkel, S., Biermann, H., and Niendorf, T., "On the effect of internal channels and surface roughness on the

high-cycle fatigue performance of Ti-6Al-4V processed by SLM," *Mater. Des.*, vol. 143, pp. 1-11, 5 April 2018, doi: https://doi.org/10.1016/j.matdes.2018.01.042.

32. Yamaguchi, K., Thomas, A. G., and Busfield, J. J. C., "Stress relaxation, creep and set recovery of elastomers," *Int. J. Non Linear Mech.*, vol. 68, pp. 66-70, Jan. 2015, doi: https://doi.org/10.1016/j.ijnonlinmec.2014.07.004.

33. Loadstar Sensors. *iLoad Mini stainless steel miniature load cell*, Loadstar Sensors: Fremont, CA, USA, 1 Apr. 2010.

34. RDP Electrosense Inc. *Capacitive load cell type mcl*; document CD1048K, RDP Electrosense Inc.: Pottstown, PA, USA.

35. NXP Semiconductors. *FXTH870xD, Tire Pressure Monitor Sensor*; FXTH870xD Datasheet, rev. 1.6, NXP Semiconductors: Eindhoven, The Netherlands, Feb. 2019.

36. Kim, S. H., Moon, J., Kim, J. H., Jeong, S. M., and Lee, S., "Flexible, stretchable and implantable PDMS encapsulated cable for implantable medical device," *Biomed. Eng. Lett.*, vol. 1, pp. 199-203, 14 Sept. 2011, Art no. 199, doi: https://doi.org/10.1007/s13534-011-0033-8.

37. Roohpour, N., Wasikiewicz, J. M., Paul, D., Vadgama, P., and Rehman, I. U., "Synthesis and characterization of enhanced barrier polyurethane for encapsulation of implantable medical devices," *J. Mater. Sci: Mater. Med.*, vol. 20, pp. 1803-1814, 28 Apr. 2009, doi: 10.1007/s10856-009-3754-9.

38. Joung, Y., "Development of implantable medical devices: from an engineering perspective," *Int. Neurourol. J.*, vol. 17, 3, pp. 98-106, 30 Sept. 2013, doi: 10.5213/inj.2013.17.3.98.

Chapter 4

4 A Numerical Model of Monitoring Bone Healing in Fracture Fixation Applications using the FXTH87

4.1 Introduction

As described in Chapter 1, instrumentation of sensor packages within fracture fixation implants has been challenging, as the accompanying sensor must be small in size while having advanced power management and telemetry capabilities. A sensorized fracture fixation implant would allow scientists and clinicians to monitor variables such as load, deformation, acceleration, and temperature. Measuring real-time in-vivo load and deformation can be used to monitor the bone healing process following a fracture. Evaluating the healing process of long bones following a fracture is very subjective and it depends on the experience of a clinician to determine if the bone is on track to fully heal [1, 2]. Long bone nonunion is fairly common and occurs in about 2-7% of patients receiving a fracture fixation plate [3]. Prolonged nonunion can eventually result in implant fatigue failure, which leads to costly revision surgeries and tissue damage surrounding the affected region. From the long-bone fracture statistics presented in the thesis introduction, there is a clear need for an objective device capable of monitoring the bone healing process. With the development of the miniature wireless load cell device described in Chapter 2 and evaluated in Chapter 3, potential orthopaedic applications of the package can be explored.

To determine if the load cell could be feasible for use in fracture fixation applications, a model of the proposed implant, surrounding anatomy, and loading conditions must be described. This model would determine whether or not the load acting on the implants could result in deformation within the range of the FXTH87 sensor. If adequate deformation was feasible, then it is also important to ensure that the stresses in the implant remain below the yield strength for the material so that the implant does not fail. A preliminary investigation was performed to determine if the FXTH87 could be embedded within a fracture fixation plate. Fracture fixation plates are widely used to treat long bone fractures and are large enough to be able to potentially accommodate the placement of the FXTH87 without major design changes. This implementation of the FXTH87 sensor package is one of the more challenging orthopaedic applications, as the accompanying implant must be capable of transducing flexion into compression, which can be monitored by the sensor package. However, this application is still worth exploring, as the number of people that could benefit from an effective sensorized fracture fixation implant is large.

The bone fracture and treatment strategy described in this chapter is a distal femoral fracture stabilized using a distal lateral femoral locking plate. As was described in the introduction to this thesis, there are hundreds of thousands of femoral fractures every year around the world. With every fracture treated using a fixation plate, there is a risk of bone nonunion. Eliminating bone nonunion not only improves patient outcomes by eliminating the need for revision surgeries, but it also decreases healthcare costs. A locking plate was selected as the fixation device because, as was described in the thesis introduction, a locking plate promotes secondary bone healing, which enables motion between bone fragments. This small implant flexure may be measurable by an internal sensor package. In addition, most locking plates are large enough to accommodate the modified FXTH87 sensor package without major design changes.

Many finite element models describing long bone fracture fixation have been previously published [4-16]; however, the outcome variables in the models are different from the variables being measured in the model proposed in this thesis chapter. In the model proposed in this chapter, a simulation is performed to determine if internal compression occurs within the custom implant during loading. The previously described models are focused on determining if their own custom sensor package could be feasible to be embedded within a fracture fixation implant to monitor bone healing. The sensor package in a majority of these publications is a strain gauge system. The fixation implants used in the models are not trying to convert flexure into compression, as their sensor packages inherently measure strain and flexure. Similar to the model proposed in this chapter, previously described models monitor the stresses acting on the fixation plate and screws to ensure that maximum stress values are well below the yield strength of the material used to fabricate the implants. While it may be challenging to compare the outcome variables from the proposed model to previously described models, the existing models can act as guide for creating our own realistic loading scenario.

In this chapter, two models simulating fracture fixation were generated in the finite element analysis software ABAQUS. The first model was a simple (non-physiological) model while the second model was created using a 3D CAD model of a human bone and a fracture fixation plate. With a successful model, an analysis can be performed to determine if the FXTH87 sensor package could be an effective tool to monitor in-vivo load and bone healing. The working principle of the models was that as load was applied to the proximal bone segment, the fixation implant would slightly bend. The flexure in the implant would decrease the distance between two surfaces in an internally located cavity. This deformation would contact the surface of the modified FXTH87, and through a calibration, load could be determined. As time passes, the osteotomy gap between bone fragments begins to heal, and the bone starts to bear more of the load acting through the structure. When the bone is fully healed the fracture fixation plate bears no load, which results in no deformation of the implant and no signal measured by the FXTH87. In the simple bone model, the implant flexed a sufficient amount to cause compression to occur inside the implant. As simulated healing was applied, the amount of internal cavity compression decreased as expected. In the realistic loading model, compression of the internal cavity inside the implant was not observed. In both models, the maximum stresses in the fixation plates were very close to the yield stress of the material used to model the implants.

4.2 Methods

4.2.1 Simple Long Bone Fracture Fixation Model

As was described in Section 4.1, two models simulating fracture fixation were generated in the finite element analysis software ABAQUS. Both models were generated using the published work describing fracture fixation modelling discussed in Section 4.1. However, the implants used in the proposed models are customized to accommodate the FXTH87 sensor package. The first model was a simple model of the bone, fixation plate, and screws. In this model, the two bone segments were modelled as hollow cylinders, and the screws used in the model were all solid cylinders. The custom fixation plate used in the model was a simple proof-of-concept implant that resembled the shape and size of clinically available components (Figure 4.1). However, modifications had to be made to the implant so that the FXTH87 sensor could theoretically be embedded within the component. Over the central region of the implant there is a noticeable bulge, where the sensor package would be placed. Inside this material bulge is a hollow rectangular cavity. The thickness of the rectangular cavity is approximately 4 mm, which is just slightly larger than the height of the FXTH87 and accompanying printed circuit board.

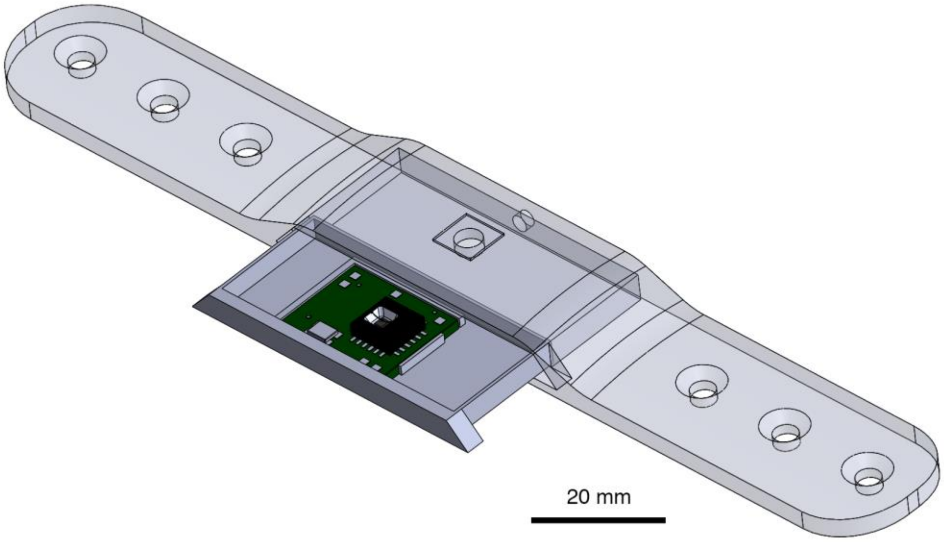

Figure 4.1: SolidWorks model of fixation implant used in finite element analysis with embedded FXTH87 and circuit board.

To simulate a long bone diaphyseal fracture, the two hollow cylinders were placed on top of each other and separated by a small osteotomy gap of 2 mm. This osteotomy gap was determined based on previously published models and clinical observations of osteotomy gaps [4, 17-20]. The custom fixation implant was placed over the center of the osteotomy gap and was fixed to the surface of the bone segments using tie constraints. On each side of the osteotomy gap, three screws of 4 mm diameter were inserted through the implant and the bone segment (Figure 4.2). Screws were fixed to the bone segment and fixation component using tie constraints. Linear static analysis with tetrahedral elements (0.5 mm size) were used to model the assembly. The fixation component and screws were modelled as solid homogenous Ti-6Al-4V with an elastic modulus of 113.8 GPa and a Poisson’s ratio of 0.342 [21], as in Chapter 3. Bone was modelled as a solid homogeneous material with an elastic modulus of 18 GPa and a Poisson’s ratio of 0.3 [22-24]. For simplicity, fixation of the plate-bone, plate-screw, and bone-screw interface was obtained using tie constraints. Surface-to-surface contact with frictionless behaviour was modelled between the implant and bone segments. One body weight of load was applied as a pressure force on the top surface of the proximal bone segment. The bottom surface of the distal bone segment was held fixed to prevent displacement in any direction.

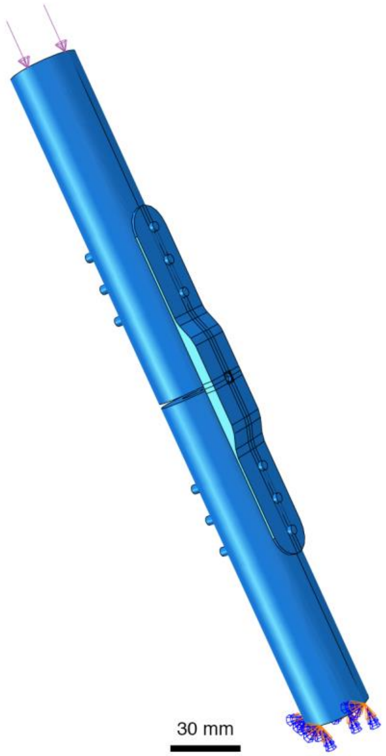

Figure 4.2: Simplified fracture fixation assembly with load and boundary conditions in ABAQUS.

From the results of the deformed model, the distance between the center of the top and bottom surface of the rectangular sensor cavity within the implant was obtained. This will determine if sufficient deformation is occurring in the internal cavity. As was described in Chapter 2, deformation of only a few hundred microns can be measured by the

FXTH87 sensor package. In addition, the stress values observed in the fixation component and screws were quantified and compared to published yield stress value for Ti-6Al-4V. In follow up experiments, the osteotomy gap between bone segments was filled with a material of increasing elastic modulus until the modulus within the gap was the same as bone. The elastic modulus values ranged from 0.5 MPa to 18 GPa. The modulus values used for each test were determined based on published studies describing the evolving elastic modulus of the bone callus during the long bone healing process [14, 25-28]. When the osteotomy gap was filled with a material of healthy bone properties, this simulated fully healed bone. After each test, the distance between the top and bottom surface of the internal cavity in the implant was measured. As discussed in Section 4.1, it is expected that as the bone is healing the implant bears less load, therefore resulting in less internal deformation of the rectangular sensor cavity.

4.2.2 Femoral Fracture Fixation Model

A second model was developed to simulate a more realistic implant-loading scenario. For this analysis, a distal fracture of the femur was modelled. Instead of using two hollow cylinders, a 3D CAD model of a human femur bone was used for testing. The fixation implant used in this model was developed by drawing a sketch on the surface of the distal lateral intact portion of the bone. The size and shape of the implant was approximated using measurements made from clinically available implants. The implant sketch was extruded to generate a 3D implant with thickness comparable to clinical implants but with a surface geometry that perfectly matched the shape of the bone (Figure 4.3). This simplifies the analysis, as contact is easier to model at the implant-bone interface. Simple circular screw holes were cut in the implant in locations similar to in clinical implants. Similar to the first model, a rectangular cavity was introduced in the fixation implant to simulate where the FXTH87 sensor package would be placed (Figure 4.4). The rectangular cavity was positioned to be centered around the location of osteometry gap described below.

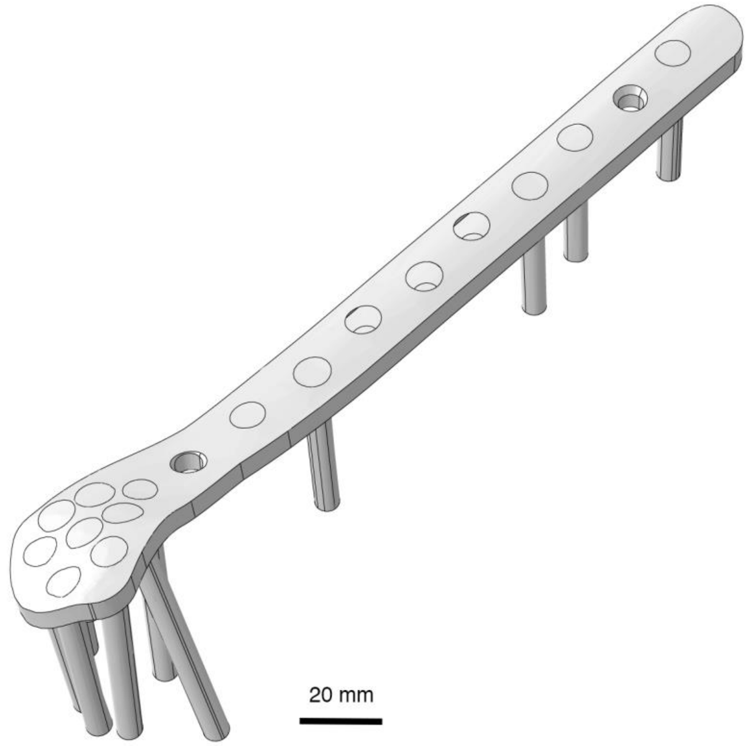

Figure 4.3: Custom fixation plate modelled in ABAQUS.

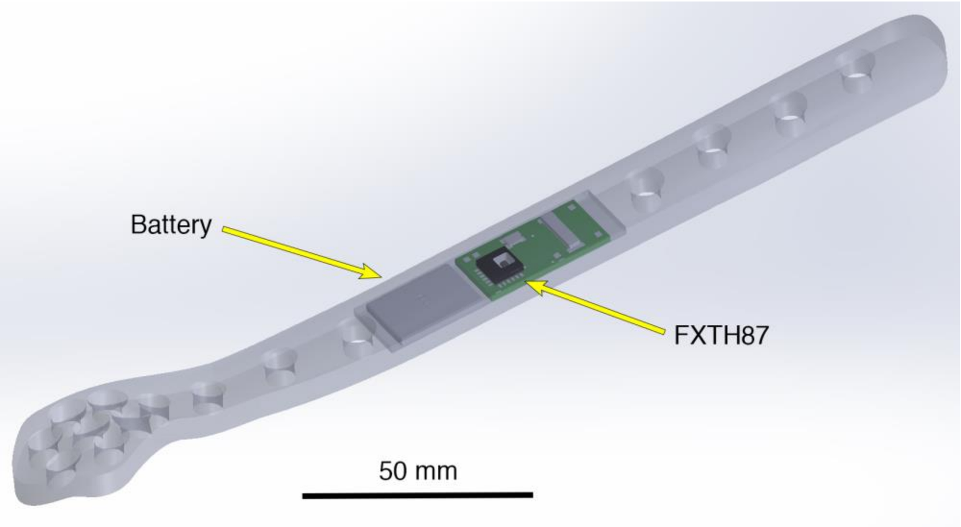

Figure 4.4: Partially transparent isometric view of the custom fracture fixation plate indicating the location of the rectangular cavity. Modelled in SolidWorks.

To simulate a distal femoral fracture, a small section of the model of the femur was removed, which left the two segments separated by an osteotomy gap of 10 mm. The size and location of the osteotomy gap was determined by the previously described published femoral fracture models. The custom fixation implant was placed on the distal lateral region of the femur. The proximal region of the implant was positioned in the diaphysis of the bone and the distal region of the implant curved around the lateral epicondyle of the femur. The osteotomy gap was located near the distal diaphyseal region of the femur. This was to ensure a level rectangular cavity could be generated in the implant. If the sensor cavity was closer to the distal end, the implant curves, making it more challenging to create a feasible cavity. The implant was fixed to the surface of the bone segments using tie constraints. In addition, surface-to-surface contact with frictionless behaviour was modelled between the implant and bone segments. On the proximal side of the osteotomy gap, screws of 4 mm diameter were inserted through the implant and the bone segment (Figure 4.5). On the distal side of the osteotomy gap, 7 screws were inserted into the epicondyle. Screws were fixed to the bone segment and fixation component using tie constraints. Linear static analysis with quadratic tetrahedral elements (0.5 mm size) were used to model the assembly. The fixation component and screws were modelled as solid homogenous Ti-6Al-4V with an elastic modulus of 113.8 GPa and a Poisson’s ratio of 0.342 [21]. Bone was modelled as a solid homogeneous material with an elastic modulus of 18 GPa and a Poisson’s ratio of 0.3 [22-24]. One body weight of load was applied to the femoral head at the proximal end of the bone. The bottom surface of the distal epicondyles was held fixed to prevent displacement in any direction.

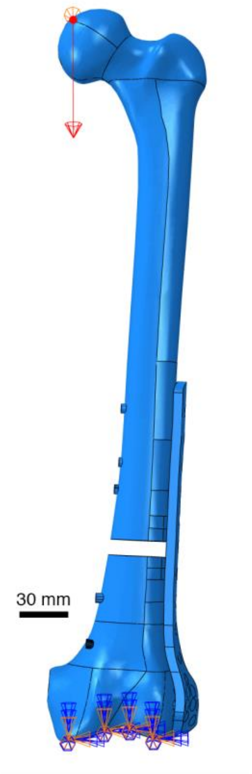

Figure 4.5: Femur, fixation plate, and screw assembly with load and boundary conditions in ABAQUS.

From the results of the deformed model, the distance between the center of the top and bottom surface of the rectangular sensor cavity embedded in the implant was obtained. This will determine if sufficient deformation is occurring in the internal cavity. Deformation of only a couple of hundred microns can be measured by the FXTH87 sensor package. In addition, the stress values observed in the fixation component and screws were quantified and compared to published yield stress value for Ti-6Al-4V.

4.3 Results

From the first model, a relationship was observed between callus modulus and distance between the top and bottom surfaces of the cavity in the fixation component (Figure 4.6). As the modulus of the callus increased, the distance between the two surfaces decreased. In other words, as the bone began to heal the deformation of the implant decreased to zero. At the maximum point of deformation, when there was no callus material present, the maximum deformation change was 162 microns. The maximum stresses in the implant and screws at maximum deformation were 844 MPa (Figure 4.7). This is slightly less than the published yield stress value for Ti-6Al-4V [21], which in tension is 880 MPa and in compression is 970 MPa. The maximum stress value is greater than the fatigue strength value for Ti-6Al-4V [29]. The location of maximum stress on the implant was on the bottom surface of the implant at the center of the osteotomy gap (Figure 4.8, Figure 4.9).

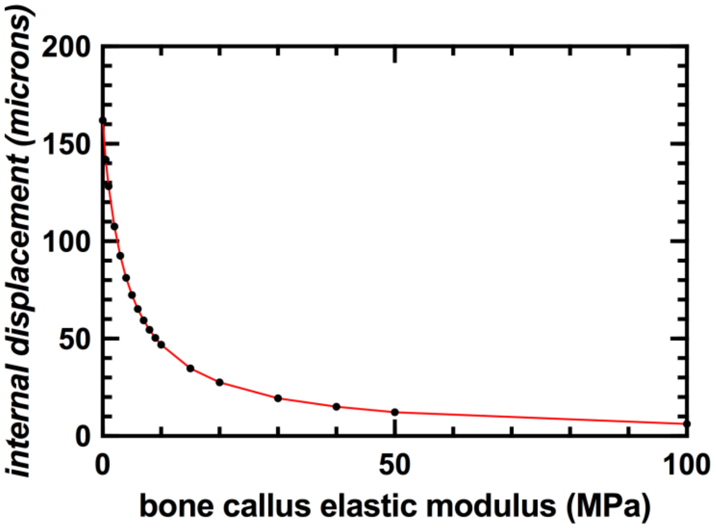

Figure 4.6: Internal cavity change in displacement vs. increasing bone callus elastic modulus.

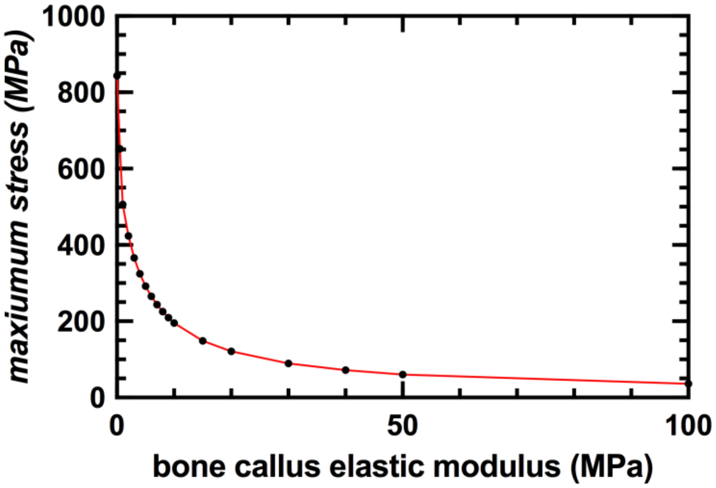

Figure 4.7: Maximum stress in the Ti-6Al-4V implant during 1 BW loading with varying bone callus elastic modulus.

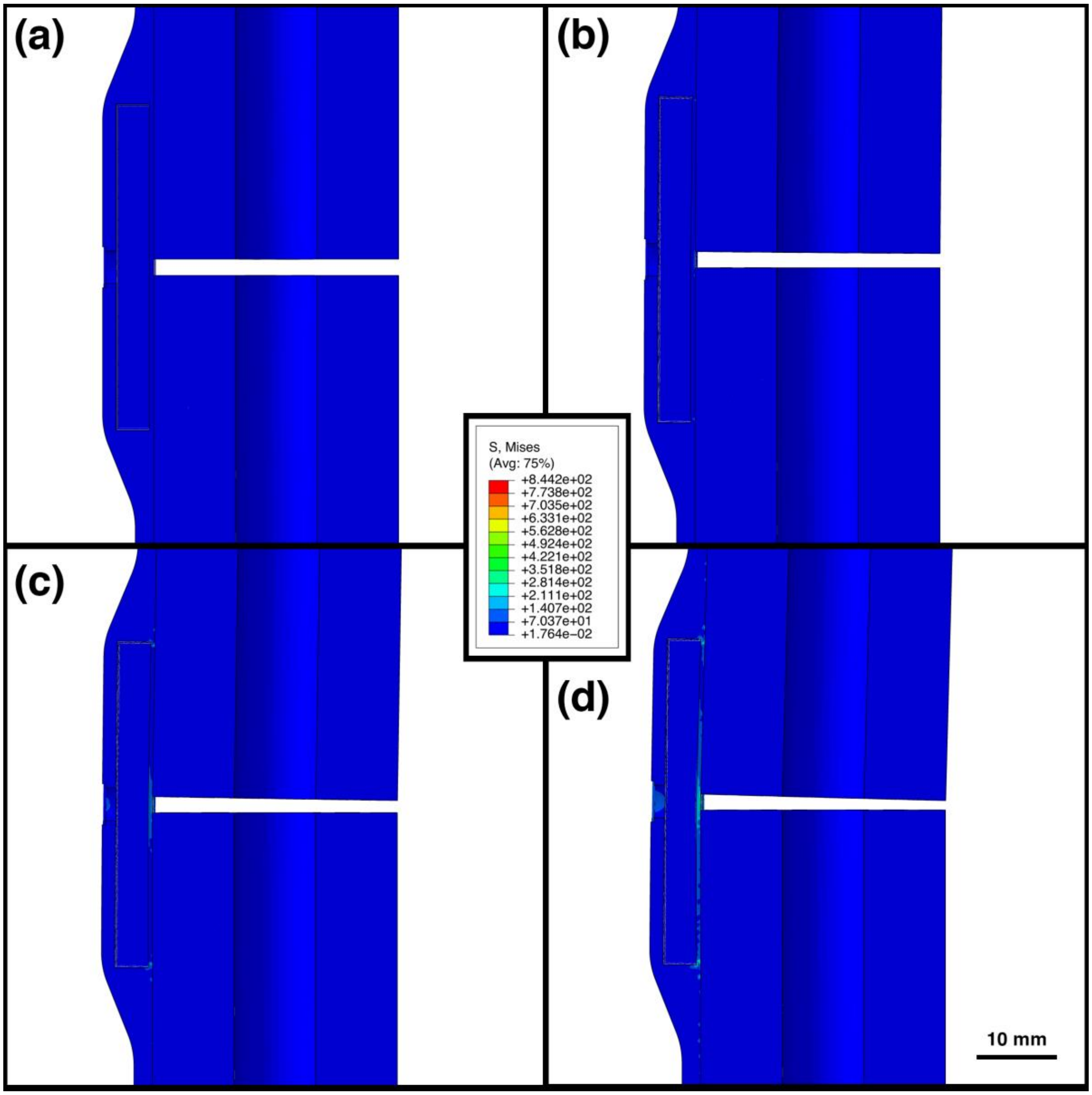

Figure 4.8: Cross section view of simple fracture fixation model depicting stresses at various deformation levels. (a) step 0/10, (b) step 3/10, (c) step 6/10, (d) step 10/10.

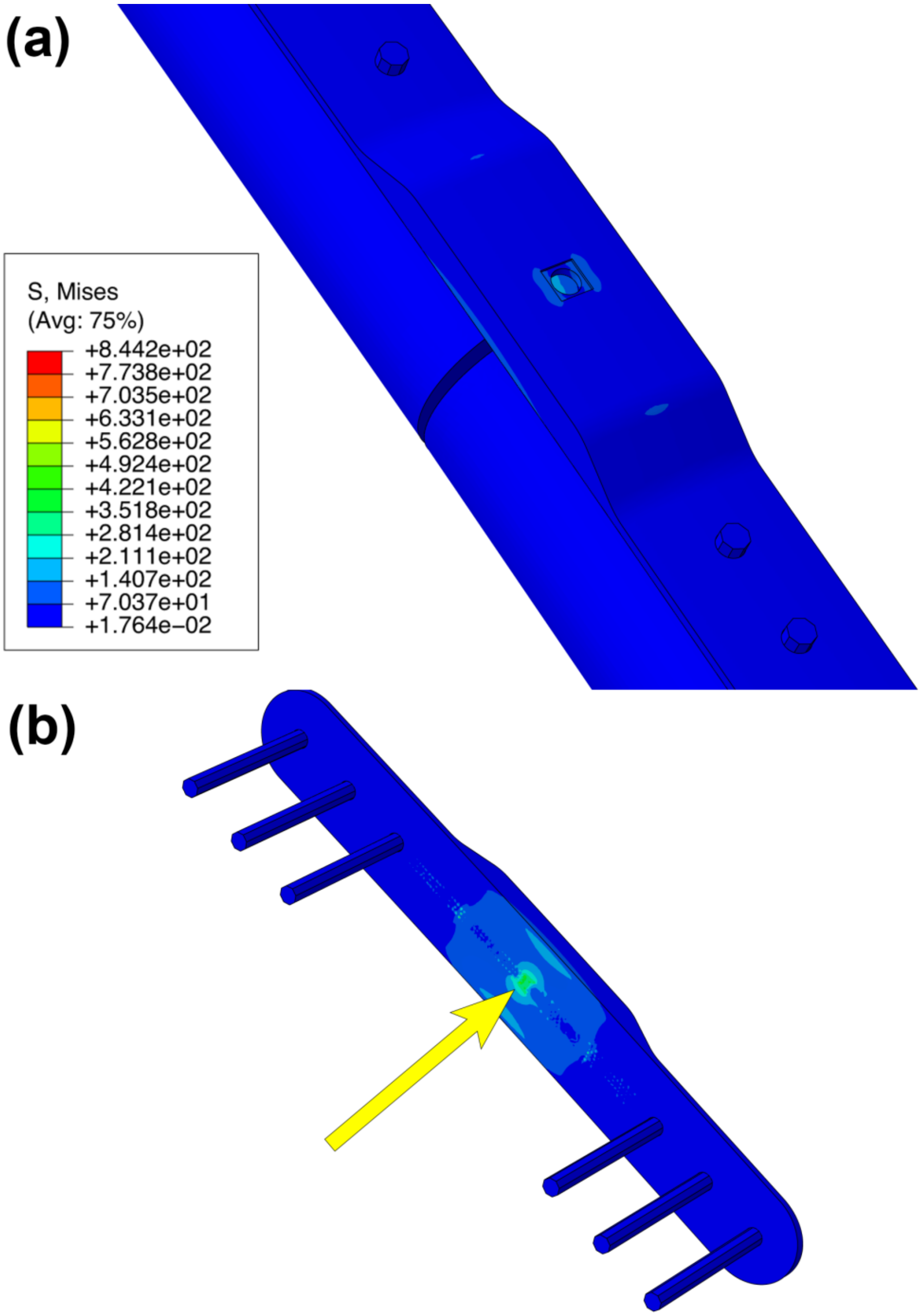

Figure 4.9: (a) Stress distribution on the simple fixation model. (b) Location of maximum stress on the Ti-6Al-4V implant (arrow).

From the second model, the realistic loading scenario, deformation exceeding 5 microns did not occur in the rectangular cavity even when the osteotomy gap was filled with no material. The maximum stress in the implant and screws were 672 MPa, which is less than the published yield stress value of Ti-6Al-4V (Figure 4.10, Figure 4.11). However, the maximum stress value is above the fatigue strength value for Ti-6Al-4V [29].

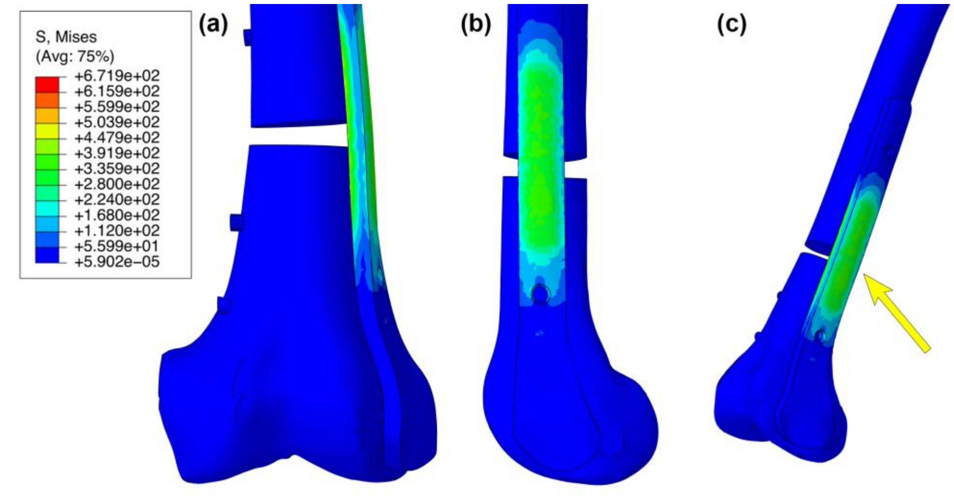

Figure 4.10: (a) Front view of distal femur fixation assembly. (b) Side view. (c) Isometric view with location of maximum stress (arrow).

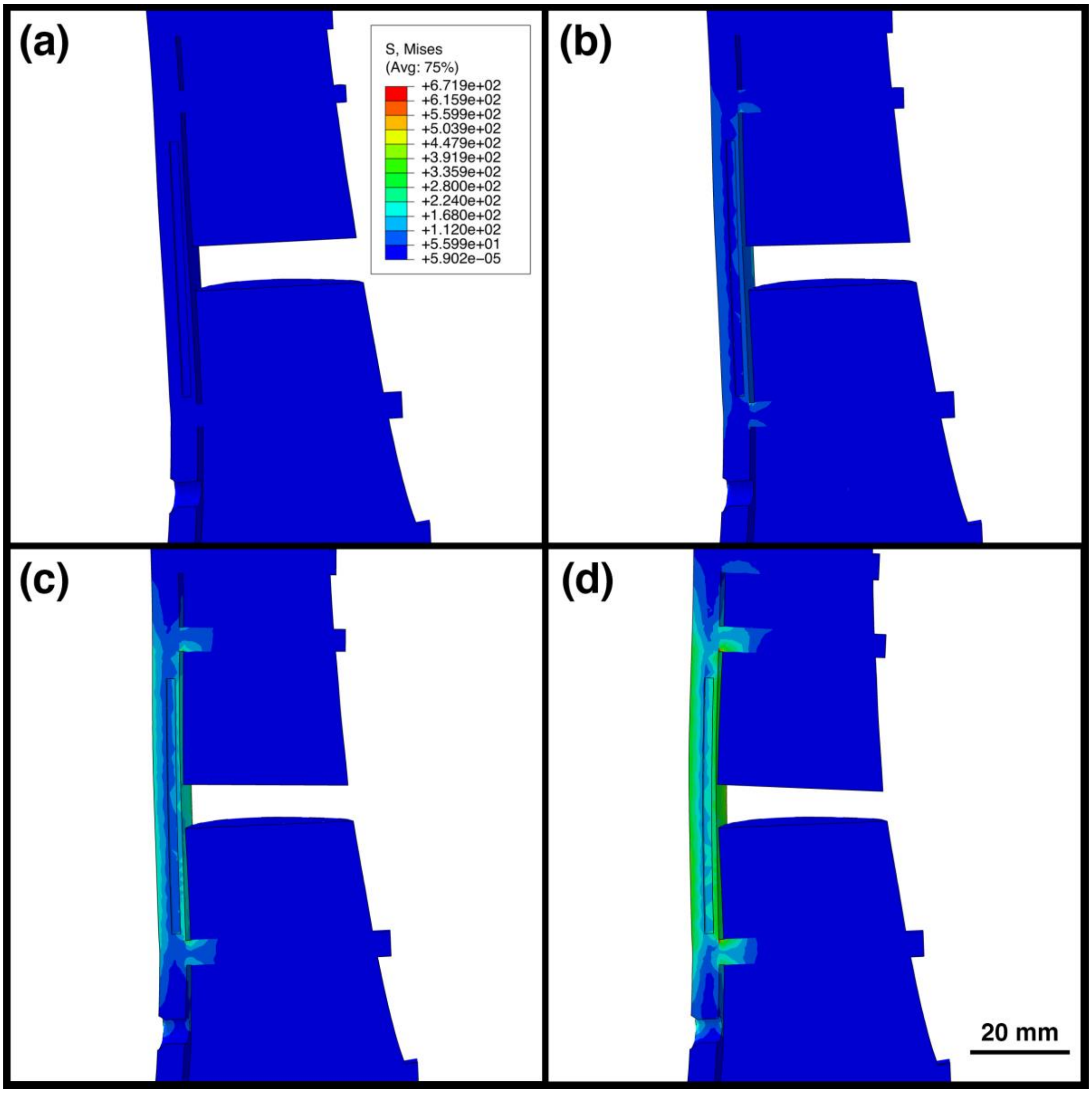

Figure 4.11: Cross section view of realistic fracture fixation model depicting stresses at various deformation levels. (a) step 0/10, (b) step 3/10, (c) step 6/10, (d) step 10/10.

4.4 Discussion

In this study, two fracture fixation models were developed to simulate implant loading immediately following surgery and during the progression of bone healing. From the results of the first model, a simple implant loading model, a relationship was reported between callus modulus and deformation of the internal cavity in the fixation plate. As the modulus of the callus material increased, the internal deformation of the cavity decreased. This result was expected because as the bone begins to heal it begins to bear the load acting through the region. As a reduced load was applied to the implant, the flexure of the implant decreased, resulting in less compression of the internal cavity. The maximum implant stresses in the first model did not exceed the published yield stress for Ti-6Al-4V. However, as the maximum stresses are close to the published yield stress value and exceed the published fatigue strength value, the implant would likely fail due to fatigue in a short number of cycles. In the second finite element model, comprised of parts matching the geometry of human anatomy, a relationship similar to the one observed in the first model was not reported. Even at a stage with no bone callus modulus in place there was no internal deformation in the implant. Similar to the first model, the maximum stresses in the implant were less than the published yield stress values and greater than the fatigue strength value for titanium alloy.

The results of this study strongly indicate that a fracture fixation flexure scenario is unlikely to be found where the implant internally deforms while the maximum stresses remain below the yield stress of the material. As was described in Section 4.1, transducing flexure into compression in a fixation model is one of the more challenging orthopaedic applications. For adequate compression to occur it requires significant flexure of the implant, which results in high internal stresses. The results indicate that the FXTH87 may be better suited for an orthopaedic application that is purely under a compressive force, as the sensor inherently measures compressive deformation. Examples of orthopaedic components subjected to compression include spinal fusion cages, high-tibial osteotomy implants, vertebral replacements, and knee replacements to name a few.

From the results of the first model, the simplistic loading scenario, it was shown that it may be possible to monitor the change in implant loading during the bone healing process. The maximum deformation that occurs when there is no material in the osteotomy gap is a little over 160 microns. The described FXTH87 sensor package is easily capable of monitoring this small change in deformation. The FXTH87 would be capable of monitoring implant load until the callus modulus exceeds 100 MPa. While the graph of callus modulus vs. internal cavity displacement drops significantly as callus modulus increases it is important to note that immediately following a fracture the callus modulus would be very low for a period of days or even weeks [14]. Therefore, the FXTH87 would be effective at monitoring the early progress of bone healing. Another important factor to take into consideration is that the implant cavity deformation is very small up to and exceeding 100 MPa. There is a large difference between 100 MPa and the elastic modulus of healthy compact bone, which is approximately 18 GPa [22-24]. If the scenario observed in the first model was replicated in a clinical setting, then the FXTH87 would have a difficult time differentiating between fully healed bone and bone partially through the healing process (callus modulus = 100 MPa). Therefore, it would be dangerous to remove the implant even if the FXTH87 was reporting that the implant was not flexing. The original problem of clinicians not knowing when the bone is fully healed would still be present. However, evidence could be provided in the early stages following a fracture indicating that the healing process has successfully initiated.

From the results of the second model, the realistic loading scenario, it was shown that the FXTH87 sensor package would not be capable of monitoring bone healing. Even when no bone callus material is present in the osteotomy gap, the internal sensor cavity in the implant does not deform a sufficient amount. As the FXTH87 is a displacement sensor, essentially zero deformation of the internal cavity would prevent signal values from being obtained. The maximum stresses at one body weight load were below the yield strength value for Ti-6Al-4V. While minimal stress is a preferable scenario, it is not that important in this case because the flexure of the beam was not capable of actuating deformation to the FXTH87. The ideal scenario would have been stresses well below the yield limit while the flexure of the beam is enough for the FXTH87 to measure. Reasons why the internal cavity of the implant did not deform sufficiently include implant design and model geometry. The implant used in the second model was designed to replicate the geometry of clinically available fracture fixation plates. As was described, the rectangular internal cavity was placed proximally in the implant so that a level region of the implant could be used. When the internal cavity was introduced in the implant the wall thickness surrounding the cavity was slightly thicker than it was in the simplistic model. This generated an implant with better support that is more resistant to bending. Sacrificing wall thickness to achieve flexure goals would directly result in an increase in local stress.

This is because the same force is being applied over a small area. This increase in stress would likely push the maximum stress over the yield limit of the material. This is observed in the first model as the implant wall thickness around the cavity may be slightly less than in the second model, but the stresses are much higher. In addition to increased wall thickness, the fixation plate was contoured to conform to the native anatomy of the bone. This curvature in the plate increases the stiffness of the implant, therefore reducing the deformation capacity of the implant. This can be validated using hand calculations and numerical modelling. In comparison to a hollow rectangular structure, similar to the structure observed in the simplistic model, a curved structure has an increased area moment of inertia. This is true even when the cross-sectional area of the cantilever structure is identical for both rectangular and contoured beams. From the flexure equations of cantilever beams, increasing area moment of inertia increases structure stiffness and decreases maximum deformation during loading [30]. A real-life example of the effect beam curvature can have on construct stiffness and resistance to bending is a tape measure. The tape is precisely contoured with a convex and concave surface to increase the stiffness of the structure. This allows the tape to be extended multiple feet before the structure buckles. If the tape was a simple rectangle, the extension capacity of the tape would be reduced, which would reduce the effectiveness of the measuring tool. The geometry of the parts used to create the model also influence the flexure capacity of the fixation implant. As was described, the parts used to generate this model are geometrically similar to real life bones and implants. Therefore, the realistic loading scenario is not perfectly symmetrical, like what was observed in the simplified fracture fixation model. From bending theory, a symmetrical model promotes the most flexion in the center of the beam structure [30]. Unfortunately, due to the complex anatomy of human bone and the implant geometry required to stabilize the selected fracture, it is unlikely a configuration could be described that is perfectly symmetrical to ensure that the most flexure occurs at the exact location of the embedded sensor package.

While it may be possible to make alterations to the model to promote increased implant flexure, it would come at a cost that would likely decrease the effectiveness of the fixation implant. As was mentioned above, the wall thickness of the fracture fixation plate could be decreased. This would generate an implant that is less resistant to bending.

However, the resulting stresses in the region would increase due to stress acting through a smaller cross section. Another design change that could promote increased flexion would be to increase the working length of the implant. The working length of a fixation implant is defined by the distance between the screws on either side of the osteotomy gap. Previous published studies have shown that increasing the working length of the implant promotes greater motion and less resistance to bending [4, 31-33]. This can be verified from bending theory, as the longer the beam the greater the maximum deflection [30]. However, to generate flexure required to deform the internal cavity in the implant the working length would have to be greatly increased. Previously published studies have described that both large and small working lengths can result in a reduced fatigue life [34, 35]. The ideal scenario is a medium working length that promotes small fragment motion while still being rigid [36, 37]. While further changes could be made to the model it is unlikely that a fixation solution can be found that would generate implant flexure and still have a long fatigue life. The osteotomy gap used in the second model is already significantly larger than the gap in typical clinical cases. This demonstrates that even a fixation solution with a large working length is not able to generate enough flexure to deform the implant cavity onto the FXTH87. In addition, the osteotomy gap had to be positioned near a location in the implant that could accommodate the placement of the FXTH87. This location was determined to be in the diaphysis region of the femur. It was described in Chapter 1 that a fracture in this location would almost never be treated by a fracture fixation plate; an intramedullary nail is preferable for fractures in the diaphysis region of the bone.

From the results of this study, it is unlikely that the FXTH87 would be capable of monitoring the bone healing process following a distal femoral fracture and is better suited for orthopaedic components under compression. Significant alterations would have to made to the models to reduce stress while promoting implant flexure. Unfortunately, to achieve the flexure required to deform the implant, the stresses would exceed the yield limit of the material. In addition, large flexure may result in too much interfragmentary motion, which can halt the normal bone healing process [4, 20]. While it is briefly investigated in the first fixation model, a fixation plate instrumented with an FXTH87 would likely only be feasible in diaphyseal fractures in long bones. However, implant stresses were very high, the FXTH87 cannot capture the full healing process, and fracture fixation plates are not commonly used to treat diaphyseal fractures. Future studies should investigate the feasibility of the FXTH87 in orthopaedic components under compression, such as spinal fusion cages, vertebral replacements, high-tibial osteotomy implants, and joint replacements.

4.5 Acknowledgements

The authors would like to thank Todor Ivanov for his help performing modelling in ABAQUS as well as Dr. Radovan Zdero and Aaron Gee for providing CAD models of a femur bone and fixation implant. This work was supported in part by the Canadian Institute of Health Research (Foundation Program) under Grant FDN-148474, the Ontario Research Fund (Research Excellence) under Grant RE-07-666, and The Collaborative Training Program in Musculoskeletal Health Research at Western University. D. W. Holdsworth is supported as the Dr. Sandy Kirkley Chair in Musculoskeletal Research at Western University.

4.6 References

1. Leow, J. M., Clement, N. D., Tawonsawatruk, T., Simpson, C. J., and Simpson, A. H. R. W., "The radiographic union scale in tibial (RUST) fractures: reliability of the outcome measure at an independent centre," *Bone Joint Res.*, vol. 5, no. 4, pp. 116-121, 12 Apr. 2016, doi: https://doi.org/10.1302/2046-3758.54.2000628.

2. Bhandari, M., Guyatt, G. H., Swiontkowski, M. F., Tornetta, P., Sprague, S., and Schemitsch, E. H., "A lack of consensus in the assessment of fracture healing among orthopaedic surgeons," *J. Orthop. Trauma*, vol. 16, no. 8, pp. 562-566, Sept. 2002.

3. Tzioupis, C. and Giannoudis, P. V., "Prevalence of long-bone non-unions," *Injury*, vol. 38, 2, pp. S3-S9, May 2007, doi: https://doi.org/10.1016/S0020-1383(07)80003-9.

4. Märdian, S., Schaser, K., Duda, G. N., and Heyland, M., "Working length of locking plates determines interfragmentary movement in distal femur fractures under physiological loading," *Clin. Biomech.*, vol. 30, no. 4, pp. 391-396, May 2015, doi: https://doi.org/10.1016/j.clinbiomech.2015.02.006.

5. Das, S. and Sarangi, S. K., "Finite element analysis of femur fracture fixation plates," *Int. J. Basic Appl. Biol.*, vol. 1, no. 1, pp. 1-5, 2014.

6. Zhang, W., Li, J., Zhang, H., Wang, M., Li, L., Zhou, J., Guo, H., Li, Y., and Tang, P., "Biomechanical assessment of single LISS versus double-plate osteosynthesis in the AO type 33-C2 fractures: a finite element analysis," *Injury*, vol. 49, no. 12, pp. 2142-2146, Dec. 2018, doi: https://doi.org/10.1016/j.injury.2018.10.011.

7. Prayson, M. J., Datta, D. K., and Marshall, M. P., "Mechanical comparison of endosteal substitution and lateral plate fixation in supracondylar fractures of the femur," *J. Orthop. Trauma*, vol. 15, no. 2, pp. 96-100, Feb. 2001.

8. Cegoñino, J., García Aznar, J. M., Doblaré, M., Palanca, D., Seral, D., and Seral, F., "A comparative analysis of different treatments for distal femur fractures using the finite element method," *Comput. Methods Biomech. Biomed. Engin.*, vol. 7, no. 5, pp. 245-256, 21 Aug. 2006, doi: https://doi.org/10.1080/10255840412331307182.

9. Elkins, J., Marsh, J. L., Lujan, T. J., Peindl, R., Kellam, J., Anderson, D. D., and Lack, W., "Motion predicts clinical callus formation: contruct-specific finite element analysis of supracondylar femoral fractures," *J. Bone Joint Surg. Am.*, vol. 98, no. 4, pp. 276-284, 17 Feb. 2016, doi: 10.2106/JBJS.O.00684.

10. Wieding, J., Souffrant, R., Fritsche, A., Mittelmeier, W., and Bader, R., "Finite element analysis of osteosynthesis screw fixation in the bone stock: an

appropriate method for automatic screw modelling," *PLoS ONE*, vol. 7, no. 3, p. e33776, 28 Mar. 2012, doi: https://doi.org/10.1371/journal.pone.0033776.

11. Borchani, W., Aono, K., Lajnef, N., and Chakrabartty, S., "Monitoring of postoperative bone healing using smart trauma-fixation device with integrated self-powered piezo-floating-gate sensors," *IEEE Trans. Biomed. Eng.*, vol. 63, pp. 1463-1472, 2016, doi: doi:10.1109/tbme.2015.2496237.

12. Tan, Y., Hu, J., Ren, L., Zhu, J., Yang, J., and Liu, D., "A passive and wireless sensor for bone plate strain monitoring," *Sensors*, vol. 17, no. 11, p. 2635, 16 Nov. 2017, doi: 10.3390/s17112635.

13. Mehboob, H. and Chang, S., "Evaluation of healing performance of biodegradable composite bone plates for a simulated fractured tibia model by finite element analysis," *Compos. Struct.*, vol. 111, pp. 193-204, May 2014, doi: https://doi.org/10.1016/j.compstruct.2013.12.013.

14. Kim, H., Kim, S., and Chang, S., "Finite element analysis using interfragmentary strain theory for the fracture healing process to which composite bone plates are applied," *Compos. Struct.*, vol. 93, no. 11, pp. 2953-2962, Oct. 2011, doi: https://doi.org/10.1016/j.compstruct.2011.05.008.

15. Wang, J., Zhang, X., Li, S., Yin, B., Liu, G., Cheng, X., and Zhang, Y., "Plating system design determines mechanical environment in long bone mid-shaft fractures: a finite element analysis," *J. Invest. Surg.*, vol. 33, no. 8, pp. 699-708, 19 Mar. 2020.

16. Nassiri, M., MacDonald, B., and O'Byrne, J. M., "Computational modelling of long bone fractures fixed with locking plates - how can the risk of implant failure be reduced?," *J. Orthop.*, vol. 10, no. 1, pp. 29-37, Mar. 2013, doi: https://doi.org/10.1016/j.jor.2013.01.001.

17. Higgins, T., Pittman, G., Hines, J., and Bachus, K. N., "Biomechanical analysis of dital femur fracture fixation: fixed-angle screw-plate construct versus condylar blade plate," *J. Orthop. Trauma*, vol. 21, no. 1, pp. 43-46, Jan. 2007, doi: 10.1097/BOT.0b013e31802bb372.

18. Augat, P., Margevicius, K., Simon, J., Wolf, S., Suger, G., and Claes, L., "Local tissue properties in bone healing: influence of size and stability of the osteotomy gap," *J. Orthop. Res.*, vol. 16, no. 4, pp. 475-481, 18 Feb. 2005, doi: https://doi.org/10.1002/jor.1100160413.

19. Gómez-Benito, M. J., García-Aznar, J. M., Kuiper, J. H., and Doblaré, M., "Influence of fracture gap size on the pattern of long bone healing: a computational study," *J. Theor. Biol.*, vol. 235, no. 1, pp. 105-119, 7 Jul. 2005, doi: https://doi.org/10.1016/j.jtbi.2004.12.023.

20. Claes, L., Augat, P., Suger, G., and Wilke, H., "Influence of size and stability of the osteotomy gap on the success of fracture healing," *J. Orthop. Res.*, vol. 15, no. 4, pp. 577-584, 18 Feb. 2005, doi: https://doi.org/10.1002/jor.1100150414.

21. "Titanium Ti-6Al-4V (Grade 5), Annealed." ASM Aerospace Specification Metals Inc. http://asm.matweb.com/search/SpecificMaterial.asp?bassnum=MTP641.

22. Merz, B., Eckstein, F., Hillebrand, S., and Putz, R., "Mechanical implications of humero-ulnar incongruity — finite element analysis and experiment," *J. Biomech.*, vol. 30, no. 7, pp. 713-721, 1997.

23. Cuppone, M., Seedhom, B. B., Berry, E., and Ostell, A. E., "The longitudinal young's modulus of cortical bone in the midshaft of human femur and its correlation with CT scanning data," *Calcif. Tissue Int.*, vol. 74, no. 3, pp. 302-309, 2004.

24. Bourne, B. C. and van de Meulen, M. C., "Finite element models predict cancellous apparent modulus when tissue modulus is scaled from speciment CT-attenuation," *J. Biomech.*, vol. 37, no. 5, pp. 613-621, 2004.

25. Leong, P. L. and Morgan, E. F., "Measurement of fracture callus material properties via nanoindentation," *Acta Biomater.*, vol. 4, no. 5, pp. 1569-1575, Sept. 2008, doi: https://doi.org/10.1016/j.actbio.2008.02.030.

26. Manjubala, I., Liu, Y., Epari, D. R., Roschger, P., Schell, H., Fratzl, P., and Duda, G. N., "Spatial and temporal variations of mechanical properties and mineral content of the external callus during bone healing," *Bone*, vol. 45, no. 2, pp. 185-192, Aug. 2009, doi: https://doi.org/10.1016/j.bone.2009.04.249.

27. Mora-Macías, J., Giráldez-Sánchez, M. Á., López, M., Domínguez, J., and Reina-Romo, M. E., "Comparison of methods for assigning the material properties of the distraction callus in computational models," *Int. J. Numer. Method Biomed. Eng.*, vol. 35, no. 9, p. e3227, 13 Jun. 2019, doi: https://doi.org/10.1002/cnm.3227.

28. Gardner, T. N., Stoll, T., Marks, L., Mishra, S., and Knothe-Tate, M., "The influence of mechanical stimulus on the pattern of tissue differentiation in a long bone fracture - an fem study," *J. Biomech.*, vol. 33, no. 4, pp. 415-425, Apr. 2000, doi: https://doi.org/10.1016/S0021-9290(99)00189-X.

29. Janeček, M., Novy, F., Harcuba, P., Strásky, J., Trško, L., and Mhaede, M., "The very high cycle fatigue behaviour of Ti-6Al-4V alloy," *Acta. Phys. Pol. A*, vol. 128, no. 4, pp. 497-503, Oct. 2015, doi: 10.12693/APhysPolA.128.497.

30. Beer, F. P., Johnston, E. R., DeWolf, J. T., and Mazurek, D. F., *Mechanics of Materials*, Sixth ed. McGraw-Hill, 2012.

31. Hoffmeier, K. L., Hofmann, G. O., and Mückley, T., "Choosing a proper working length can improve the lifespan of locked plates: a biomechanical study," *Clin. Biomech.*, vol. 26, no. 4, pp. 405-409, May 2011, doi: https://doi.org/10.1016/j.clinbiomech.2010.11.020.

32. Kanchanomai, C., Muanjan, P., and Phiphobmongkol, V., "Stiffness and endurance of a locking compression plate fixed on fractured femur," *J. Appl. Biomech.*, vol. 26, pp. 10-16, Feb. 2010.

33. Ellis, T., Bourgeault, C. A., and Kyle, R. F., "Screw position affects dynamic compression plate strain in an in vitro fracture model," *J. Orthop. Trauma*, vol. 15, no. 5, pp. 333-337, 2001.

34. Chen, G., Schmutz, B., Wullschleger, M., Pearcy, M. J., and Schuetz, M. A., "Computational investigations of mechanical failures of internal plate fixation," *Proc. Inst. Mech. Eng. H J Eng. Med.*, vol. 224, no. 1, pp. 119-126, 1 Jan. 2010, doi: 10.1243/09544119JEIM670.

35. Stoffel, K., Dieter, U., Stachowiak, G., Gächter, A., and Kuster, M. S., "Biomechanical testing of the LCP — how can stability in locked internal fixators be controlled?," *Injury*, vol. 34, 2, pp. B11-9, 31 Oct. 2003, doi: 10.1016/j.injury.2003.09.021.

36. Hak, D. J., Toker, S., Yi, C., and Toreson, J., "The influence of fracture fixation biomechanics on fracture healing," *Orthopedics*, vol. 33, no. 10, pp. 752-755, Oct. 2010, doi: 10.3928/01477447-20100826-20.

37. Bottlang, M., Doorink, J., Lujan, T. J., Fitzpatrick, D. C., Marsh, J. L., Augat, P., von Rechenberg, B., Lesser, M., and Madey, S. M., "Effects of contruct stiffnes on healing of fractures stabilized with locking plates," *J. Bone Joint Surg. Am.*, vol. 92, 2, pp. 12-22, 1 Dec. 2010, doi: 10.2106/JBJS.J.00780.

Chapter 5

5 Conclusions and Future Directions

5.1 Summary of Results

Instrumenting sensor packages inside orthopaedic components has long been a challenge due the unique size, signal transmission, and power management requirements of orthopaedic components [1]. While sensors have been successfully embedded in larger components such as hip, knee, and shoulder replacements, the packages are too big to fit in smaller components such as spinal fusion cages, high-tibial osteotomy implants, and some fracture fixation solutions. The conventional method of measuring implant load and deformation, using strain gauges, is the reason why these sensor packages have to be larger. Strain gauges require additional components, such as a signal processing and telemetry system. Adding components quickly increases the overall size of the package. An alternative method of measuring load and deformation must be developed to be feasible for use in smaller components. This small package would feature a signal processing and telemetry system integrated into a single package with the load sensor. In addition to load and deformation, sensorized implants can be capable of monitoring variables such as acceleration, temperature, pH, biomarkers, and more. These implants can monitor patient rehabilitation, which can help improve patient outcomes. In-vivo implant data can also help scientists and engineers improve implant design. This thesis outlined the development of a novel miniature wireless load and displacement sensor with sophisticated transmission and power management capabilities. In combination with custom deformable spring bodies, the proposed sensor can be tasked to measure a wide range of forces and is suitable for many biomechanical, commercial, and industrial applications.

First, in Chapter 2, we demonstrated that a commercially available MEMS pressure sensor can be converted into an effective tool to measure deformation and load. The device has integrated RF transmission and power management capabilities, facilitating its use as a low-power, miniature sensor package for orthopaedic applications. With the addition of an elastomeric coating to the external surface of the capacitive transducer, the sensor package is suited to measure changes in deformation over a range of 350 µm. The position of a mechanical indenter can be determined to within about 1 µm. The repeatability of the output signal profile during compressive deformation allowed the sensor package to be calibrated to measure load. The package can be tasked to measure a wide variety of load magnitudes by altering the compressive enclosure, as long as the amount of external deformation onto the sensor package does not exceed the maximum limits defined in this paper. The onboard accelerometer was calibrated and may be an effective tool to record implant motion during periods of activity. The low-power consumption of the sensor package allows it to pair with a battery or alternative power source to measure and transmit data over longer periods of time. In-vivo load and deformation information has been shown to be beneficial in the development of new orthopaedic implants and patient rehabilitation practices [1, 2] by monitoring the forces acting on the implants and surrounding structures. The novel device described in this chapter has the potential to provide wireless real-time deformation and load information, while embedded within orthopaedic implants and other deformable strain members.

In Chapter 3, we demonstrated that customizable, deformable spring bodies can be fabricated to have different load capacities, based on material selection and cantilever beam design parameters. As the width of the cantilever beams increased, the load required to cause full compression of the spring body increased. Finite element analysis was successful in predicting the increase in experimental load capacity observed in different size iterations of the spring bodies. Theoretical finite element analysis was a good indicator of fatigue life and failure location in 3D-printed PLA and Ti-6Al-4V components. As predicted, the spring bodies fabricated in titanium alloy failed before the fatigue life observed in Fe-Safe. One of the titanium alloy spring bodies was successfully paired with the FXTH87 load sensor described in Chapter 2 to produce a functional load cell capable of measuring loads up to 120 N. The calibrated load cell had error values of approximately 2% and was comparable in performance to other commercially available load sensors. The calibrated capacitive load cell passed nearly all of the performance targets proposed for implantable load sensors outlined in Section 1.5.2. This indicates that the proposed load cell is feasible for use in biomedical applications and many other remote small-scale applications. While the creep error of the sensor slightly exceeded the proposed target, drift compensation and calibration can be performed to ensure the sensor is feasible for use in static measurement applications. The load cell described in this chapter is an effective miniature wireless device that could be tasked to measure load and deformation in a handful of applications with varying load capacity. In addition to orthopaedic and biomedical applications, the proposed load cell could be used in many commercial, industrial, and research-based applications.

In Chapter 4, a simple and realistic fracture fixation finite element model was proposed to determine if the FXTH87 could be instrumented within a fixation implant to monitor the bone healing process. From the simple fixation model, adequate flexure of the fixation implant occurred that resulted in deformation of the internal cavity in the implant that houses the FXTH87. As the elastic modulus of the bone callus material was increased, the deformation of the internal cavity decreased. Therefore, the FXTH87 would be capable of monitoring the early stages of the bone healing process. The maximum stresses in the simple fixation model were slightly below the yield limit for Ti-6Al-4V. In the realistic fixation model, it was determined that deformation greater than 5 microns did not occur in the internal cavity of the implant. The FXTH87 would therefore not be able to monitor the bone healing process in the realistic loading scenario. The maximum stresses in the implant were below the yield limit of the material; however, while this is ideal in a normal scenario, it is not desired when adequate plate flexure has not occurred. The work described in Chapter 4 suggests that the FXTH87 is better suited for orthopaedic components that are purely under compression.

5.2 Future Directions

The development of a novel miniature wireless device capable of monitoring load and deformation enables numerous impactful studies that can be conducted using this device. These future studies may involve tests on the sensor and supporting spring body, but they will likely task the proposed device to measure forces in orthopaedic components and other biomedical applications.

5.2.1 Testing of FXTH87 Sensor

Performing additional tests on the modified FXTH87 sensor can further quantify the performance of the device, which can help prepare the sensor for use in future applications. In Chapter 2, it was discussed that two custom printed circuit boards were developed for the FXTH87. The first board, which was used during all testing, was a small, thin rectangular board with uni-directional communication capabilities. In other words, this device was only capable of sending signals to an external receiver. The second board, which was not used during any testing, was capable of multi-direction communication, as a small LF receiver was added to the circuit board design. Using a board with multi-directional communication could allow the FXTH87 to receive commands that could initiate/stop different sensor measurements and/or change the transmission rate of the RF transmitter. From the work discussed in Chapter 2, halting or decreasing the transmission rate when data is not required can greatly increase the life of the sensor, if a finite power source is used. Future work would also involve developing an easy-to-use user interface that would allow a user to quickly, wirelessly alter the functionality of the device. Depending on the application where the FXTH87 is tasked, the accompanying printed circuit board could be redesigned to be a different shape or possibly even smaller in size. For example, in the commercial application of the FXTH87, the circuit board is circular to save space and fit within the component designed to connect to the vehicle tire. While the FXTH87 and custom printed circuit board are effectively able to transmit through tissue to an external receiver, the maximum transmission range of the device is still very limited. If the FXTH87 was to be used in a remote application where monitoring over a large distance is required, then custom antennas could be connected to increase the transmission range. If the device was to be sealed in a metal enclosure, such as in an orthopaedic implant, transmission tests should be performed to determine how small of a break in the material is required for transmissions to be sent. There is also a scenario where the FXTH87 could have a small antenna that extrudes from the sealed metal enclosure and is encapsulated in a medical grade elastomer or surrounded by a polymer cap. This design is quite common in sensorized hip and shoulder implants with wireless transmission capabilities [3].

As for testing of the commercial and modified FXTH87, it was beyond the scope of this thesis to calibrate the built-in temperature sensor. If temperature was a desired outcome measure in an application, then a temperature sensor calibration would have to be performed. It is promising that the built-in temperature sensor has a large measuring range and is capable of monitoring temperature changes of well less than 1 °C [4]. For the modified FXTH87 described in Chapter 2, there are a number of additional tests that could be performed on the sensor package. Elastomers of different mechanical properties could be used to coat the external surface of the capacitive transducer. Other materials may have properties that are more resistant to phenomenon like stress relaxation. The devices tested in Chapter 2 were all coated in freshly cured Sylgard 184, and no preconditioning of the device was performed prior to each test. Preconditioning of the Sylgard 184 may alter both the short- and long-term mechanical properties of the material. While a short-term hysteresis test was described in Chapter 2, a long-term hysteresis test was not performed. If the modified sensor is to be implemented in an application with long-term cyclic compression, then it is important to ensure that the sensor functions as described after a high number of cycles. In Chapter 2, the built-in accelerometer was calibrated, and it was described that acceleration values could be used to trigger sensor measurements. This would help conserve the accompanying power source. Depending on the specific application, future work may involve determining a specific acceleration response that could tell the FXTH87 to initiate and/or stop sensor readings. As was described in Chapter 3, testing the modified FXTH87 in varying temperature, humidity, and pressure environments was not performed. If the FXTH87 is able to effectively operate as intended in varying environmental conditions, then the sensor is feasible for use in a larger range of applications.

5.2.2 Development and Testing of Deformable Spring Bodies

To expand on the tests performed in Chapter 3, fabricating multiple spring bodies of the same load capacity can increase the sample size of the test and allow error values to be quantified. Designing new deformable spring bodies could allow the sensor package to measure larger quantities of load while having a lengthy fatigue life. As was described in Chapter 3, it is easy to change the load capacity of the deformable bodies by altering the dimensions of the cantilever beams. Depending on the dimensions selected, the spring bodies could be capable of deforming only a couple of hundred microns under loads of multiple kilonewtons. The current iteration of the spring bodies could be redesigned to be perfectly symmetrical, which would redistribute stresses evenly over all of the cantilever beams. In addition, the spring bodies could be fabricated in different materials with varying mechanical properties to achieve different performance outcomes. If metal 3D printing is selected to fabricate the devices, then a study could be performed on how different post-processing techniques affect the fatigue life of the spring bodies. As was described in Chapter 3, depending on the application, the overall shape of the spring body could be redesigned. A future study may involve determining whether a circular or square shaped spring body with cantilever beams has the best fatigue life. The FXTH87 is versatile in the sense that it can be embedded in almost any deformable enclosure that is designed to deform only a couple of hundred microns. Deformable spring bodies that don’t use cantilever beams could be explored to determine if they are a better fit for the FXTH87.

5.2.3 Orthopaedic Applications

With the development of an effective miniature wireless load cell device and fracture fixation finite element model, additional orthopaedic applications of the package can be explored. To determine if the load cell could be feasible for use in orthopaedic applications, a model of the proposed implant, surrounding anatomy, and loading conditions must be described. This model would determine whether or not the load acting on the implants could result in deformation that the FXTH87 could measure. If adequate deformation was feasible, then it is also important to ensure that the stresses in the implant remain below the yield strength for the material so that the implant does not fail. As was described throughout the thesis, spinal fusion cages, high-tibial osteotomy implants, tibial trays, and vertebral replacements are just a few orthopaedic applications that could be capable of housing the FXTH87 package. All of these implants are subjected to compressive forces and would not require flexure to be transduced into compression. Many of these implants are small in size and existing sensor packages are currently not capable of being embedded within these implants. The size and functionalities of the FXTH87 may make it one of the only sensor packages in the world that could be instrumented within these orthopaedic applications.

5.3 Summary

Overall, this thesis outlined the development of a miniature wireless load sensor device with sophisticated RF transmission and power management capabilities. To the best of our knowledge, this one of the smallest sensors in the world capable of measuring and wirelessly transmitting load and deformation. The sensor was instrumented within proof-of-concept deformable spring bodies to demonstrate the wide range of loads the device could measure. Mechanical testing of the deformable spring bodies indicated that theoretical fatigue failure analysis can be an accurate predictor of fatigue life and failure location in experimental 3D-printed components. The finite element models of fracture fixation implants demonstrated that the FXTH87 sensor package may be better suited for orthopaedic components purely under compression. The novel FXTH87 load sensing device proposed in this thesis could be instrumented within custom deformable enclosures to transduce compression, tension, torque, and flexure. As there is no limit to the amount of load the modified FXTH87 can measure, the sensor can be adapted to a variety of applications in biomedical research.

5.4 References

1. D’Lima, D. D., Fregly, B. J., and Colwell, C. W., "Implantable sensor technology: measuring bone and joint biomechanics of daily life in vivo," *Arthritis Res. Ther.*, vol. 15, 2013, Art no. 203, doi: https://doi.org/10.1186/ar4138.

2. O’Connor, C. and Kiourti, A., "Wireless sensors for smart orthopedic implants," *J. Bio-Tribo-Corrosion,* vol. 3, p. 1127, 2017, doi: 10.1007/s40735-017-0078-z.

3. Graichen, F., Arnold, R., Rohlmann, A., and Bergmann, G., "Implantable 9-channel telemetry system for in vivo load measurements with orthopedic implants," *IEEE Trans. Biomed. Eng.*, vol. 54, pp. 253-261, 2007, doi: 10.1109/tbme.2006.886857.

4. NXP Semiconductors. *FXTH870xD, Tire Pressure Monitor Sensor*; FXTH870xD Datasheet, rev. 1.6, NXP Semiconductors: Eindhoven, The Netherlands, Feb. 2019.

Appendices

Appendix A: Copyright Permissions

MDPI Open Access Information and Policy:

Obtained from: https://www.mdpi.com/openaccess

All articles published by MDPI are made immediately available worldwide under an open access license. This means:

- everyone has free and unlimited access to the full text of *all* articles published in MDPI journals.
- everyone is free to re-use the published material if proper accreditation/citation of the original publication is given.
- open access publication is supported by the authors' institutes or research funding agencies by payment of a comparatively low **Article Processing Charge (APC)** for accepted articles.

Permissions:

Obtained from: https://www.mdpi.com/openaccess

No special permission is required to reuse all, or part of article published by MDPI, including figures and tables. For articles published under an open access Creative Common CC BY license, any part of the article may be reused without permission provided that the original article is clearly cited. Reuse of an article does not imply endorsement by the authors or MDPI.

Curriculum Vitae

Name:	William D. Anderson
Post-secondary Education and Degrees:	**Bachelor of Engineering**, University of Guelph Guelph, Ontario, Canada 2014-2018
	Master of Engineering Science, Western University London, Ontario, Canada 2018-2021
Honours and Awards:	Transdisciplinary Bone and Joint Trainee Award 2018-2021
	2nd Place poster award at 2020 Canadian Bone and Joint Conference 2020
	Dean's Honours List University of Guelph 2017, 2018
Related Work Experience	Undergraduate Research Assistant Robarts Research Institute, The University of Western Ontario 2018
	Undergraduate Research Assistant University Health Network, Toronto, Ontario 2017

Publications:

Anderson, W.D.; Wilson, S.L.M.; Holdsworth, D.W. Development of a Wireless Telemetry Sensor Device to Measure Load and Deformation in Orthopaedic Applications. *Sensors* **2020**, *20*, 6772.

Patents:

Anderson, W.D.; Wilson, S.L.M.; Holdsworth, D.W., "Wireless capacitive load cell device," U.S. Patent application 16/810,554, March 3, 2020 (patent pending).

Podium Presentations:

1.
Conference Name: Innovation in Motion Research Day
Title of Presentation: Wireless Telemetry Load Sensor for Orthopaedic Applications
Country: Canada
City: London, Ontario
Date: June 2019
Co-authors: Sydney Wilson, David W. Holdsworth

2.
Conference Name: CSME-CFDSC 2019 Congress
Title of Presentation: Wireless Telemetry Load Sensor for Orthopaedic Applications
Country: Canada
City: London, Ontario
Date: June 2019
Co-authors: Sydney Wilson, David W. Holdsworth

Poster Presentations:

1.
Conference Name: Ontario Biomechanics Conference
Title of Presentation: Wireless Telemetry Load Sensor for Orthopaedic Applications
Country: Canada
City: Alliston, Ontario
Date: March 2019
Co-authors: Sydney Wilson, David W. Holdsworth

2.
Conference Name: Imaging Network Ontario Conference
Title of Presentation: Wireless Telemetry Load Sensor for Orthopaedic Applications
Country: Canada
City: London, Ontario
Date: March 2019
Co-authors: Sydney Wilson, David W. Holdsworth

3.
Conference Name: London Health Research Day
Title of Presentation: Wireless Telemetry Load Sensor for Orthopaedic Applications
Country: Canada
City: London, Ontario
Date: April 2019
Co-authors: Sydney Wilson, David W. Holdsworth

4.
Conference Name: Imaging Network Ontario 2020 Symposium

Title of Presentation: Design and 3D Printing of Wireless Load Cells for Biomedical Applications
Country: Canada
City: London, Ontario (Virtual)
Date: March 26/27, 2020
Co-authors: Sydney Wilson, David W. Holdsworth

5.
Conference Name: Canadian Bone and Joint Conference
2nd Place Poster Award in MSK Rehab & Biomechanics
Title of Presentation: Design and 3D Printing of Wireless Load Cells for Biomedical Applications
Country: Canada
City: London, Ontario (Virtual)
Date: June 11-13, 2020
Co-authors: Sydney Wilson, David W. Holdsworth

6.
Conference Name: Robarts Research Retreat
Type of Presentation: 3-Minute Thesis
Title of Presentation: Design and 3D Printing of Wireless Load Cells for Biomedical Applications
Country: Canada
City: London, Ontario (Virtual)
Date: June 19th, 2020
Co-authors: Sydney Wilson, David W. Holdsworth

7.
Conference Name: Imaging Network Ontario 2021 Symposium
Title of Presentation: Fatigue Analysis of Wireless Load Cells for Biomedical Applications
Country: Canada
City: London, Ontario (Virtual)
Date: March 23/24, 2021
Co-authors: Todor Ivanov, David W. Holdsworth

8.
Conference Name: London Health Research Day
Title of Presentation: Fatigue Analysis of Wireless Load Cells for Biomedical Applications
Country: Canada
City: London, Ontario (Virtual)
Date: May 11th, 2021
Co-authors: Todor Ivanov, David W. Holdsworth

9.

Conference Name: Robarts Research Retreat
Title of Presentation: Fatigue Analysis of Wireless Load Cells for Biomedical Applications
Country: Canada
City: London, Ontario (Virtual)
Date: June 17th, 2021
Co-authors: Todor Ivanov, David W. Holdsworth